8-16-2024

Exiting Inflation with a Smooth Scale Factor

Harry Oslislo
University of South Carolina

Exiting Inflation with a Smooth Scale Factor

by

Harry Frank Oslislo

Bachelor of Science
Rutgers University 1973

Submitted in Partial Fulfillment of the Requirements

for the Degree of Doctor of Philosophy in

Physics

College of Arts and Sciences

University of South Carolina

2024

Accepted by:

Brett Altschul, Major Professor

Matthias Schindler, Committee Member

Yaroslaw Bazaliy, Committee Member

Quentin Bailey, Committee Member

Ann Vail, Dean of the Graduate School

Acknowledgments

I want to thank the members of my doctoral committee, who educated me and enabled me to reach this goal. Over the years that I have attended the University, I found myself seeking them out for guidance and advice, and I am grateful for their help and encouragement.

Without the support of my advisor, Dr. Altschul, none of this would have been possible. He provided me patient, positive direction every week consistently for several years. His knowledge and experience are simply astonishing. All of my work flowed from him, and I consider myself fortunate that Dr. Altschul has been my advisor.

Abstract

The expectation that the physical expansion of space occurs smoothly may be expressed mathematically as a requirement for continuity in the time derivative of the metric scale factor of the Friedmann–Robertson–Walker cosmology. We explore the consequences of imposing such a smoothness requirement, examining the forms of possible interpolating functions between the end of inflation and subsequent radiation- or matter-dominated eras, using a straightforward geometric model of the interpolating behavior. We quantify the magnitude of the cusp found in a direct transition from the end of slow roll inflation to the subsequent era, analyze the validity several smooth interpolator candidates, and investigate equation-of-state and thermodynamic constraints. We find an order-of-magnitude increase in the size of the universe at the end of the transition to a single-component radiation or matter era. We also evaluate the interpolating functions in terms of the standard theory of preheating and determine the effect on the number of bosons produced.

Table of Contents

List of Tables

List of Figures

Chapter 1

Introduction

1.1 The Geometry of Spacetime

The cosmological principal states that the universe is homogeneous and isotropic on large scales. Ancient astronomers placed Earth at the center of the universe. It remained there centuries later under the influence of epicycles, which were increasingly intricate adjustments to the models underlying the predicted motion of cosmological objects, until Copernicus relocated the center of the universe to the sun. Although agreement on the location of the center remained unsettled, the focus of astronomers moved provisionally to the center of mass within the volume under consideration in Newtonian gravitation, with the space outside the volume assumed to be homogeneous and isotropic. Finally convinced by empirical evidence available beginning in the twentieth century, modern cosmologists have come to rely on the cosmological principle. On sufficiently large scales such that existing structure becomes immaterial, observers see a universe that is the same everywhere and lacks a preferred direction. If not, for instance, observers might find themselves living in an isotropic but not homogeneous universe, like one with a preferred position at which an observer witnesses the density of structure dependent on radial distance. Conversely, the universe might be homogeneous without being isotropic. For example, space filled with a pervasive vector field establishes a preferred direction dependent on the line of sight of an observer.

Based on the foundation of the theory of General Relativity and the cosmological principal, Alexander Friedmann and his contemporaries provided cosmologists with tools to

study the dynamics of the universe. The cosmological principal is the basis for Friedmann–Robertson–Walker (FRW) models of cosmology [1–3]. In our notation, $\hbar = 1$ and $c = 1$ hereafter unless otherwise noted. Below we have the Minkowski metric, which satisfies Einstein's first postulate of Special Relativity that spacetime measurements are Lorentz invariant with respect to inertial frames of reference,

$$ds^2 = dt^2 - (dx^2 + dy^2 + dz^2) = dt^2 - dl^2. \tag{1.1}$$

Homogeneity imposes the restriction of a constant coefficient before dt^2, here equal to one after rescaling the other elements, and isotropy removes off-diagonal elements [4].

Geodesic slices at fixed times foliate spacetime into 3 dimensional manifolds. These geodesics define the shortest metrics in spacetime, and the manifolds possess an inherent flat, spherical, or hyperbolic geometrical radius of curvature $= 0, > 0,$ or < 0, respectively. The radius of curvature is constant throughout space in a homogeneous, isotropic universe [5]. In 2 dimensional Euclidean space, for a circle we have line element and radius R [6, 7]:

$$dl^2 = dx^2 + dy^2 \text{ and } R^2 = x^2 + y^2. \tag{1.2}$$

The analogous representations in $(1 + 1)$-dimensional Minkowski spacetime for a hyperbola of constant separation of the vertices S are

$$dl^2 = dx^2 - dt^2 \text{ and } S^2 = -x^2 + t^2. \tag{1.3}$$

Combining the formalism for the circle and the hyperbola results in

$$dl^2 = dx^2 \pm du^2 \tag{1.4}$$

$$\pm C^2 = x^2 \pm u^2. \tag{1.5}$$

The parameter C, the radius of curvature in our geometry, represents both the constant radius R and the constant separation S of the hyperbola. The parameter u stands for the

second dimension in our geometries, y for the circle and time t for the parabola in (1 + 1)-dimensional space. Differentiating eq. (1.5) gives

$$du^2 = \frac{x^2\,dx^2}{u^2} = \frac{x^2\,dx^2}{C^2 \mp x^2}. \tag{1.6}$$

After substituting this into the eq. (1.4) line element, we obtain

$$dl^2 = dx^2\left(1 \pm \frac{x^2}{C^2 \mp x^2}\right). \tag{1.7}$$

We extend this treatment to more rigorous mathematical theory. The geometry encompasses that of a three-sphere embedded in four-dimensional Euclidean space and a hyperboloid embedded in (1 + 3)-dimensional space. In 3 dimensional spherical coordinates,

$$d\mathbf{x}^2 = dr^2 + r^2(d\theta^2 + \sin^2\theta\,d\phi^2) \tag{1.8}$$

$$\mathbf{x}^2 = r^2 \tag{1.9}$$

$$\mathbf{x}\,d\mathbf{x} = \frac{1}{2}d|\mathbf{x}|^2 = r\,dr. \tag{1.10}$$

Below we first make these substitutions into the eq. (1.7) line element,

$$dl^2 = dr^2 \pm \frac{r^2\,dr^2}{C^2 \mp r^2} + r^2(d\theta^2 + \sin^2\theta\,d\phi^2) \tag{1.11}$$

$$= dr^2\left(\frac{1}{1 \mp \frac{r^2}{C^2}}\right) + r^2(d\theta^2 + \sin^2\theta\,d\phi^2), \tag{1.12}$$

and then use this result to replace the line element in the eq. (1.1) metric,

$$ds^2 = dt^2 - dr^2\left(\frac{1}{1 \mp \frac{r^2}{C^2}}\right) + r^2(d\theta^2 + \sin^2\theta\,d\phi^2). \tag{1.13}$$

We introduce the parameter κ, which is the inverse of the radius of curvature squared, $\kappa = 1/C^2$, with units of inverse length squared and get

$$ds^2 = dt^2 - dr^2\left(\frac{1}{1 \mp \kappa r^2}\right) + r^2(d\theta^2 + \sin^2\theta\,d\phi^2). \tag{1.14}$$

The angular parameters θ, $d\theta$, and $d\phi$ are invariant to spatial expansion in 3 dimensions. The other parameters are functions of time subject to the effect of expansion. We convert

the observable *proper distance* r measured in local coordinates at a specific time into a *comoving distance* r' with coordinates that remain constant in time:

$$r = a(t)r', \tag{1.15}$$

and convert the other distance parameters, $dr = a(t)dr'$ and $\kappa = \kappa'/a^2(t)$, similarly. All distances relative to an observer in a comoving frame of reference expand by $a(t)$, so that such an observer continues to see an istropic universe as time passes. By contrast, for example, on Earth we see the redshifting and blueshifting of the Cosmic Microwave Background (CMB) depending on the line of sight as our frame of reference travels through space relative to the CMB isotropy. After dropping the prime for convenience, we are left with the metric

$$ds^2 = dt^2 - a^2(t)\left[\left(\frac{1}{1 \mp \kappa r^2}\right)dr^2 + r^2(d\theta^2 + \sin^2\theta\, d\phi^2)\right]. \tag{1.16}$$

The observable spacetime metric ds^2 in eq. (1.16) comprises the observable proper time element dt^2 and the observable proper distance element, consisting of the time dependent conversion factor $a(t)$, called the *scale factor*, and the comoving distance. The comoving distance represents the shortest distance between events on the spacetime geodesic. Both parameters in factor κr^2 are comoving. At the present, the proper and comoving distances are equal, so that $a(t) = 1$. The product of a distance measurement today and the scale factor at time t provides the calculated distance measure at t. Figure 1.1 depicts the expansion in space of a comoving displacement defined by constant coordinates.

Next we rescale the line element components to transform κ into *curvature constant* k, such that $k = 0, +1, -1$ for the flat, spherical, and hyperbolic curvatures described above. The rescaling relations are [8]

$$k = \frac{\kappa}{|\kappa|} \tag{1.17}$$

$$r' = |\kappa|^{1/2} r \tag{1.18}$$

$$dr' = |\kappa|^{1/2} dr \tag{1.19}$$

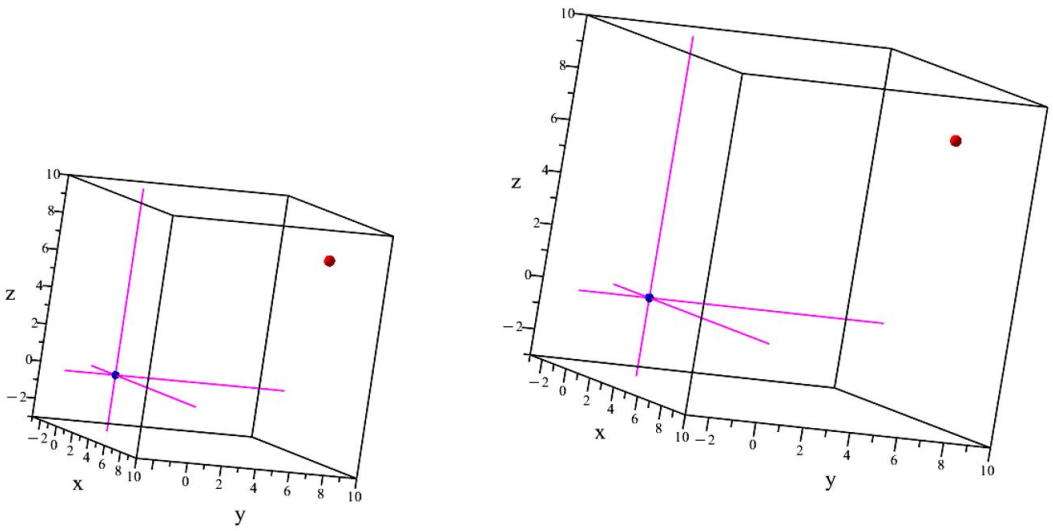

Figure 1.1 As space expands in time, comoving coordinates remain constant.

$$a' = \frac{a}{|k|^{1/2}}. \tag{1.20}$$

Again we drop the prime for convenience to get the Robertson–Walker (RW) metric, the basis for the FRW models of cosmology:

$$ds^2 = dt^2 - a^2(t)\left[\left(\frac{1}{1-kr^2}\right)dr^2 + r^2(d\theta^2 + \sin^2\theta\, d\phi^2)\right]. \tag{1.21}$$

The scale factor $a(t)$ quantifies the expansion of space in time. We derive it from the Einstein field equations in section 1.2, in which we also show the RW metric informs the derivation of the stress-energy tensor and the Ricci tensor and scalar. Further, we see the role of the RW metric in the models of inflation in chapter 2, both as the background for old inflation and the equations of motion for new inflation and chaotic inflation.

1.2 The Friedmann Equations

Alexander Friedmann based a second tool he contributed to cosmology, the *Friedmann equations*, on the Einstein field equations. He assumed the universe consists of a plasma that acts as a perfect fluid, that is, a smoothly flowing, incompressible fluid without viscosity. Inflation theorists base their work on the same assumption.

The RW metric written as tensors is

$$ds^2 = g_{\mu\nu} dx^\mu dx^\nu \tag{1.22}$$

with metric tensor

$$g_{\mu\nu} = \begin{pmatrix} 1 & 0 & 0 & 0 \\ 0 & -\frac{a^2}{1-kr^2} & 0 & 0 \\ 0 & 0 & -a^2 r^2 & 0 \\ 0 & 0 & 0 & -a^2 r^2 \sin^2(\theta) \end{pmatrix}. \tag{1.23}$$

We proceed by first evaluating the left-hand side of the Einstein field equations, after combining the cosmological constant with the stress-energy tensor on the right:

$$R_{\mu\nu} - \frac{1}{2} g_{\mu\nu} R = 8\pi G \, T_{\mu\nu}. \tag{1.24}$$

The Ricci tensor $R_{\mu\nu}$ results from the contraction of the Riemann tensor:

$$R_{\mu\nu} = R^\alpha_{\mu\alpha\nu} = \frac{\partial}{\partial_\alpha} \Gamma^\alpha_{\mu\nu} - \frac{\partial}{\partial_\nu} \Gamma^\alpha_{\mu\alpha} + \Gamma^\alpha_{\sigma\alpha} \Gamma^\sigma_{\mu\nu} - \Gamma^\alpha_{\sigma\nu} \Gamma^\sigma_{\mu\alpha}. \tag{1.25}$$

The equation for the Christoffel symbol,

$$\Gamma^l_{ji} = \frac{1}{2} g^{lm} \left(\frac{\partial g_{mi}}{\partial x^j} + \frac{\partial g_{mj}}{\partial x^i} - \frac{\partial g_{ij}}{\partial x^m} \right), \tag{1.26}$$

displays symmetry $\Gamma^l_{ji} = \Gamma^l_{ij}$, and the diagonal metric tensor implies that only terms with $l = m$ survive, from which we obtain a set of non-zero symbols. For example, for $l = m = 0$:

$$\Gamma^t_{ji} = \frac{1}{2} g^{tt} \left(\frac{\partial g_{ti}}{\partial x^j} + \frac{\partial g_{tj}}{\partial x^i} - \frac{\partial g_{ij}}{\partial x^t} \right) \tag{1.27}$$

$$\Gamma^t_{rr} = \frac{1}{2} g^{tt} \left(\frac{\partial g_{tr}}{\partial x^r} + \frac{\partial g_{tr}}{\partial x^r} - \frac{\partial g_{rr}}{\partial x^t} \right) = \frac{a\dot{a}}{1 - kr^2} \tag{1.28}$$

$$\Gamma^t_{\theta\theta} = a\dot{a} r^2; \; \Gamma^t_{\phi\phi} = a\dot{a} r^2 \sin^2(\theta). \tag{1.29}$$

Appendix A contains the rest of the non-zero symbols.

For a perfect fluid, the energy density is constant, the lack of viscosity eliminates sheer forces, and rotation and turbulence are absent in the smooth flow. The right-hand side of the

Einstein field equations, the stress-energy tensor, is diagonal for a pre-inflationary plasma of energy and matter that acts as a perfect fluid [9]:

$$T_{\mu\nu} = (\rho + p)U_\mu U_\nu - p g_{\mu\nu}. \tag{1.30}$$

In the fluid rest frame, that is, the frame of an observer moving with the flow of the fluid, the four-velocity $U_\alpha = (c, \mathbf{0})$. The stress-energy tensor takes the form

$$T_{\mu\nu} = \begin{pmatrix} \rho & 0 & 0 & 0 \\ 0 & -pg_{11} & 0 & 0 \\ 0 & 0 & -pg_{22} & 0 \\ 0 & 0 & 0 & -pg_{33} \end{pmatrix}. \tag{1.31}$$

Thus the Ricci tensor has the same diagonal form. For example,

$$R_{tt} = R^\alpha_{t\alpha t} = \frac{\partial}{\partial_\alpha}\Gamma^\alpha_{tt} - \frac{\partial}{\partial_t}\Gamma^\alpha_{t\alpha} + \Gamma^\alpha_{\sigma\alpha}\Gamma^\sigma_{tt} - \Gamma^\alpha_{\sigma t}\Gamma^\sigma_{t\alpha} \tag{1.32}$$

$$= -\frac{\partial}{\partial_t}\Gamma^\alpha_{t\alpha} - \Gamma^\alpha_{\sigma t}\Gamma^\sigma_{t\alpha} \tag{1.33}$$

$$= -\frac{3\ddot{a}}{a}. \tag{1.34}$$

Similarly,

$$R_{rr} = \frac{1}{1-kr^2}\left(a\ddot{a} + 2\dot{a}^2 + 2k\right);\ R_{\theta\theta} = r^2\left(a\ddot{a} + 2\dot{a}^2 + 2k\right);\ R_{\phi\phi} = r^2\sin^2(\theta)\left(a\ddot{a} + 2\dot{a}^2 + 2k\right). \tag{1.35}$$

Contracting the Ricci tensor yields the Ricci scalar

$$R = g^{\mu\nu}R_{\mu\nu} \tag{1.36}$$

$$= -6\left[\frac{\ddot{a}}{a} + \left(\frac{\dot{a}}{a}\right)^2 + \frac{k}{a^2}\right]. \tag{1.37}$$

Combining the left-hand and right-hand sides of the Einstein field equations, that is, eqs. (1.34), (1.35), and (1.37) on the left and eq. (1.31) on the right, we get an expression for the time components and a second one for the space components:

$$\left[\frac{\dot{a}(t)}{a(t)}\right]^2 + \frac{k}{a^2(t)} = \frac{8\pi G}{3}\rho(t) \tag{1.38}$$

$$\frac{2\ddot{a}(t)}{a(t)} + \left[\frac{\dot{a}(t)}{a(t)}\right]^2 + \frac{k}{a^2(t)} = -8\pi G p(t). \tag{1.39}$$

Each individual spatial component exhibits the same dependency of expansion on pressure in eq. (1.39). Conversion of eq. (1.39) by substituting the first Friedmann equation, eq. (1.38), into it yields the second Friedmann equation, also called the *acceleration equation*:

$$\frac{\ddot{a}}{a} = -\frac{4\pi G}{3}(\rho + 3p). \tag{1.40}$$

In the same way that the stress-energy tensor of the Einstein field equations informs the dynamics of the mass and energy that comprise it, the energy density and pressure of the Friedman equations direct the expansion of space represented by the scale factor and its rate of change and acceleration. Taken together, the Friedman equations show that although the rate of expansion increases proportionally to an increase in energy density, the acceleration of the expansion decreases with an increase in either the energy density or pressure. The first Friedmann equation, eq. (1.38), determines the expansion rate of the universe, the Hubble parameter, $H(t) = \frac{\dot{a}}{a}$. The sign inherent in $\dot{a} > 0$ or $\dot{a} < 0$ dictates whether the universe expands or contracts. Theorists use the acceleration, specifically, $\ddot{a} > 0$, to define a spacetime state of inflation.

The energy density ρ consists of all types of particles. We use the first Friedmann equation to derive the scale factor dependency on time for single component matter-filled and radiation-filled universes in section 1.3. We also rewrite the first Friedman equation in terms of the critical density associated with a flat universe to derive an observable measure of flatness in section 1.4. Section 1.5 describes cosmological issues that motivated the formulation of inflationary theory.

1.3 The Fluid Equation

A third tool available to cosmologists in their study of the dynamics of space is the *fluid equation*, which we derive here with the principles of thermodynamics. Energy expressed

as a comoving density is

$$U = \rho V, \tag{1.41}$$

with volume $V = \frac{4}{3}\pi a^3(t) r^3$ and constant comoving r. Differentiating the energy in time results in

$$\dot{U} = 4\pi a^2(t)\dot{a}(t)\rho(t) + \frac{4}{3}\pi a^3(t)\dot{\rho}(t). \tag{1.42}$$

The vacuum of space in a homogeneous, isotropic universe experiences no heat flow or pressure gradient effect. The first law of thermodynamics $dU = dQ - PdV$ therein reduces to $dU = -PdV$. Differentiation with respect to time,

$$4\pi a^2(t)\dot{a}(t)p = -\frac{4}{3}\pi a^3(t)\dot{\rho}(t) - 4\pi a^2(t)\dot{a}(t)\rho(t), \tag{1.43}$$

yields a version of the fluid equation in terms of both energy density and pressure,

$$\dot{\rho}(t) = -3\frac{\dot{a}(t)}{a(t)}\left[\rho(t) + p\right]. \tag{1.44}$$

For $\dot{a}(t) > 0$, for example, energy decreases as space expands due to the dilution of particles and the work done by pressure.

The dynamic behavior of the energy density applies to the variety of particles found in the universe. For simplicity, we consider single component, non-relativistic and relativistic particles separately. On large scales, matter in a homogeneous isotropic universe exhibits dust-like characteristics, that is, matter acts as if it were a pressureless perfect fluid. For relativistic particles, the thermodynamic energy and entropy are $U = \sigma V T^4$ and $S = \frac{4}{3}\frac{U}{T} = \frac{4}{3}VT^3$, respectively. The Stefan-Boltzmann constant σ is the proportionality coefficient. The Helmholtz free energy $F = U - TS$ becomes

$$F = \sigma V T^4 - \frac{4}{3}\sigma V T^4 = -\frac{1}{3}\sigma V T^4. \tag{1.45}$$

Pressure of the relativistic particles in terms of the Helmholtz free energy is

$$P = -\left(\frac{\partial F}{\partial V}\right)_T = \frac{1}{3}\sigma T^4 = \frac{1}{3}\frac{U}{V} = \frac{1}{3}\rho. \tag{1.46}$$

The results for the two forms of particles give us a linear relationship between pressure and energy density, the *equation of state*,

$$p = w\rho, \tag{1.47}$$

with $w = 0$ for non-relativistic particles and $w = 1/3$ for relativistic particles. Substitution into eq. (1.44) yields the well known form of the fluid equation,

$$\dot{\rho}(t) = -3\frac{\dot{a}(t)}{a(t)}\rho(t)(1 + w). \tag{1.48}$$

The first Friedmann equation combined with the fluid equation enables us to determine the way in which space expands in time for a single component universe. After integrating eq. (1.48) from t_0 to t, we find [10]

$$\rho(t) = \rho(t_0)\left[\frac{a(t)}{a(t_0)}\right]^{-3(1+w)}. \tag{1.49}$$

For a universe consisting of only non-relativistic matter,

$$\rho(t) = \rho(t_0)\left[\frac{a(t)}{a(t_0)}\right]^{-3}. \tag{1.50}$$

Substituting this result into the first Friedmann equation with $\left[\frac{\dot{a}(t)}{a(t)}\right]^2 \gg \frac{k}{a(t)^2}$ gives

$$\left[\frac{\dot{a}(t)}{a(t)}\right]^2 = \frac{8\pi G}{3}\rho(t_0)\left[\frac{a(t)}{a(t_0)}\right]^{-3}. \tag{1.51}$$

In differential form, we have

$$a^{1/2}(t)\,da = \left[\frac{8\pi G}{3}\rho(t_0)a^3(t_0)\right]^{1/2} dt. \tag{1.52}$$

Integration reveals the relation of expansion of space of a matter-filled universe to time to be

$$a(t) \propto t^{2/3}, \tag{1.53}$$

after neglecting the contributions of $a(t_0)$ and t_0, if any. Similarly, for a radiation-filled universe with $w = 1/3$,

$$\rho(t) = \rho(t_0)\left[\frac{a(t)}{a(t_0)}\right]^{-4}. \tag{1.54}$$

The associated Friedmann equation,

$$\left[\frac{\dot{a}(t)}{a(t)}\right]^2 = \frac{8\pi G}{3}\rho(t_0)\left[\frac{a(t)}{a(t_0)}\right]^{-4}, \tag{1.55}$$

leads to

$$a(t)\,da = \left[\frac{8\pi G}{3}\rho(t_0)\right]^{1/2} a^2(t_0)\,dt \tag{1.56}$$

and the proportionality

$$a(t) \propto t^{1/2}. \tag{1.57}$$

Analysis of the fluid equation provides the understanding that energy density scales with the expansion of space by factors proportional to $a^{-3}(t)$ and $a^{-4}(t)$ for matter-filled and radiation-filled single component universes, respectively, while $a(t)$ itself scales $\propto t^{2/3}$ and $t^{1/2}$, respectively. Dilution of both types of particles by the volume expansion of space decreases the energy density by a^{-3}. Expansion also reduces the energy density of radiation by another factor of a^{-1} due to the redshift of the comoving electromagnetic wavelengths λ_{cm} as they lengthen during expansion in the same way as any other spatial displacement, $\lambda(t) = a(t)\lambda_{cm}$. These insights drive derivation of a measure of the flatness of curved spacetime in section 1.4.

1.4 Spatial Curvature

We have characterized the spherical, flat, and hyperbolic geometries of the universe in the eq. (1.21) RW metric with curvature constant values +1, 0, and -1, respectively, which cosmologists describe as *closed*, *flat*, and *open*. In a flat universe, the first Friedmann equation

$$\left[\frac{\dot{a}(t)}{a(t)}\right]^2 = \frac{8\pi G}{3}\rho(t) - \frac{k}{a^2(t)}, \tag{1.58}$$

reduces to

$$\left[\frac{\dot{a}(t)}{a(t)}\right]^2 = \frac{8\pi G}{3}\rho(t). \tag{1.59}$$

For a given energy density, as $t \to \infty$ and the energy density undergoes dilution and tends to zero, a flat universe expands with a positive decreasing rate of expansion $\frac{\dot{a}(t)}{a(t)} \to 0$. An open universe with

$$\left[\frac{\dot{a}(t)}{a(t)}\right]^2 = \frac{8\pi G}{3}\rho(t) + \frac{1}{a^2(t)} \tag{1.60}$$

expands forever at a positive decreasing rate that never goes to zero. For a closed universe, the Friedman equation

$$\left[\frac{\dot{a}(t)}{a(t)}\right]^2 = \frac{8\pi G}{3}\rho(t) - \frac{1}{a^2(t)} \tag{1.61}$$

predicts expansion at a decreasing rate until

$$a(t) = \left[\frac{3}{8\pi G\rho(t)}\right]^{1/2}, \tag{1.62}$$

at which time expansion stops and space begins to contract.

We measure flatness using an empirical attribute of curvature called the *density parameter*, Ω_t, derived below starting with the first Friedmann equation,

$$H^2(t) = \frac{8\pi G}{3}\rho_t - \frac{k}{a^2(t)}. \tag{1.63}$$

We define a critical density $\rho_{cr,t}$ expressed in terms of the Hubble parameter as the density at time t at which the geometry of the universe is flat, namely,

$$\rho_{cr,t} = \frac{3}{8\pi G}H^2(t), \tag{1.64}$$

where

$$\rho_t = \sum_i \rho_{i,t} = \rho_{m,t} + \rho_{r,t} + \rho_{\Lambda,t}. \tag{1.65}$$

Each component above, that is, matter, radiation, and the vacuum, has an associated density parameter, a ratio in terms of the critical density:

$$\Omega_{i,t} = \frac{\rho_{i,t}}{\rho_{cr,t}}. \tag{1.66}$$

The sum of these,

$$\Omega_t = \sum_i \Omega_{i,t}, \tag{1.67}$$

gives us a measure of the flatness of the universe, the *spatial curvature parameter*, $\Omega_k = (1 - \Omega_t)$, which is the variation of the density parameter from 1:

$$\Omega_k = (1 - \Omega_t) = (1 - \Omega_{m,t} - \Omega_{r,t} - \Omega_{\Lambda,t}). \tag{1.68}$$

For a flat universe at the critical density, $(1 - \Omega_t) = 0$. When the density of the universe is greater than the critical density, we have $(1 - \Omega_t) < 0$, and the amount of matter, radiation, and vacuum energy will cause gravitational collapse. An open universe, with $(1 - \Omega_t) > 0$, expands forever at a decreasing rate.

Using these definitions and attributes we convert the first Friedmann equation into a measurable form:

$$H^2(t) = \frac{8\pi G}{3}(\rho_{m,t} + \rho_{r,t} + \rho_{\Lambda,t}) - \frac{k}{a^2(t)}. \tag{1.69}$$

$$H^2(t) = H^2(t)\left[\Omega_{m,t} + \Omega_{r,t} + \Omega_{\Lambda,t} - \frac{k}{a^2(t)H^2(t)}\right]. \tag{1.70}$$

$$(1 - \Omega_t) = -\frac{k}{a^2(t)H^2(t)}. \tag{1.71}$$

$$(1 - \Omega_0) = -\frac{k}{a^2(t_0)H_0^2}. \tag{1.72}$$

The last equation is the measure of flatness in the present, designated by subscript 0. Equation (1.71) also provides the insight that the variation cannot change sign, because k does not change its value, as evidenced by the first Friedman equation. An open or closed universe remains open or closed. Expansion does not change the topology of the universe.

We extract a relation for the evolution of flatness by eliminating the curvature constant k from equations (1.71) and (1.72) with the scale factor today $a(t_0) = 1$:

$$(1 - \Omega_t) = \frac{H_0^2}{a^2(t)H^2(t)}(1 - \Omega_0). \tag{1.73}$$

We thus obtain a form of the Friedmann equation that is responsive to observation, one that provides a function of the variation from 1 of the density parameter in the past based on the observational variation in the present. Using equation (1.73) to quantify flatness requires an expression for $\frac{H_0^2}{H^2(t)}$.

Comoving densities, as derived in Appendix B,

$$\rho_{m,t} = \frac{\rho_{m,0}}{a^3(t)} \; ; \; \rho_{r,t} = \frac{\rho_{r,0}}{a^4(t)} \; ; \; \rho_{\Lambda,t} = \rho_{\Lambda,0}, \tag{1.74}$$

transform equation(1.69) into

$$H^2(t) = \frac{8\pi G}{3}\left[\frac{\rho_{m,0}}{a^3(t)} + \frac{\rho_{r,0}}{a^4(t)} + \rho_{\Lambda,0}\right] - \frac{k}{a^2(t)}. \tag{1.75}$$

Substitution of the component density parameters of equation(1.66) leaves

$$H^2(t) = \frac{8\pi G}{3}\left[\frac{\Omega_{m,0}\rho_{cr,0}}{a^3(t)} + \frac{\Omega_{r,0}\rho_{cr,0}}{a^4(t)} + \Omega_{\Lambda,0}\rho_{cr,0}\right] - \frac{k}{a^2(t)} \tag{1.76}$$

$$= H_0^2\left[\frac{\Omega_{m,0}}{a^3(t)} + \frac{\Omega_{r,0}}{a^4(t)} + \Omega_{\Lambda,0} - \frac{k}{a^2(t)H_0^2}\right]. \tag{1.77}$$

We simplify equation(1.70) as

$$1 = \left[\Omega_{m,t} + \Omega_{r,t} + \Omega_{\Lambda,t} - \frac{k}{a^2(t)H^2(t)}\right], \tag{1.78}$$

enabling us to interpret the term $\frac{k}{a^2(t)H^2(t)}$ as the density parameter remaining after taking the difference between 1 and the matter, radiation, and vacuum density parameters. The term $\frac{k}{a^2(t)H^2(t)}$ drives the rate of expansion with a sign opposite to that of k. Thus, we observe that $+(1-\Omega_t)$ is the contribution to the rate of expansion of space due to curvature. Eq. (1.78) today is

$$1 = \left[\Omega_{m,0} + \Omega_{r,0} + \Omega_{\Lambda,0} - \frac{k}{a^2(t_0)H_0^2}\right] \tag{1.79}$$

$$1 - \Omega_0 = -\frac{k}{a^2(t_0)H_0^2} = -\frac{k}{H_0^2}. \tag{1.80}$$

Applying this result to equation(1.77) yields the required coefficient,

$$\frac{H_0^2}{H^2(t)} = \left[\frac{\Omega_{m,0}}{a^3(t)} + \frac{\Omega_{r,0}}{a^4(t)} + \Omega_{\Lambda,0} + \frac{(1-\Omega_0)}{a^2(t)}\right]^{-1}. \tag{1.81}$$

Equation(1.73), the evolution of the variation from 1 of the density parameter, becomes

$$(1-\Omega_t) = \frac{a^2(t)(1-\Omega_0)}{a(t)\Omega_{m,0} + \Omega_{r,0} + a^4(t)\Omega_{\Lambda,0} + a^2(t)(1-\Omega_0)}, \tag{1.82}$$

which is a form responsive to observation.

1.5 The Flatness, Horizon, and Monopole Problems

The problem of trying to reconcile physical theories regarding the form and evolution of the primordial universe with modern cosmological observations has occupied researchers for decades. Providing a complete explanation for the origins of the characteristics that the universe exhibits today has been challenging. We witness extreme uniformity and flatness and the absence of certain particles predicted in some Grand Unified Theory (GUT) models. Many physicists have detailed these well-known difficulties in texts and expository papers; see, for example, Refs. [11–19].

1.5.1 The Flatness Problem

Expansion itself does not change the inherent topology of the universe: A universe that is closed, open, or flat remains so. However, expansion makes any curvature appear locally more flat. In the preceding section lies the basis of the Flatness Problem. The most recent experimental data from the Planck Collaboration sets the spatial curvature parameter today, $\Omega_k = 1 - \Omega_0$, at $\approx 7 \times 10^{-4}$ [20]. However, because k does not change its value, if we observe an open universe today, going back in time we expect to see an open universe. The geometry of a closed universe would remain unchanged similarly going back in time.

Although the expansion of space would tend to flatten the radius of curvature, and intuitively we recognize that expansion flattens a sphere and a hyperbola, we see from eq. (1.71) an inverse dependence on the rate of change of the scale factor,

$$|\Omega_k| = |(1 - \Omega_t)| = \left| -\frac{k}{a^2(t)H^2(t)} \right| \tag{1.83}$$

$$= \left| -\frac{k}{\dot{a}^2(t)} \right|. \tag{1.84}$$

But the scale factor differentials for the matter-dominated and radiation-dominated eras, $\dot{a}(t) \propto t^{-1/3}$ and $\dot{a}(t) \propto t^{-1/2}$, respectively, are themselves inversely dependent on time, so that $|\Omega_k|$ decreases going backward in time through the eras.

To evaluate the evolution of the variation, we use generally accepted values for the scale factor at various periods in the history of the universe and recent experimental data for densities [11, 20]. The trend of $|(1 - \Omega_t)|$ ranges from the Planck Collaboration $\approx 7 \times 10^{-4}$ today to $\lesssim 10^{-6}$ at recombination, $\lesssim 10^{-7}$ at matter-radiation equality, and $\lesssim 10^{-14}$ at Big Bang nucleosynthesis, according to eq. (1.82). Continuing backward in time would generate increasingly extreme variations from 1. Table 1.1 details these values. The density factors m, γ, and Λ, for matter, radiation, and the vacuum energy, respectively, reflect approximations of the composition of the universe during the applicable periods. Big Bang nucleosynthesis is the theoretical era of fusion of fundamental observable matter giving rise to heavier elements. Following the arbitrary milestone of the equality of matter and radiation densities, recombination of protons and electrons to form hydrogen atoms was the event that precipitated the creation of the CMB, when the universe was sufficiently large so that photons were first able to stream without scattering.

Table 1.1 The variation in curvature at selected periods going backward in time in the history of the universe.

		Density Factor				
Period	~ Age	m	γ	Λ	$\approx$ a(t)	$(1 - \Omega_t)$
Today	3.8×10^9 years	0.31	0	0.69	1.0	0.0007
Recombination	380,000 years	1.0	0	0	9.1×10^{-4}	2.0×10^{-6}
Matter-radiation equality	47,000 years	0.5	0.5	0	2.8×10^{-4}	3.2×10^{-7}
Big Bang nucleosynthesis	2 minutes	0	1.0	0	3.6×10^{-8}	1.1×10^{-14}

Inflation offers a remedy: The inflationary exponential scale factor would tend to drive down the spatial curvature to a level that could support subsequent evolution to the value observed today, as discussed in section 2.2.2. Otherwise, in the absence of this solution, physics has to devise an alternative model of origin to account for an apparently flat universe initially.

1.5.2 The Horizon Problem

The issue of uniformity has the name the *Horizon Problem*. We see a homogeneous, isotropic universe on large scales. Despite the almost incomprehensible longevity of the universe, it is simply too immense to have grown to be uniform on large scales. Causality demands that local homogeneity takes time to develop, with equilibrium conditions dispersing at a rate no greater than the speed of light. Two local homogeneous elements dispersed in time must retain a causal connection to remain in equilibrium with one another. Yet opposite sides of the universe appear nearly identical to us. Even if we assume they started that way, not enough time has passed for space to have expanded a great enough distance to maintain the equilibrium—at least not according to the physics we understand—with signaling bounded by the limit of the speed of light. Cosmologists assess uniformity primarily using the temperature of the Cosmic Microwave Background (CMB), which is the thermal radiation emitted as the matter in the universe was cooling and transitioning from a conductive, opaque plasma to a neutral, transparent gas. The widely accepted standard is $T \approx 2.7255\,\mathrm{K}$ [21]. An Early CMB probe, the Cosmic Background Explorer, found the temperature variation from the mean to be on the order of $10^{-5}\,\mathrm{K}$ [22]. Quantifying the Horizon Problem further illustrates it.

We assume the early universe consisted of plasma containing causally connected photons as the source of the CMB photons at recombination when they were last scattered. In a non-relativistic universe, the distance between two isothermal objects traveling apart at the same speed would be simply $2vt$. But in Einstein's universe, the speed governing the causal connection between two photons moving apart cannot exceed c. We return to the eq. (1.15) definition of comoving distance at time t, cmd(t), now in integral form to define the distance light travels in an expanding universe. The maximum distance the photons that would become the CMB could be separated, that is, the maximum distance of causal

connection at last scattering, the proper distance $\mathrm{pd}(t_{ls})$, follows (c = 1):

$$\mathrm{cmd}(t_{ls}) = \int_0^{t_{ls}} \frac{dt}{a(t)} \;\rightarrow \tag{1.85}$$

$$\mathrm{pd}(t_{ls}) = a(t_{ls}) \int_0^{t_{ls}} \frac{dt}{a(t)} \tag{1.86}$$

$$= a(t_{ls}) \int_0^{a(t_{ls})} \frac{da}{a(t)\dot{a}(t)} \tag{1.87}$$

$$= a(t_{ls}) \int_0^{a(t_{ls})} \frac{da}{a^2(t)H(t)} \tag{1.88}$$

$$= a(t_{ls}) \int_0^{a(t_{ls})} \frac{da}{a^2(t)H_0} \left[\frac{\Omega_{m,0}}{a^3(t)} + \frac{\Omega_{r,0}}{a^4(t)} + \Omega_{\Lambda,0} + \frac{(1-\Omega_0)}{a^2(t)} \right]^{-1/2}. \tag{1.89}$$

In the last step, we have substituted the measurable form of the first Friedmann equation, eq. (1.81).

The Friedmann equation used in the last step derived from component densities that assumed idealized, single-component versions of the universe. In reality, the existing variety of components would have interacted, making the actual density formulas more complex. However, the distance estimate that results from the approximation proves suitable for demonstration of the Horizon Problem.

We next evaluate to $O(a)$ the maximum distance of causal connection at $a(t_{ls})$, given the Table 1.1 value $a(t_{ls}) \approx 9.1 \times 10^{-4}$:

$$\mathrm{pd}(t_{ls}) \approx a(t_{ls}) \int_0^{a(t_{ls})} \frac{da}{H_0} (a\Omega_{m,0} + \Omega_{r,0})^{-1/2} \tag{1.90}$$

$$= \frac{2a(t_{ls})}{H_0\,\Omega_{m,0}} \left[\sqrt{a(t_{ls})\Omega_{m,0} + \Omega_{r,0}} - \sqrt{\Omega_{r,0}} \right] \tag{1.91}$$

$$\approx 0.26\,\mathrm{Mpc}. \tag{1.92}$$

The final step in the process of quantifying the Horizon Problem is comparison of the maximum possible causal separation to the size of the last scattering surface. In their study [23], Halpern and Tomasello used Planck satellite data to estimate the radius of the observable universe in the present as 14,200 Mpc. The comoving distance equation results

in an estimate for the size of the universe at the time of last scattering,

$$\mathrm{pd}(t_{ls}) = a(t_{ls})\,\mathrm{cmd}(t_0) \tag{1.93}$$

$$\approx 12.9\,\mathrm{Mpc}. \tag{1.94}$$

Thus, the ratio of the maximum distance of causal connection to the radius of the universe at the time of last scattering was approximately $\frac{0.26\,\mathrm{Mpc}}{12.9\,\mathrm{Mpc}} \approx \frac{1}{50}$. Each causally connected portion of the CMB that should have been able to thermalize before the recombination photons that we observe today began to stream freely along their paths toward the Earth could not have been diametrically separated by more than $\frac{1}{50}$ the necessary distance. Cosmologists confronting the Horizon Problem ask the question, *How can we observe isothermal photons diametrically separated by 28,400 Mpc in the present when the maximum diametric separation of causal connection at the time of last scattering was about* $1/50$ *the diametric separation of the last scattering surface? How then,* cosmologists ask, *did they collectively equilibrate at a common temperature that is uniform to within the order of* 10^{-5} *K [11]?* A period of superluminal expansion provided by inflation could provide the missing causal connection.

1.5.3 The Monopole Problem

The additional *Monopole Problem* arises from the predictions of some GUT models [24, 25] that a phase transition breaks the symmetry between the strong and weak forces when the temperature of the universe drops to a level consistent with the energy scale 10^{16} GeV. A result would be the formation of a dust of massive magnetic monopoles, with a density that is subsequently proportional to a^{-3}, potentially thereby blocking the radiation and matter eras from taking place [15]. The Monopole Problem calls for a mechanism to reconcile the GUT prediction of the creation of these massive particles with our accepted understanding of the chronology of the early universe and current cosmological observation. Inflation could provide dilution that would make magnetic monopoles so few and far apart that finding them would be essentially impossible.

Chapter 2

Inflationary Cosmology

2.1 Old Inflation

In his groundbreaking research in 1981 [26], Alan Guth introduced the theory of inflation to address the unresolved horizon, flatness, and monopole problems. He proposed that Grand Unified Theory (GUT) phase transitions during the cooling of the universe produced the required solution of exponential expansion. However, his approach did not provide a satisfactory method to reheat a homogeneous, isotropic universe at the end of inflation.

Guth modeled the vacuum of space with constant energy density ρ_0 and a temperature T_c at the energy scale of a GUT theory. He envisioned the early universe not necessarily causally connected in its entirety but locally homogeneous, isotropic, and thermalized. A GUT phase transition initiated supercooling that trapped the scalar field in the lowest energy level ρ_0 of the unstable false vacuum state. The universe supercooled orders of magnitude below T_c, causing inflationary expansion sufficient to solve the Horizon, Flatness, and Monopole Problems. During the supercooling, the scalar field underwent quantum tunneling at the energy density of the vacuum. *Bubbles*, randomly distributed regions of space, formed at a temperature below that of the phase transition. These bubbles, which contained the scalar field, then expanded and nucleated. At an electroweak phase transition temperature T_s, collisions occurred among the bubbles to release the latent heat stored in their walls. The collisions reheated and thermalized the universe to a temperature T_r on the order of T_c.

The initial environment was one of constant entropy in a comoving volume undergoing adiabatic expansion,

$$\frac{d}{dt}(sR^3) = 0, \tag{2.1}$$

where s and R were the entropy density and radius of curvature, respectively, of the causally connected universe. Guth proposed that the GUT phase transition began non-adiabatic expansion with respect to initial total entropy S_0,

$$S_0 \equiv R^3 s, \tag{2.2}$$

so that volume expansion factor Z acted on entropy S_0 resulting in total entropy today S_p,

$$S_p = Z^3 S_0. \tag{2.3}$$

Inflation ended at the reheating temperature T_r, which determined the expansion factor for the inflationary environment,

$$Z \approx \frac{T_r}{T_s}. \tag{2.4}$$

As the universe expanded, the constant energy density ρ_0 of the vacuum came to dominate the first Friedmann equation and thus define the rate of expansion of the inflationary universe. Guth assumed the scalar field expanded relativistically, so that $T(t) \propto a(t)^{-1}$, or $T(t) = Ca(t)^{-1}$ with constant C, for the redshifted field:

$$\dot{a}(t) = -\frac{\dot{T}(t)\,C}{T(t)^2} \tag{2.5}$$

$$\frac{\dot{a}(t)}{a(t)} = -\frac{\dot{T}(t)}{T(t)}. \tag{2.6}$$

We then have the Friedmann equation in terms of the scale factor $a(t)$ and the temperature,

$$\frac{\dot{a}(t)}{a(t)} = \sqrt{\frac{8\pi G}{3}\rho_0} \tag{2.7}$$

$$\frac{\dot{T}(t)}{T(t)} = -\sqrt{\frac{8\pi G}{3}\rho_0}. \tag{2.8}$$

Solving the differential equation gives

$$\frac{T(t_i)}{T(t_f)} = e^{\sqrt{\frac{8\pi G}{3}\rho_0}\,(t_f - t_i)}. \tag{2.9}$$

Finally, after resubstituting the scale factor,

$$a(t_f) = a(t_i)\, e^{\sqrt{\frac{8\pi G}{3}\rho_0}\,(t_f - t_i)} = a(t_i)\, e^{H(t_f - t_i)}, \tag{2.10}$$

yielding the Hubble parameter $H = \sqrt{\frac{8\pi G}{3}\rho_0}$, the constant inflationary rate of expansion.

Inflation ended when enough bubbles collided and coalesced to form an infinite, reheated universe in the true vacuum state. However, Guth acknowledged a major difficulty of his model. The rate of nucleation was problematic. With a rate that was too fast, inflation would not last long enough to solve the Horizon, Flatness, and Monopole Problems. But too slow a rate would result in not enough bubbles to collide and reheat the universe. No rate could accomplish both sufficient exponential expansion and reheating [27].

The inflation proposed by Guth was not capable of terminating successfully. He acknowledged the difficulty his mechanism created: An exit from the false vacuum that drives inflation involved quantum tunneling from a false to the true vacuum state, an effect that would occur primarily in localized bubbles—that is, discrete regions subsequently characterized by the Klein-Gordon scalar field that drives inflation (the inflaton ϕ) having settled into its true vacuum state. Meanwhile, expansion of space would continue between the bubbles (where such tunneling had not yet occurred), and as a result, we would expect to see parcels of non-uniform space today. Intersecting bubbles would have similar effects. This model of inflation thus predicted a universe inconsistent with observation; Guth's original theory lacks what cosmologists call a *graceful exit*, a problem solved by Andrei Linde with his theory of new inflation.

2.2 New Inflation

In 1982, inflation pioneer Andrei Linde sought to solve the graceful exit problem with a new theory, *slow-roll inflation* [28]. Instead of starting in a false vacuum, the inflaton rolls

down a potential energy plateau to a minimum where it oscillates around a true vacuum state, which figure 2.1 depicts schematically. The assumption that the potential energy of the inflaton dominates the kinetic energy for a sufficient time results in exponential inflation.

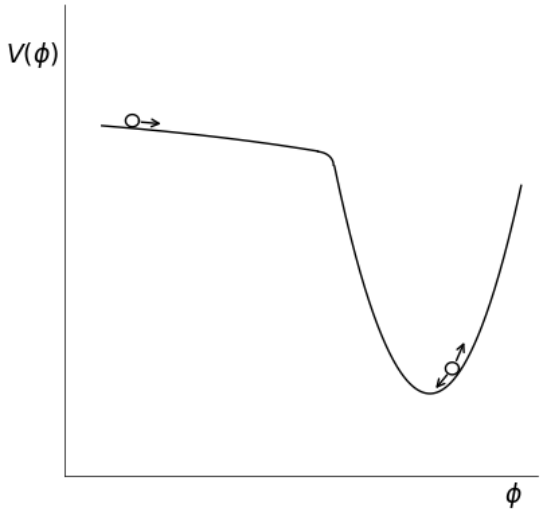

Figure 2.1 Slow roll inflation requires a plateau to generate enough inflationary expansion to solve the Horizon, Flatness, and Monopole Problems. After inflation, the inflaton oscillates around a minimum potential during a period of reheating, reviewed in chapter 2.5.

The Lagrangian for the inflaton, the Klein-Gordon scalar field with an as yet undefined potential energy function $V(\phi)$ is well-known:

$$\mathcal{L} = \frac{1}{2}\partial_\mu\phi\partial^\mu\phi - V(\phi). \tag{2.11}$$

We assume that the scalar field has a negligible spatial dependence, so that $\phi = \phi(t)$. Varying the action of the Lagrangian in gravity defined by the RW metric yields the equation of motion,

$$\ddot{\phi} + 3\frac{\dot{a}}{a}\dot{\phi} + \frac{\partial V(\phi)}{\partial\phi} = 0. \tag{2.12}$$

In terms of the expansion rate of the universe, the Hubble parameter H, the equation of motion becomes

$$\ddot{\phi} + 3H\dot{\phi} + V(\phi)_{,\phi} = 0. \tag{2.13}$$

The comma linked to the potential of the inflaton denotes the partial derivative with respect to ϕ.

Noether's theorem leads to the derivation of the stress-energy tensor,

$$T^{\mu\nu} = \frac{\partial \mathcal{L}}{\partial(\partial_\mu \phi)} \partial^\nu \phi - g^{\mu\nu} \mathcal{L}. \tag{2.14}$$

Applied to the Lagrangian and with the indices lowered, the stress-energy tensor is

$$T_{\alpha\beta} = \partial_\alpha \phi \partial_\beta \phi - g_{\alpha\beta} \left[\frac{1}{2} \partial_\mu \phi \partial^\mu \phi - V(\phi) \right] \tag{2.15}$$

$$= \partial_\alpha \phi \partial_\beta \phi - \frac{1}{2} g_{\alpha\beta} \left[\dot{\phi}^2 - \nabla^2 \phi \right] + g_{\alpha\beta} V(\phi). \tag{2.16}$$

With the inflaton scalar field $\phi = \phi(t)$,

$$T_{\alpha\beta} = \partial_\alpha \phi \partial_\beta \phi - \frac{1}{2} g_{\alpha\beta} \dot{\phi}^2 + g_{\alpha\beta} V(\phi). \tag{2.17}$$

Only the diagonal elements survive:

$$T_{tt} = \partial_t \phi \partial_t \phi - \frac{1}{2} g_{tt} \dot{\phi}^2 + g_{tt} V(\phi) \tag{2.18}$$

$$= \frac{1}{2} \dot{\phi}^2 + V(\phi). \tag{2.19}$$

$$T_{ii} = \partial_i \phi \partial_i \phi - \frac{1}{2} g_{ii} \dot{\phi}^2 + g_{ii} V(\phi) \tag{2.20}$$

$$= -\frac{1}{2} g_{ii} \dot{\phi}^2 + g_{ii} V(\phi). \tag{2.21}$$

These elements equate to those of the rest frame perfect fluid to produce expressions for the energy density and pressure of the inflaton:

$$\rho = \frac{1}{2} \dot{\phi}^2 + V(\phi). \tag{2.22}$$

$$p = \frac{1}{2} \dot{\phi}^2 - V(\phi). \tag{2.23}$$

The Hubble friction term in eq. (2.13) regulates the slow roll condition of inflation, understood to arise with the expansion of space as its physical basis, such that kinetic energy is negligible with respect to the potential energy that drives inflation, and the magnitudes of both the density and pressure of the inflaton become approximately equal to the potential:

$$\rho = \frac{1}{2}\dot{\phi}^2 + V(\phi) \approx V(\phi) \tag{2.24}$$

$$p = \frac{1}{2}\dot{\phi}^2 - V(\phi) \approx -V(\phi). \tag{2.25}$$

The negative pressure arising from the perfect fluid assumption acts repulsively on the left-hand side of the Einstein field equations in the same way as a cosmological constant, an effect opposite to that of energy and mass. Within bubbles that tunnel to the true vacuum, inflatons undergo oscillatory decay leading to the end of inflation. However, regions that fail to tunnel, trapping inflatons that never decay in the false vacuum, expand forever, like a universe defined by the de Sitter solution to the Einstein equations.

2.2.1 The Nature of Inflation

The universe is always expanding, so that the time derivative of the scale factor is positive, and we define inflation as expansion characterized by acceleration of the scale factor, specifically, when $\ddot{a} > 0$. We start with the relationship between the energy density and pressure of the particles in space, the equation of state derived in section 1.3 from the Fluid Equation,

$$w = \frac{p}{\rho}. \tag{2.26}$$

We now use the second Friedmann equation, the acceleration equation, to determine the necessary condition for inflation with $\ddot{a} > 0$:

$$\frac{\ddot{a}}{a} = -\frac{4\pi G}{3}(\rho + 3p) > 0. \tag{2.27}$$

$$\rho + 3p < 0. \tag{2.28}$$

$$\frac{p}{\rho} < -\frac{1}{3} \;\rightarrow\; w_{\text{infl}} < -\frac{1}{3}. \tag{2.29}$$

The necessary condition for density, $\rho > 0$, implies that pressure is in fact less than zero, $p < 0$, which is consistent with negative pressure in the stress-energy tensor of the Einstein field equations driving expansion of the lattice of spacetime on the left-hand side.

The first of two parameters that constrain inflation, ϵ, supports the inflationary expansion. The equation of state for the inflaton, based on equations 2.22 and 2.23, is

$$w_\phi = \frac{\frac{1}{2}\dot{\phi}^2 - V(\phi)}{\frac{1}{2}\dot{\phi}^2 + V(\phi)}. \tag{2.30}$$

Assuming that the potential energy dominates, so that $V(\phi) \gg \frac{1}{2}\dot{\phi}^2$,

$$w_\phi \approx \frac{-V(\phi)}{V(\phi)} = -1, \tag{2.31}$$

which satisfies the necessary condition that $w_{\text{infl}} < -\frac{1}{3}$ of section 2.2.1.

We derive the first parameter as follows:

$$H^2 + \dot{H} = \left(\frac{\dot{a}}{a}\right)^2 + \frac{d}{dt}\left(\frac{\dot{a}}{a}\right) = \left(\frac{\dot{a}}{a}\right)^2 + \frac{\ddot{a}}{a} - \left(\frac{\dot{a}}{a}\right)^2 = \frac{\ddot{a}}{a}. \tag{2.32}$$

Let

$$H^2 + \dot{H} = H^2\left(1 + \frac{\dot{H}}{H^2}\right) = H^2(1 - \epsilon) \;\rightarrow\; \epsilon = -\frac{\dot{H}}{H^2}. \tag{2.33}$$

After evaluating $\dot{H}$ as

$$\dot{H} = \frac{d}{dt}\left(\frac{\dot{a}}{a}\right) = \frac{\ddot{a}}{a} - \left(\frac{\dot{a}}{a}\right)^2, \tag{2.34}$$

we substitute the acceleration equation and the first Friedmann equation in flat space into equation 2.34 and find ϵ for $V(\phi) \gg \frac{1}{2}\dot{\phi}^2$:

$$\epsilon = -\frac{\dot{H}}{H^2} = \frac{3(\rho + p)}{2\rho} = \frac{3\dot{\phi}^2}{\dot{\phi}^2 + 2V(\phi)} \ll 1 \tag{2.35}$$

We have an inflationary period with $w_\phi = -1$ subject to the constraint that the first parameter $\epsilon \ll 1$.

The *slow-roll* condition implies $\ddot{\phi} \rightarrow 0$, so that the equation of motion of the scalar field,

$$\ddot{\phi} + 3H\dot{\phi} + V(\phi)_{,\phi} = 0, \tag{2.36}$$

reduces to

$$3H\dot{\phi} = -V(\phi)_{,\phi}. \tag{2.37}$$

We interpret the result to indicate that under the constraint that $\epsilon \ll 1$, the potential of the inflaton drives the expansion of space, which itself provides the slow roll condition.

The need for inflation to come to an end such that $\ddot{a} = 0$ motivates derivation of the second parameter, η. We rearrange the equation of motion 2.13, so that

$$\frac{\ddot{\phi}}{3H\dot{\phi}} + \frac{V(\phi)_{,\phi}}{3H\dot{\phi}} = -1. \tag{2.38}$$

For $\ddot{\phi} \to 0$, we define the second parameter as

$$\eta = \frac{\ddot{\phi}}{3H\dot{\phi}} \to 0, \tag{2.39}$$

in which case

$$V(\phi)_{,\phi} \approx -3H\dot{\phi}. \tag{2.40}$$

Inflation ends as the second parameter approaches zero, and the final result indicates that the decrease in the ratio of the derivative of $V(\phi)$ with respect to ϕ to the derivative of ϕ in terms of time approximates the Hubble parameter during inflation.

The expansion rate of the universe during inflation depends on the potential of the inflaton and is exponential. To start, we expand the first Friedmann equation in flat space and the acceleration equation in terms of the expressions for ρ and p:

$$H^2 = \frac{8\pi G}{3}\rho = \frac{8\pi G}{3}\left[\frac{1}{2}\dot{\phi}^2 + V(\phi)\right]; \tag{2.41}$$

$$\frac{\ddot{a}}{a} = \dot{H} + H^2 = -\frac{4\pi G}{3}(\rho + 3p) = -\frac{8\pi G}{3}[\dot{\phi}^2 - V(\phi)]. \tag{2.42}$$

Substitution leaves

$$\dot{H} = -4\pi G\,\dot{\phi}^2. \tag{2.43}$$

The first parameter constraining inflation becomes

$$\epsilon = -\frac{\dot{H}}{H^2} = \frac{4\pi G\,\dot{\phi}^2}{H^2}, \tag{2.44}$$

and after imposing the constraint that $\epsilon \ll 1$,

$$4\pi G\,\dot{\phi}^2 \ll H^2. \tag{2.45}$$

Now the first Friedman equation reduces to

$$H^2 \approx \frac{8\pi G}{3} V(\phi). \tag{2.46}$$

We thus confirm the interesting insight that the rate of expansion of the universe during inflation depends on the potential of the inflaton.

In this regime of density and pressure of eqs. (2.24) and (2.25), respectively, the Friedmann acceleration equation governing $\ddot{a}$ is

$$\frac{\ddot{a}(t)}{a(t)} = -\frac{4\pi G}{3}(\rho + 3p) = \frac{8\pi G}{3}\rho. \tag{2.47}$$

Thus the expansion of space undergoes inflationary acceleration, $\frac{\ddot{a}}{a} > 0$, as a result. The first Friedman equation,

$$H^2 + \frac{k}{a^2} = \frac{8\pi G}{3}\rho, \tag{2.48}$$

with $H^2 = \left(\frac{\dot{a}}{a}\right)^2 \gg \frac{k}{a^2}$, yields the scale factor solution

$$a(t) = a_0 e^{Ht}. \tag{2.49}$$

This is the exponential expansion of space predicted by the theory of slow-roll inflation [18, 29]. A period of superluminal expansion would explain the homogeneity and isotropy of the observable universe by providing the necessary causal connection to solve the Horizon Problem. Superluminal expansion would also flatten the spatial curvature and decrease the density of magnetic monopoles. Numerical analysis provides insight into the question of the number of e-folds of expansion necessary to resolve these problems. The amount by which the cosmos expands is normally expressed in terms of the number of times the size has increased by a constant factor—in other words, the number of the e-folds (or nepers) $N = \log \frac{a(t_f)}{a(t_i)}$. However, this solution comes with its own associated shortcoming: Producing an outcome consistent with modern observations demands very specific initial conditions.

2.2.2 The Inflation Solution

Inflation provides a solution to the as yet otherwise intractable Flatness, Horizon, and Monopole Problems. Regarding the Flatness Problem, as Table 1.1 shows, the scale factors of the single-component eras numerically reduce the curvature of space going backward in time, due to their proportionality to a fractional exponent. Extending the timeline of the table to an even earlier era reduces the measure of flatness, $\Omega_k = 1 - \Omega(t)$, to an infinitesimal level. At the end of inflation with section 3.1 estimates $t_f \approx 4 \times 10^{-39}$ s and $a(t_f) \approx 10^{-29}$, calculation yields $\Omega_k \approx 10^{-57}$.

The derivation of Ω_k, eq. (1.82), from the first Friedmann equation enables us to determine the effect of inflation on curvature, starting with expressions for flatness at the beginning and end of inflation:

$$\Omega_k(t_i) = -\frac{k}{a^2(t_i)H^2(t_i)} \tag{2.50}$$

$$\Omega_k(t_f) = -\frac{k}{a^2(t_f)H^2(t_f)}. \tag{2.51}$$

We equate the curvature constants, because an open or closed universe remains open or closed, and assume the Hubble parameter is constant over the inflationary period.

$$\Omega_k(t_i)a^2(t_i) = \Omega_k(t_f)a^2(t_f). \tag{2.52}$$

$$\Omega_k(t_f) = \Omega_k(t_i)\frac{a^2(t_i)}{a^2(t_f)} = \Omega_k(t_i)e^{-2N}. \tag{2.53}$$

Within reasonable tolerances for early-universe parameter assumptions, we find the same order of magnitude measures of flatness as the extended Table 1.1 value that evolves to the Planck Collaboration observation today. For example, for a maximally open universe, in which $\Omega_k = 1$, the flatness measure at the end of inflation is $\Omega_k(t_f) \approx 10^{-57}$ with $N = 65$. Thus, exponential inflation flattens the curvature of space to an infinitesimal level, and during the subsequent single-component eras, the scale factors proportional to fractional exponents curve space to the nearly flat universe observed today with $\Omega_k \approx 7 \times 10^{-4}$.

Analyzing the effect of exponential inflation applied to distances resolves the Horizon Problem. We have found that the universe without inflation could not have thermalized subsequent to the formation of the last scattering surface. We require that the causal connection in the early universe expand sufficiently by the time of the creation of the last scattering surface to encompass the region of space destined to grow to the size of the observable isothermal universe today. The analysis here evaluates the relation between the original early-universe causal connection and that region at the time of the last scattering surface, t_{ls}, to determine the number of inflationary e-folds needed.

We start with the expression for the causal connection,

$$\mathrm{pd}(t_{ls}) = a(t_{ls}) \int_0^{t_{ls}} \frac{dt}{a(t)}, \tag{2.54}$$

and expand it in terms of each constituent era:

$$\mathrm{pd}(t_{ls}) = a(t_{ls}) \left[\int_0^{t_i} \left(\frac{t_i}{t}\right)^{1/2} \frac{dt}{a(t_i)} + \int_{t_i}^{t_f} \frac{dt}{a(t_i) e^{H(t-t_i)}} + \int_{t_f}^{t_{ls}} \frac{dt}{a(t)} \right]. \tag{2.55}$$

Assuming the inflationary term will dominate, we eliminate the third term to obtain

$$\mathrm{pd}(t_{ls}) = \frac{a(t_{ls})}{a(t_i)} \left(2t_i + H^{-1}\right) - H^{-1} \approx \frac{a(t_{ls})}{a(t_i)} \left(2t_i + H^{-1}\right) = \frac{a(t_{ls}) e^N}{a(t_f)} \left(2t_i + H^{-1}\right) \tag{2.56}$$

Solving for N yields

$$e^N = \left[\frac{a(t_f)}{a(t_{ls})(2t_i + H^{-1})} \right] \mathrm{pd}(t_{ls}). \tag{2.57}$$

Based on the Table 1.1 value for $a(t_{ls})$, the previously determined $\mathrm{pd}(t_{ls})$, and an estimate that inflation began at $t_i = 10^{-42}$ s [12], we find $N \approx 68$ and thus, within reasonable tolerances for early-universe parameter assumptions, a numerical basis for support of the theory of New Inflation as a valid solution to the Horizon Problem.

Cosmologists have applied a variety of approaches to estimating the amount of inflation necessary to solve the Horizon, Flatness, and Monopole Problems. Linde [29] reports that a quadratic inflaton potential creates a wavelength for the inflaton comparable in size to our observable universe after about 60 e-folds. In a detailed analysis, Lyth [30] finds that for

a quartic inflaton potential, a range of e-fold values from 47 to 61 results in a universe on the present scale. He further explains that at a minimum, more than 14 e-folds are needed to generate perturbations leading to structure formation, and that an extended period of domination of the inflaton kinetic term could increase his estimates of N by nearly 14, therefore concluding with an estimate of $14 < N < 75$.

Other researchers have performed analyses to determine the number of e-folds required to solve specific inflationary problems [31]. Solving the Horizon Problem entails that the comoving Hubble radius at the beginning of inflation $[a(t_i)H(t_i)]^{-1}$ must contain what has become the comoving Hubble radius today $[a(t_0)H(t_0)]^{-1}$, so that the comoving $[a(t_0)H(t_0)]^{-1}$ could have thermalized before expanding through the post-inflationary epochs of the universe up to the present. The Hubble radius is the distance light travels in time $t = H^{-1}$. Thus we have

$$[a(t_i)H(t_i)]^{-1} \geq [a(t_0)H(t_0)]^{-1} \tag{2.58}$$

$$\frac{1}{H(t_i)} \geq \frac{1}{H(t_0)}\frac{a(t_i)}{a(t_0)} = \frac{1}{H(t_0)}\frac{a(t_f)}{a(t_0)}\frac{a(t_i)}{a(t_f)} = \frac{1}{H(t_0)}\frac{a(t_f)}{a(t_0)}e^{-N} \tag{2.59}$$

$$-N \leq \log\left[\frac{H(t_0)}{H(t_i)}\frac{a(t_0)}{a(t_f)}\right] = \log\left[\frac{H(t_0)}{H(t_i)}\frac{T(t_f)}{T(t_0)}\right] = \log\left[\frac{H(t_0)}{T(t_0)}\frac{T(t_f)}{H(t_i)}\right]. \tag{2.60}$$

In eq. (2.60) we use the inverse relation between the scale factor and temperature, which is derived in appendix C for reference. Parameter values $T(t_0) \approx 2.75\,\mathrm{K}$ and $H(t_0) \approx 100\,\mathrm{km/s/Mpc}$ lead to

$$N \geq 67 + \log\left[\frac{H(t_i)}{T(t_f)}\right], \tag{2.61}$$

which indicates that N is at least 67, because the temperature $H(t_i)$ represents is greater than $T(t_f)$.

2.3 Chaotic Inflation

Although the underlying physics of inflation (such as the existence of the inflaton field) remains unsubstantiated experimentally, the framework of inflation is widely accepted among

cosmologists as a way of providing an underlying solution to various cosmological problems. Over the years, researchers have revised the concept by devising a diverse body of new theories. For our purposes, we shall focus on Linde's solution to the problem of the requirement of specific initial conditions in the slow roll theory. In 1983, he published his theory of *chaotic inflation* [32]. In its simplest version [29], the inflaton potential has the form $V(\phi) = \frac{1}{2}m^2\phi^2$. The plateau is absent, and in an expanding universe, the friction term $3H\dot{\phi}$ in the inflaton equation of motion (2.36) has the effect of restricting the motion of the inflaton, as the slow roll plateau does, resulting again in exponential expansion. Figure 2.2 shows the chaotic inflation potential in contrast to that of figure 2.1.

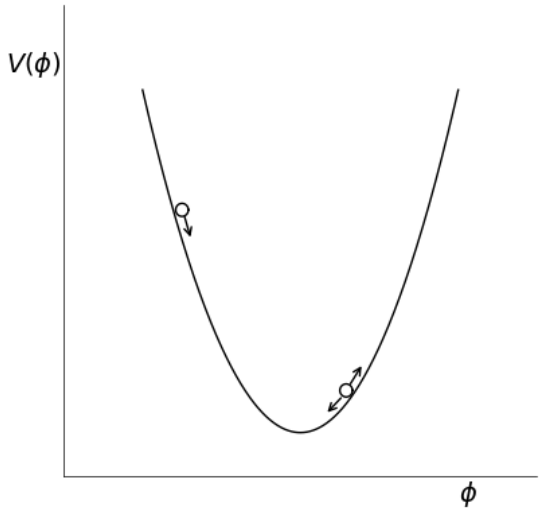

Figure 2.2 In chaotic inflation, the effects of the friction term in the equation of motion replace that of the slow roll plateau in keeping the inflaton from moving to the true vacuum too quickly, after which the inflaton oscillates around its minimum potential during reheating.

2.4 The Physics of the Cosmic Microwave Background

Large Scale Structure

Gravitationally bound structure, defined as structure larger than galactic scales, is a feature of the universe that supports inflationary theory. Quantum fluctuations of the inflaton arising during inflation cause curvature and density inhomogeneities subject to gravitational instability based on the physics of General Relativity. Matter accumulates in gravitationally bound density perturbations and disperses in empty space during expansion in quantities sufficient in time for the formation of stars and larger and larger structure, until satellites map the pattern throughout the universe today. The Milky Way, for example, resides in structure of increasing size, from the Local Group containing more than 54 galaxies, to the Virgo Supercluster, and then to the Laniakea Supercluster. Although the universe is homogeneous when viewed on large scales, the statistical distribution of large scale structure is not random. The image generated by the Sloan Digital Sky Survey (SDSS) in figure 2.3 shows a map of redshift radiation across a swath of the upper hemisphere. By contrast, a random distribution would spread galaxies in a uniform pattern, which would lack the distinctive clusters of structure in figure 2.3.

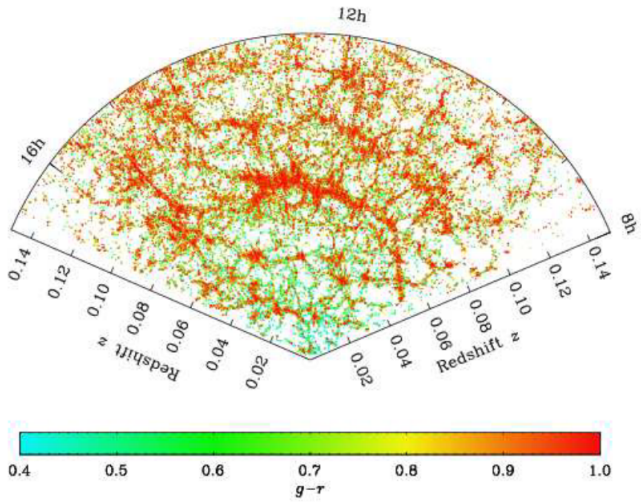

Figure 2.3 The SDSS redshift map of the structure of galaxies of the north Galactic cap within 4° of the plane of Earth's equator. Figure from Ref. [33].

A qualitative description of the complicated dynamics of the origin of large scale structure begins with the inflaton subject to quantum fluctuations [34],

$$\phi(\mathbf{x}, t) \;\rightarrow\; \phi(t) + \delta\phi(\mathbf{x}, t), \tag{2.62}$$

crossing the Hubble radius during the inflationary period $t \sim H^{-1}$. As the field exits the Hubble radius, the fluctuations cause time fluctuations that affect the end of inflation and expansion, resulting in curvature and associated density perturbations. Outside the Hubble parameter, the inflatons begin to behave classically, such that the amplitudes remain constant while the wavelengths continue both to expand exponentially and to generate fluctuations. As the Hubble radius expands after inflation along with the universe, the perturbations reenter the Hubble radius. At recombination, the photons that start streaming toward observers in the present day reveal the effects of the density perturbations imprinted on the last scattering surface. The density perturbations that reenter the Hubble radius at recombination become increasingly irregular as time progresses, and they coalesce under gravitational instability to evolve eventually into large scale structure.

We note a simplified proportionality between density and the Hubble parameter and time according to the first Friedmann equation in flat space

$$\rho \sim H^2 \sim t^{-2} \tag{2.63}$$

$$|\,\delta\rho\,| \sim |\,-t^{-3}\delta t\,| \tag{2.64}$$

$$\frac{\delta\rho}{\rho} \sim \frac{\delta t}{t}. \tag{2.65}$$

The differential of the inflaton with respect to time gives an expression for δt,

$$\dot{\phi} = \frac{d\phi}{dt} = \frac{\delta\phi}{\delta t} \;\rightarrow\; \delta t = \frac{\delta\phi}{\dot{\phi}} = \frac{H}{2\pi\dot{\phi}}, \tag{2.66}$$

where in the last step we substituted the derived dependence of the inflaton perturbation on the Hubble parameter, $\delta\phi = \frac{H}{2\pi}$ [34]. Eqs. (2.65) and (2.66) yield

$$\frac{\delta\rho}{\rho} \sim \frac{1}{t}\frac{H}{2\pi\dot{\phi}} = \frac{H^2}{2\pi\dot{\phi}}. \tag{2.67}$$

The left-hand side is responsive to experimental observation; the right-hand side is subject to numerical evaluation. Agreement supports the proposition that the dynamics of physics in inflationary theory was the source of large scale structure. The discovery of temperature

anisotropies experimentally confirmed the existence of density perturbations.

Temperature Anisotropies

The most notable accomplishment of the early CMB probe, the 1989 Cosmic Background Explorer (COBE), which also showed that CMB radiation remarkably simulates that of a blackbody, was the discovery of temperature anisotropies. Temperature anisotropies are variations from isotropy of the CMB, measured as brightness on angular scales. The Nobel-winning accomplishments of COBE provided a strong impetus for the proposal and approval of more ambitious projects, the 2003 Wilkinson Microwave Anisotropy Probe (WMAP) and the 2013 Planck satellite. Figure 2.4 compares sky maps of temperature anisotropies generated by the COBE and Planck missions. The Planck mission improved the resolution in angular scale from the 10° of COBE to better than 0.2°. The COBE map was the result of 4 years of observational data, which had to be washed to eliminate noise and the Dipole effect caused by motion of the satellite, anchored ultimately in the Local Group, in the CMB rest frame.

The temperature anisotropies provide experimental confirmation of the physics [11]. During the time prior to recombination, curvature perturbations cause temperature perturbations due to the *Sachs-Wolfe effect* acting on photon modes on super-horizon scales, derived as [37]

$$\frac{\delta T}{T} = \frac{\delta a}{a}. \tag{2.68}$$

The Sachs-Wolfe effect combines a redshift as photons climb out of the potential well of contracted space offset by a gravitational time delay, with both driven by the theory of General Relativity. At recombination, the photons that begin streaming toward detectors in the present carry the signature of the temperature perturbations. Density perturbations associated with the same curvature perturbations cross the last scattering surface at the same time to seed large scale structure, of which the Earth finds itself a part.

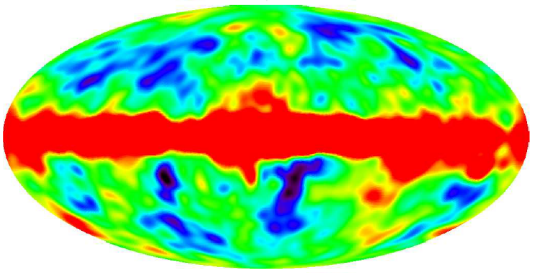

(a)

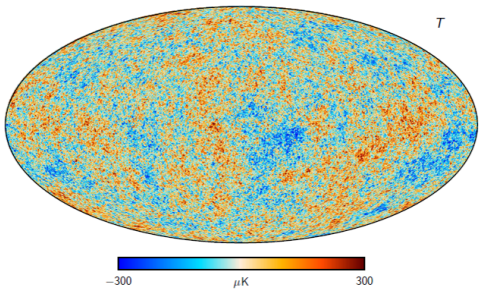

(b)

Figure 2.4 The contrast between the detail of graph (a) of the 1993 COBE map of temperature anisotropies and that of graph (b), the 2018 Planck satellite map at an enhanced angular scale. The Planck rendering has also eliminated the galactic plane of the Milky Way, which appears as the broad horizontal red band in the COBE image. Figures from Refs. [35] and [36], respectively.

The enhanced angular resolution of the Planck satellite has been the source of much information about the physics of the CMB. Although some of the effects occur after the period of interest here and recombination, a brief review of the work of the Planck Collaboration regarding temperature anisotropies is illustrative of the advancement in CMB cosmology over the past three decades. The symmetry of the isotropy and homogeneity of the CMB allows expansion of the temperature anisotropies in spherical harmonics [11],

$$\frac{\delta T}{T}(\theta,\phi) = \sum_{l=0}^{\infty}\sum_{m=-l}^{l} a_{lm}Y_{lm}(\theta,\phi). \tag{2.69}$$

After defining the correlation function between points defined by $\hat{n}$ and $\hat{n}'$ separated by θ in the sphere as

$$C(\theta) = \left\langle \frac{\delta T(\hat{n})}{T_0}\frac{\delta T(\hat{n}')}{T_0} \right\rangle, \tag{2.70}$$

where $\delta T(\hat{n}) = T(\hat{n}) - T_0$ and T_0 is the average temperature of the CMB calculated over all pairs of points at the angular scale, we have an expression for the form of the correlation function responsive to observation,

$$C(\theta) = \frac{1}{4\pi} \sum_{l=0}^{\infty} (2l + 1)\, C_l\, P_l\, (cos\, \theta). \tag{2.71}$$

The Planck Collaboration produced statistical data displayed as angular power spectrum brightness, that is, the correlation function, adjusted for various noise effects as a function of multipole moment of the spherical harmonics of temperature anisotropies. Figure 2.5 captures the observational results. On the left of the dominant peak, that is, the small multipole moments and large angular scales, is the brightness profile for the anisotropies COBE measured due to the Sachs-Wolfe effect. Physics effects after recombination generate the dominant peak, the two smaller peaks to the right, and the rest of the detail of the brightness profile.

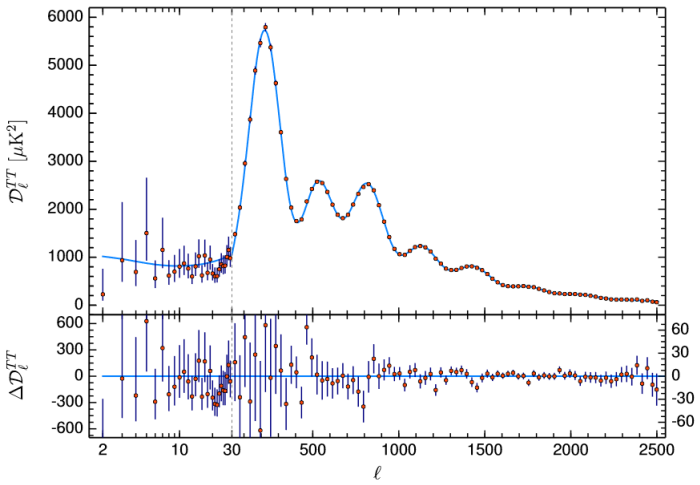

Figure 2.5 The temperature power spectrum fitted to observation. The lower part of the graph shows residuals of the fit, that is, the difference when the observations are compared to the predicted fit of Planck's Lambda Cold Dark Matter (ΛCDM) model. Figure from Ref. [38].

Cosmologists classify temperature anisotropies according to the scale and timing on which the physics that creates them operates [39]. Physics acting on scales larger than the Hubble radius prior to recombination imprint primary anisotropies on the last scattering

surface as the anisotropies reenter the horizon. Between recombination and the present, physics acting on photons streaming toward our detectors produce secondary anisotropies.

Primary anisotropies, all a consequence of inflation, include the following types:

- The Sachs-Wolfe effect, described above, is reflected in the COBE results. As space expands, photons must climb out of the potential well of the flattening curvature perturbations.

- At the creation of the last scattering surface, electrons that scatter photons have a velocity relative to the rest frame of the CMB and introduce a Doppler effect.

- Curvature perturbations bring about baryonic perturbations and the changes in densities cause temperature anisotropies. Theoretical physics had predicted these perturbations, including the influence of cold dark matter. However, although the temperature anisotropies caused by the Doppler effect were known empirically, experimental confirmation of perturbations had to await the resolution provided by COBE.

- Also due to inflation, outside the horizon two primary anisotropies on sub-horizon scales arise from modes within the speed of sound horizon of waves in the plasma of baryons and photons:

  - The plasma oscillates adiabatically in acoustic waves due to the opposing forces between the gravitational attraction of baryons and dark matter and pressure from photons. The density anisotropies imprinted on the last scattering surface include additional temperature anisotropies of the acoustic waves.

  - Recombination occurred at the time at which the photon mean free path exceeded the Hubble radius, so that photons were able to begin streaming freely through space without absorption by hydrogen. However, the formation of the CMB last scattering surface required a duration of time. While some photons began streaming freely, others continued to be absorbed and emitted, until the

last scattering surface was completed. During that interim period, in a process called *Silk Damping*, temperature anisotropies underwent isotropic degrading by photon absorption and then emission in all directions.

The following secondary anisotropies came about from the physics of cosmology in the evolution of the universe after recombination and are not directly related to inflation or scales greater than the Hubble radius:

- After reionization of hydrogen by electrons emitted from relatively newly formed stars, galaxies, and quasars, photons scatter off free electrons. *Thomson scattering* is isotropic, thereby erasing the anisotropies originally imprinted at the time of the last scattering surface.

- The curvature distortions of large scale structure disrupts the anisotropy profile of photons because of the influence of changes to the gravitational potential as the photons pass into and out of its influence. The effect, called the *integrated Sachs-Wolfe effect* because determining the magnitude involves line-of-sight integration, results as the time-dependent potential changes while photons traverse the potential well, and the effects of falling into the well and climbing out of it do not offset.

- Photons experience deflection due to General Relativity by all the objects that make up large scale structure.

- The *Sunyaev-Zeldovich effect*, isotropic scattering of photons by clusters of galaxies and gases, alters the temperature anisotropies originally imprinted.

A few additional comments conclude this section. In the Planck spectrum of figure 2.5, the large scale spectrum measured by COBE lies to the left of the dominant peak, where the Sachs-Wolfe effect dominates, ending at about multipole moment 13. The relatively flat spectrum in this region is due to the resolution of COBE at a large angular scale, which

captures anisotropies generated outside the Hubble radius. On that scale, the frozen amplitudes of inflaton perturbations generate density perturbations with amplitudes also all of approximately the same size. Thus, we see the impact of the Sachs-Wolfe effect, reflecting the density perturbations, as a nearly flat spectrum as measured by COBE. Finally, overall, one of the primary successes of the Planck Collaboration was a set of estimates of component densities and cosmological parameters consistent with those that model a ΛCDM universe.

The Scalar Spectral Index

Further theoretical analysis of the spectrum of anisotropies provides observable constraints on models of inflation. Observations of large scale structure of the SDSS sky survey are consistent with Gaussian density perturbations. Similarly, WMAP characterized the CMB perturbations as Gaussian [40, 41]. The correlation function of a Gaussian random scalar field, like the inflaton of slow roll inflation, encodes all the statistical properties of the field. As such, in momentum space, the power spectrum with modes k of of the CMB temperature anisotropies distributed over its multipole moments has the form

$$P_k \propto k^{n_s - 1}. \tag{2.72}$$

The scalar spectral index n_s becomes

$$n_s - 1 = \frac{d \log P_k}{d \log k}. \tag{2.73}$$

A spectral index of 1 produces a flat, scale-invariant spectrum. The variation from a flat spectrum manifests itself as a "tilt" in the graph of the spectrum. The observations of inflaton perturbations imprinted on the CMB last scattering surface are the correlation function of the temperature anisotropies described previously. We start by expressing the power spectrum in terms of the potential of the inflaton V [42],

$$P_k = \frac{1}{75\pi^2 M_p^2} \frac{V^3}{V'^2}, \tag{2.74}$$

with the Planck mass M_p and the potential differentiated with respect to ϕ.

We will need the slow-roll parameters ϵ and η of eqs. (2.35) and (2.39), respectively, as functions of V. The first parameter ensures that the potential changes slowly when $\epsilon \ll 1$, which accounts for the *slow roll*, and inflation terminates under the condition that η, also defined as very much less than 1, approaches zero. To express ϵ as a function of the potential, we differentiate the first Friedmann equation in flat space after the conversion $8\pi G = \frac{1}{M_p^2}$ [19],

$$H^2 = \frac{1}{3M_p^2}\left(\frac{1}{2}\dot{\phi}^2 + V\right) \tag{2.75}$$

$$2H\dot{H} = \frac{1}{3M_p^2}\left(\dot{\phi}\ddot{\phi} + V'\dot{\phi}\right). \tag{2.76}$$

The equation of motion (2.36) during slow roll inflation when $\ddot{\phi} \rightarrow 0$ reduces to

$$\ddot{\phi} + 3H\dot{\phi} + V' = 0 \rightarrow V' = -3H\dot{\phi}, \tag{2.77}$$

and eq. (2.76) becomes

$$\dot{H} = -\frac{1}{2M_p^2}\dot{\phi}^2. \tag{2.78}$$

Under the slow-roll assumption that $V \gg \dot{\phi}$, eq. (2.75) gives us

$$H^2 = \frac{1}{3M_p^2}\left(\frac{1}{2}\dot{\phi}^2 + V\right) \approx \frac{1}{3M_p^2}V. \tag{2.79}$$

Substitution of eqs. (2.78) and (2.79) into the formula for ϵ yields

$$\epsilon = \frac{\dot{H}}{H^2} = -\frac{3}{2}\frac{\dot{\phi}^2}{V}. \tag{2.80}$$

By substituting eq. (2.79) into eq. (2.77), we find

$$\dot{\phi} = -\frac{V'}{3H} = -V'\left(\frac{M_p^2}{3V}\right)^{1/2}, \tag{2.81}$$

so that

$$\epsilon = -\frac{M_p^2}{2}\left(\frac{V'}{V}\right)^2. \tag{2.82}$$

We continue by using a definition of the second parameter in terms of the potential [42],

$$\eta = \frac{M_p^2 V''}{V}. \tag{2.83}$$

For the modes under consideration, that is, perturbations that crossed the approximately constant Hubble radius during inflation with $k = aH$,

$$\frac{d\log k}{dt} \approx \frac{d\log aH}{dt} \tag{2.84}$$

$$= \frac{\frac{d(aH)}{dt}}{aH} = \frac{\dot{a}}{a} = H \tag{2.85}$$

$$\rightarrow \; d\log k \approx Hdt. \tag{2.86}$$

In the equation for the scalar spectral index, eq. (2.73),

$$n_s - 1 = \frac{d\log P_k}{d\log k}, \tag{2.87}$$

we convert the epression for the denominator, eq. (2.86), into a function of the potential using eq. (2.77)

$$\frac{d}{d\log k} \approx \frac{d}{Hdt} \tag{2.88}$$

$$V' = -3H\frac{d\phi}{dt} \;\rightarrow\; dt = -\frac{3H}{V'}d\phi \tag{2.89}$$

$$\frac{d}{Hdt} = \frac{1}{H}\frac{d}{\frac{-3H}{V'}d\phi} \;\rightarrow\; \frac{d}{d\log k} \approx -\frac{V'}{3H^2}\frac{d}{d\phi}. \tag{2.90}$$

Substituting eq. (2.79) into the above gives

$$\frac{d}{d\log k} \approx -\frac{M_p^2 V'}{V}\frac{d}{d\phi}. \tag{2.91}$$

The spectral index becomes

$$n_s - 1 = \frac{d\log P_k}{d\log k} = -\frac{M_p^2 V'}{V}\frac{d}{d\phi}\left[\log\left(\frac{1}{75\pi^2 M_p^2}\frac{V^3}{V'^2}\right)\right] \tag{2.92}$$

$$= -\frac{M_p^2 V'}{V}\frac{d}{d\phi}\left[\log\left(\frac{V^3}{V'^2}\right)\right] \tag{2.93}$$

$$= -6\frac{M_p^2}{2}\left(\frac{V'}{V}\right)^2 + 2M_p^2\frac{V''}{V} \tag{2.94}$$

$$= -6\epsilon + 2\eta. \tag{2.95}$$

This is the form of the spectral index that, for example, the Planck Collaboration reports in an early paper on inflationary constraints [43]. Thus, under the slow roll constraints $\epsilon \ll 1$ and $\eta \ll 1$, slow roll inflationary theory predicts a spectral index approximately equal to 1.

The enhanced resolutions from COBE to WMAP to the Planck mission show increasingly convincing observational evidence in support of inflationary theory. COBE calculates a scalar spectral index of $n_s = 1.2 \pm 0.3$ [35], a somewhat flat result. The refined scale of WMAP provides stronger support for slow roll theory with a much flatter spectral index measurement, $n_s = 0.9608 \pm 0.0080$ [41]. The additional precision of the Planck telescope serves to reinforce the WMAP finding with $n_s = 0.9649 \pm 0.0042$ [38], suggesting that numerically, we are approaching a valid measurement of the actual phenomenon. In addition, the Planck Collaboration explicitly confirms the Gaussian nature of the inflaton and affirms the validity of both the slow roll approach and the power law spectrum [38].

Polarization of the CMB

Additional constraints on models of inflation are available through comparison of observation of CMB polarization and theoretical predictions. The CMB exhibits polarization that is in essence different from the familiar polarization of electromagnetism. Light, with its oscillating electric and magnetic fields, can exhibit linear and circular polarization. In a somewhat analogous manner, the CMB has regions of oscillations made up of components termed *E-modes* and *B-modes*. The E-mode polarization is like electromagnetic linear polarization in that it is perpendicular to the axial wave vector, although the E-mode polarization can also be parallel to the wave vector axis. Both the electromagnetic linear polarization and the CMB E-mode polarization lack a curl. While the circular polarization of electromagnetism is perpendicular to the wave vector, B-mode polarization lies at a 45° angle to the wave vector axis. Because the B-mode polarization can loop dependent on its orientation around a point in space, it is divergence-free like circular polarization. Again in analogy, like light waves possessing electromagnetic polarization, a wave of CMB radiation in a region of space displays polarization of its electric field consisting of superposed

E- and B-modes. The physics of the interaction of radiation and the geometry of space imparts the superposed modes on the last scattering surface.

To compare theoretical predictions with observations, that is, measures of the CMB polarization, cosmologists decompose curvature perturbations in the metric tensor into *scalar perturbations* and *tensor perturbations*, which are density perturbations and theoretically predicted gravitational waves, respectively. The formalism starts with the momentum space expression for a quantum scalar field $\chi(\mathbf{x}, t)$ [31, 44, 45],

$$\chi(\mathbf{x}, t) = \int \frac{d^3\mathbf{k}}{2\pi^{3/2}} e^{i\mathbf{k}\cdot\mathbf{x}} \chi_{\mathbf{k}}(t). \tag{2.96}$$

Cosmologists define the power spectrum in momentum space as the vacuum expectation value

$$\left\langle \chi_{\mathbf{k}_1} \chi^*_{\mathbf{k}_2} \right\rangle = \frac{2\pi^2}{k^3} P_{\chi_{\mathbf{k}}} \delta^{(3)} \left(\mathbf{k}_1 - \mathbf{k}_2\right), \tag{2.97}$$

and in real coordinate space, the definition is

$$\left\langle \chi^2_{\mathbf{k}}(t) \right\rangle = \int \frac{dk}{k} P_{\chi}(k). \tag{2.98}$$

After perturbation of the scalar field in conformal time τ, so that

$$\chi(\mathbf{x}, \tau) = \chi(\tau) + \delta\chi(\mathbf{x}, \tau). \tag{2.99}$$

second quantization with the commutation relations of the creation and annihilation operators yields the power spectrum of the fluctuations

$$P_{\delta\chi} = \frac{k^3}{2\pi^2} |\delta\chi|^2. \tag{2.100}$$

Scalar perturbations of the metric tensor are the density perturbations and related temperature anisotropies that result in the formation of large scale structure as described previously. In the formalism of the quantum scalar field, scalar perturbations have the power spectrum P_S and scalar spectral index n_S of eqs. (2.72) and (2.73).

Similarly, perturbing the metric tensor $g_{\mu\nu}$ of the RW metric,

$$ds^2 = g_{\mu\nu} dx^\mu dx^\nu, \tag{2.101}$$

generates the tensor perturbations and its power spectrum. Perturbations of the inflaton in the stress-energy tensor of the Einstein field equations give rise to metric tensor perturbations. Complex formalism fixing a gauge choice using constant conformal slices of time makes frame of reference transformations invariant and results in a revised metric tensor in terms of perturbation h_{ij},

$$g_{\mu\nu}dx^{\mu}dx^{\nu} = a^2(\tau)\left[-d\tau^2 + (\delta_{ij} + h_{ij})\,dx^i dx^j\right]. \tag{2.102}$$

The tensor δ_{ij} is the spatial part of the RW metric in conformal time. The tensor h_{ij} manifests itself physically as theoretically predicted gravitational waves.

Just like the scalar perturbations, scale-invariant tensor perturbations lie outside the Hubble radius after inflation, and we have an analogous tensor power spectrum P_T and spectral index n_T. The tensor-to-scalar ratio r, defined as

$$r = \frac{P_T}{P_S}, \tag{2.103}$$

is an observable parameter. Using suitable parametric estimates, cosmologists have derived model-dependent theoretical bounds on r. Thus, observations can lend support to or disfavor inflationary models.

Regarding the physics of polarization, the stage is set at recombination before the brief period of creation of the last scattering surface. The universe cools sufficiently to promote the formation of hydrogen atoms from ionized protons and free electrons. For the first time, photons are able to stream without continually being absorbed and emitted by electrons. However, electrons that have not yet bonded to protons scatter photons for the last time through Thomson scattering, which linearly polarizes the radiation [46]. The physics is not unlike that of the scattering of unpolarized light from a planar surface. An observer positioned along the line of sight of the incoming reflected light sees polarization aligned with the reflecting planar surface, that is, perpendicular to the plane formed by the incident and reflected rays. Thomson scattering from free electrons produces the same polarizing effect. If the incoming radiation is isotropic to the frame of reference of the electrons,

the superposed scattered radiation displays no polarization. However, in the case of the last scattering surface, the radiation incoming to the frame of the electrons has a preferred orientation, which the scattered radiation embodies in its polarization.

Spherical harmonic quadrupoles of temperature anisotropies arising from the $g_{\mu\nu}$ perturbations are responsible. The scalar and tensor perturbations of metric tensor perturbations create the quadrupoles of figure (2.6). Scalar perturbations, the consequence of underlying density perturbations of the metric tensor, generate E-mode polarization. The oscillations of gravitational waves, the tensor perturbations, create both E- and B-mode polarization.

Figure 2.6 Quadrupole images for spherical harmonics $Y_l^m(\theta, \phi)$ with indices $l = 2,\ m = 0$ on the left and $l = 2,\ m = 2$ on the right, associated with scalar and tensor perturbations, respectively. The light gray lobes are hotter, less dense regions in contrast to the colder, more dense, dark gray regions.

The temperature anisotropies and varying densities of photons in the $Y_2^0(\theta, \phi)$ quadrupole in the image on the left of figure (2.6) create radiation flows from both the upper and lower hotter lobes toward the colder torus-like region in the center. The rays incident to Thomson scattering are not isotropic, and the imbalance in the pattern of migration causes a net linear E-mode polarization. A more complicated dynamic takes place in the flow of radiation with the $Y_2^2(\theta, \phi)$ quadrupole in the image on the right and also with the $Y_2^{-2}(\theta, \phi)$ quadrupole. The peaks and troughs of passing gravitational waves laterally stretch the colder and hotter lobes, respectively, and impart both E- and B-modes of polarization to the radiation wave. Whereas the alignment in the Y_2^0 quadrupole of the lobes and the centrally-directed flows

results in Thomson scattering E-modes, the elongation of the lobes of the $Y_2^{\pm 2}$ quadrupoles by gravitational waves causes misalignment with the flows, so that scattering generates the looping B-mode. The three quadrupoles in combination imprint the superimposed modes on the suddenly free-streaming CMB photons comprising the last scattering surface.

Observations

Analysis of the CMB polarization begins with the decomposition of observations into the curl-free E-mode and divergence-free B-mode, similar to the decomposition of a vector into curl- and divergence-free components according to the Helmholtz Theorem, namely,

$$\mathbf{F} = \nabla\Phi + \nabla \times \mathbf{A}. \tag{2.104}$$

The formulas $\mathbf{E} = \nabla\Phi$ and $\mathbf{B} = \nabla \times \mathbf{A}$ in electrostatics would be the curl-free and divergence-free parts, respectively. The polarization of the CMB has position and orientation but lacks direction, in contrast to an electromagnetic wave, with its polarization vector pointing away from the axis of the wave vector. Decomposition of the CMB polarization involves a tensor composed of its Stokes parameters.

We have described the scalar perturbations giving rise to observable temperature anisotropies, by which the power spectrum becomes a function of the multipole moments of the correlation function. In the same way, we again observe polarization of the CMB as a pattern of temperature anisotropies. Produced by tensor perturbations of the metric tensor, these anisotropies are on a scale of an order of magnitude less than those of the scalar perturbations.

In the familiar formalism of electromagnetic polarization, decomposed wave components are

$$\mathbf{E}_x = E_x\, e^{i(\mathbf{k}\cdot\mathbf{x}-\omega t)}\, \hat{\mathbf{e}}_x = a_x\, e^{i\theta_x}\, e^{i(\mathbf{k}\cdot\mathbf{x}-\omega t)}\, \hat{\mathbf{e}}_x \tag{2.105}$$

$$\mathbf{E}_y = E_y\, e^{i(\mathbf{k}\cdot\mathbf{x}-\omega t)}\, \hat{\mathbf{e}}_y = a_y\, e^{i\theta_y}\, e^{i(\mathbf{k}\cdot\mathbf{x}-\omega t)}\, \hat{\mathbf{e}}_y, \tag{2.106}$$

with amplitudes written in terms of their magnitudes, a_x and a_y, and phase factors, θ_x and θ_y. We have time-averaged Stokes parameters [47]

$$I = \left\langle a_x^2 \right\rangle + \left\langle a_y^2 \right\rangle \tag{2.107}$$

$$Q = \left\langle a_x^2 \right\rangle - \left\langle a_y^2 \right\rangle \tag{2.108}$$

$$U = 2a_x a_y \cos(\theta_x - \theta_y). \tag{2.109}$$

The polarization in terms of position-defined parameters Q and U transforms invariantly under rotations with tensor

$$P_{ab} = \frac{1}{2}\begin{bmatrix} Q & -U\sin(\theta) \\ -U\sin(\theta) & -Q\sin^2(\theta) \end{bmatrix} \tag{2.110}$$

in coordinates $(\mathbf{n}, \theta, \phi)$. We recall the symmetry of the CMB offered expansion of the scalar perturbation temperature anisotropies in spherical harmonics in eq. (2.69). Although in a more complex form, spherical harmonic expansion of the CMB polarization is also available:

$$\frac{P_{ab}}{T_0} = \sum_{l=2}^{\infty} \sum_{m=-l}^{l} \left[a^G_{(lm)} Y^G_{(lm)ab} + a^C_{(lm)} Y^C_{(lm)ab} \right]. \tag{2.111}$$

The supercripts G and C signify the gradient and curl decompositions for E- and B-modes like the decompositions of the vector in eq. (2.104). Figure 2.7 contains depictions of a set of idealized orientations of the polarization of the E-modes and B-modes less than and greater than zero.

Beginning with observations taken in 2006, the BICEP collaboration has reported on measurements of the CMB polarization at increasing sensitivities. Three years of observations from 2010 to 2012 at the South Pole resulted in the E-mode and B-mode maps of figure 2.8.

The instruments viewed $\sim$ 380 square degrees of the southern hemisphere sky around right ascension 0° and declination −57.5°. Right ascension 0° is the celestial equivalent of the Prime Meridian. Cosmologists call it the *Vernal equinox*, the longitude in the sky

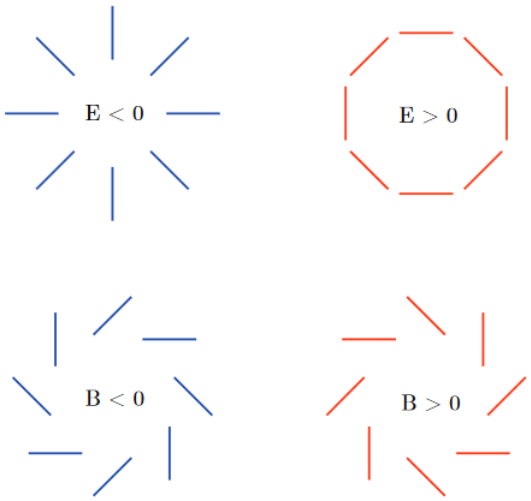

Figure 2.7 A sample of possible orientations of curl-free E-mode and divergence-free B-mode CMB polarizations. Figure from Ref. [45].

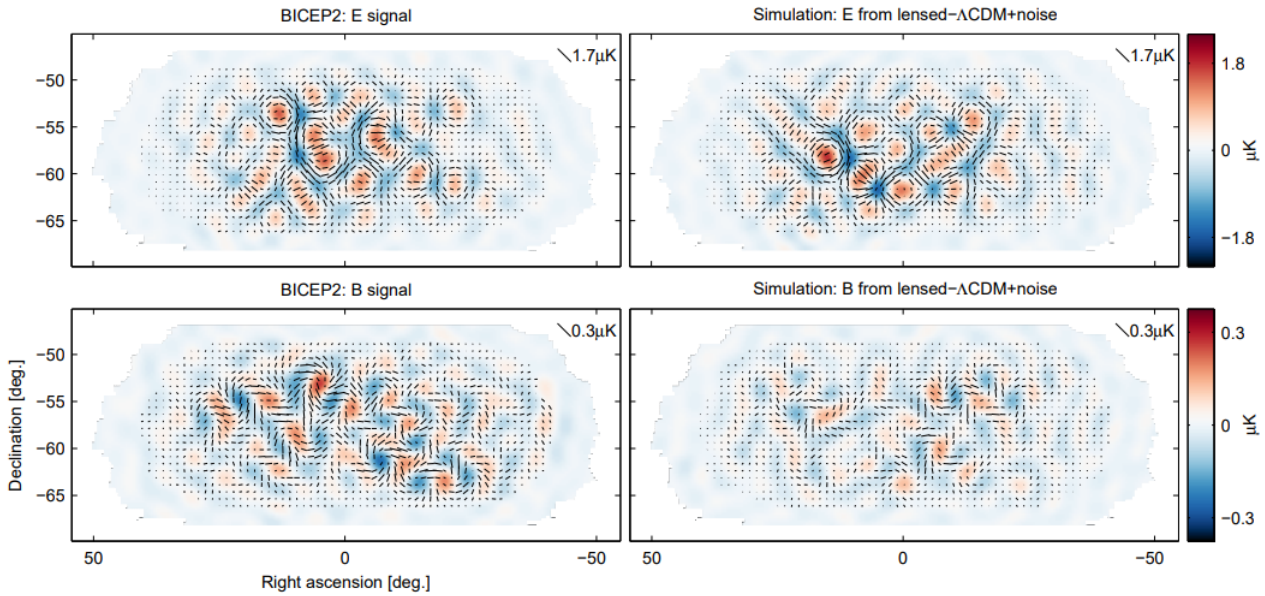

Figure 2.8 Observed and simulated E- and B-mode maps on the left and right, respectively. Figure from Ref. [48].

where the sun crosses the celestial equator on the spring equinox. Declination is the celestial equivalent of latitude. In figure 2.8, color-coded temperature anisotropies appear measuring $\lesssim \pm 1.8\mu$K in the top row maps and $\lesssim \pm 0.3\mu$K in the bottom row maps. The line segments represent polarization orientations corresponding to magnitudes of temperature anisotropies at scales of 1.7μK and 0.3μK for the E-modes and B-modes, respectively. The

pair of graphs on the left are observations after undergoing filtering processes. On the right are simulations of maps based on a lensed-ΛCDM+noise environment. The simulations include both instrument noise and the post recombination lensing effect of conversion of E-modes into B-modes by the CMB passing through the influence of the gravitational potential of structure. Statistical analysis offers a comparison for consistency between the actual observations and the simulations. At this point in the project history, the collaboration has not yet cleaned their observational data of B-mode polarization to be reported by the Planck team caused by galactic dust.

Constraints on Models of Inflation

The Planck Collaboration reports consistency between the six parameters used to characterize the ΛCDM universe and the fit of their model to observations. Table 2.1 details their bounds on the following six parameters:

- The present-day baryon density.
- The angular size of CMB fluctuations at recombination, which is the ratio of the acoustic sound wave arc length on the last scattering surface to the observational distance.
- The Thompson scattering optical depth, a measure of the number of times a photon is scattered. As described above, isotropic Thomson scattering after reionization lessens the anisotropies originally imprinted at the time of the last scattering.
- The amplitude of the power spectrum of scalar perturbations.
- The scalar spectral index.
- The present-day density of dark and visible matter.

Table 2.1 The bounds of the Planck Collaboration on the six parameters of the ΛCDM universe [20].

Parameter	Result	Description
$\Omega_b h^2$	0.02237 ± 0.00015	Baryon density
$100\theta_{MC}$	1.04092 ± 0.00031	Angular size
τ	0.0544 ± 0.0073	Optical depth
$\log(10^{10} A_s)$	3.044 ± 0.014	Amplitude of scalar perturbations
n_s	0.9649 ± 0.0042	Scalar spectral index
Ω_m	0.3153 ± 0.0073	Matter density

A second publication of the Planck Collaboration reports their findings regarding the validity of models of inflation, graphically displayed in figure 2.9. The topmost colored items of the key accompanying the graph are the various sets of observational data used to analyze the models of inflation, including correlation functions (TT, TE, and EE); the removed E-mode data (lowE) and effect of structure (lensing); the Bicep results (BK15); and baryon acoustic oscillations (BAO). The lower set of colored items, dashed key, and colored bars represent the models of inflation considered. The graph bounds inflation models with the circles at the bottom of the key, that is, the span of values for inflationary e-folds, $50 < N < 60$. The figure displays the sets of observational data as upright, quasi-half-elliptical regions centered on the n_s-axis at 1-σ and 2-σ confidence levels. For example, close visual inspection reveals the outline in blue of a smaller, 1-σ area within the larger, 2-σ blue area.

Based on their derived bound for the tensor-to-scalar ratio, $r_{0.002} < 0.056$, the Planck team reaches a conclusion supporting slow-roll, concave potentials and no other. The subscript 0.002 defines the scale of the horizon-crossing mode $\mathbf{k}$ during inflation as $\mathbf{k} = 0.002\,\mathrm{Mpc}^{-1}$. For the models of inflation of interest here, quadratic slow roll and chaotic inflation, we see the ϕ^2 potential model becoming progressively more removed in time from the colored areas of the Planck analyses in the graphs of the 2013, 2015, and finally 2018 papers [38, 43, 49]. The latest paper shows the ϕ^2 model in figure 2.9 lying entirely outside the valid colored areas. However, we can consider the final physics far from settled.

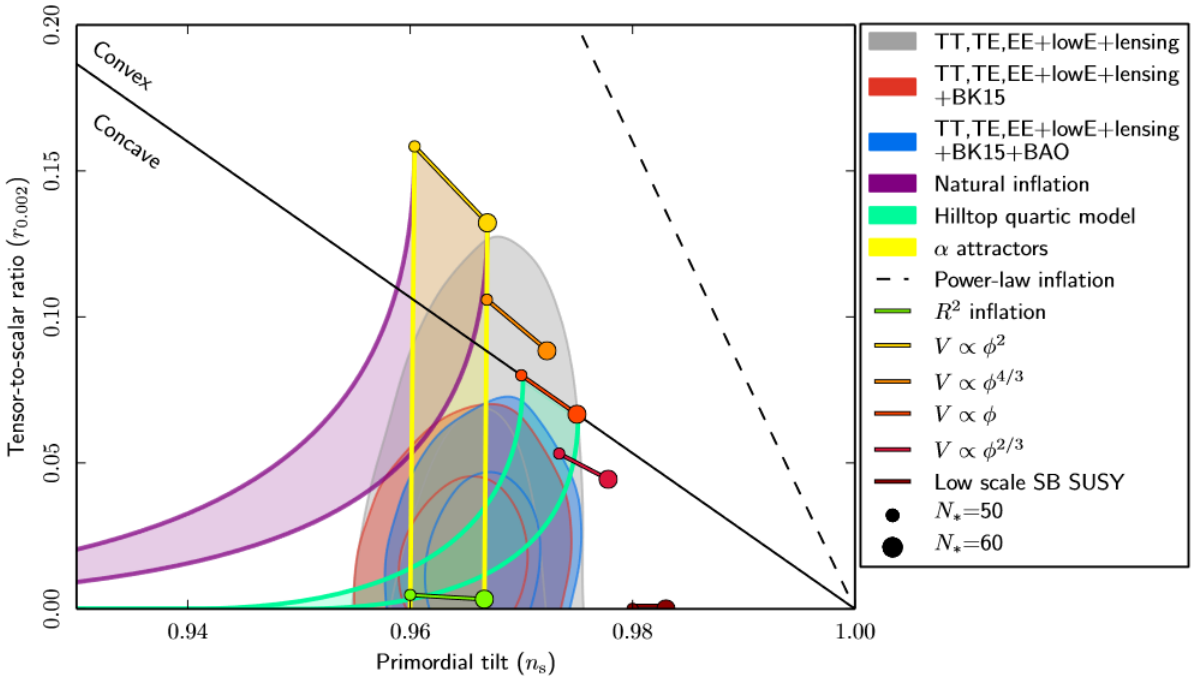

Figure 2.9 The graphical result of the Planck analyses of inflationary models. Figure from Ref. [38].

2.5 Reheating

The expansion of space by inflation dilutes the number densities of all particles and leaves the universe cold, with energy concentrated primarily in the inflaton. Following the end of inflation, reheating results in the transfer of energy from the inflaton to Standard Model particles or their precursors. Reheating has two stages, first the transfer of energy and then subsequent thermalization to a temperature sufficient to promote nucleosynthesis of light elements. A mechanism developed by Lev Kofman, Andrei Linde, and Alexei Starobinsky in their iconic 1997 paper, "Towards the Theory of Reheating after Inflation" [50], which they call *preheating* because it precedes thermalization, supersedes earlier explanations of reheating by way of perturbation theory and narrow parametric resonance. We reference a selection of the wide range of literature available on the subject of preheating [17, 51–54].

A preheating framework appears to be necessary, because perturbative processes prove too slow and inefficient to raise the reheating temperature enough to support nucleosyn-

thesis. Also, the perturbative approach required certain conditions and treated inflatons collectively in a state of superposition of individual particles, each capable of decaying independently—rather than as coherent semiclassical fields. On the other hand, narrow parametric resonance models followed the approach that the inflatons formed a homogeneous, coherent, oscillating wave appropriate for classical treatment. In narrow parametric resonance, an inflaton wave interacts as a background source for a second scalar field χ. However, this theory itself can be problematic. Because the modes of the scalar field χ have physical wavelengths, the expansion of space redshifts modes outside the borders of the resonance band and also makes the band more narrow. In addition, the expansion and the decay of the inflaton into χ particles decrease the amplitude of the coherent inflaton wave. The number of particles being produced instantaneously is proportional to both the number of χ particles previously created and to the inflaton amplitude, so that the effects of expansion and decay lower the efficiency of the resonant conversion and tend to suppress the growth of the χ population. Narrow parametric resonance thus typically terminates well before reheating is complete.

The parametric resonance in preheating models is instead broad: All modes less than a specific momentum participate in the ϕ-χ coupling. A non-adiabatic transfer of energy leads to exponential growth in the number and number density of the χ quanta. Moreover, the expansion of space can actually make the resonance more effective by gradually redshifting additional modes down to below the maximum momentum, making them part of the process. The end of reheating depends on the possible range of values of parameters involved in preheating and the complex dynamics of backreaction and rescattering. However, preheating may still not be sufficient to complete reheating, and the reheating process may have to revert to a period of narrow parametric resonance, perturbative decay, or both to arrive at a temperature that is suitable for thermalization but not high enough to produce very massive particles like monopoles.

In chapter 3, the reader will find a description of the cusp discontinuity inherent in inflationary theories involving an exponential scale factor and our approach to quantifying the extent of the cusp. Chapter 4 introduces a method for finding an interpolating function to replace the cusp, by detailing the geometry of a simple circular model, and then we focus on finding a more realistic interpolating function. We derive the formalism establishing smoothness in the expansion of space at the end of inflation and analyze the implications of the most straightforward interpolating candidates, power law functions. The equation-of-state and thermodynamic constraints provide additional means of restricting possible interpolating functions, and this is discussed in chapter 5. We analyze the effect on the size of the universe of a horizontal parabola-like power law serving as a transitional interpolating function in chapter 6. Finally, we look at further numerical analyses to determine the effect on the scalar χ number and number density predicted by the Kofman, Linde, and Starobinsky (KLS) model of preheating in chapter 7.

Chapter 3

Period Scale Factors

The well-known expressions for the scale factor in the early universe include a curious unphysical approximation, a lack of smoothness at the end of the inflationary epoch. The inflationary and radiation-dominated scale factors, $a_1(t)$ and $a_2(t)$, respectively, follow [11]

$$a_1(t) = a(t_i)e^{H(t-t_i)} \tag{3.1}$$

$$a_2(t) = a(t_f)\left(\frac{t}{t_f}\right)^{1/2}. \tag{3.2}$$

To demonstrate the discontinuity in $\dot{a}$, we assume contrariwise that the time derivatives of the scale factors are equal at the end of inflation, t_f:

$$\frac{d}{dt}a_1(t)\Big|_{t_f} = a(t_i)He^{H(t-t_i)}\Big|_{t_f} = a(t_f)H \tag{3.3}$$

$$\frac{d}{dt}a_2(t)\Big|_{t_f} = \frac{a(t_f)}{\sqrt{t_f}}\frac{1}{2t^{1/2}}\Big|_{t_f} = \frac{a(t_f)}{2t_f}. \tag{3.4}$$

By first expressing the Hubble parameter H in terms of N, the number of inflationary e-folds of expansion, and then equating derivatives, we find

$$H = \frac{N}{t_f - t_i} \tag{3.5}$$

$$N = \frac{t_f - t_i}{2t_f} = \frac{1}{2} - \frac{t_i}{2t_f}. \tag{3.6}$$

Continuity of the derivatives requires that $N \leq \frac{1}{2}$, or else the time at the beginning of inflation is less than zero. Although much research into inflation has produced a wide range of proposed values for N, this result is particularly problematic. If taken literally, it would eliminate inflation as a solution to the kinds of problems the theory was designed to solve.

Although early universe estimates are themselves quite problematic because of the uncertainty in the values of basic parameters, using reasonable values can provide some insight into the mathematical relationship between the scale factors in different periods of cosmological evolution. We can estimate a value for $a(t_f)$ by taking advantage of the inverse relation between the scale factor and temperature, in conjunction with estimates of temperature then and now, $T(t_f)$ and $T(t_0)$, respectively,

$$a(t_f) = \frac{T(t_0)}{T(t_f)} \approx \frac{2.73\,\mathrm{K}}{1.16 \times 10^{29}\,\mathrm{K}} \approx 10^{-29}, \tag{3.7}$$

since by convention, $a(t_0) = 1$. The temperature of the CMB today is $T(t_0) \approx 2.73$ K [21], and $T(t_f)$ corresponds to the temperature equivalent to the value of H for a universe that supports the Standard Model, which is $H \approx 10^{16}$ GeV [55].

Next we compare slopes at the end of inflation. The inflationary slope is

$$\dot{a}_1(t_f) \approx 10^{-13}\,\mathrm{GeV} \approx 10^{11}\,\mathrm{s}^{-1}. \tag{3.8}$$

For the radiation-era derivative, after solving eq. (3.5) for t_f and substituting it into eq. (3.4), we have

$$\dot{a}_2(t_f) = \frac{a(t_f)H}{2(N + Ht_i)} = \frac{\dot{a}_1(t_f)}{2(N + Ht_i)}. \tag{3.9}$$

The estimate by Liddle and Lyth that inflation began at $t_i = 10^{-42}$ s [12] leads to $Ht_i \approx 0.02$. A reasonable assumption is that $N \approx 60$ [29–31], which results in a measure of the discontinuity. The time derivative of the radiation-era scale factor is approximately $\frac{1}{120}$ of the derivative of the inflationary scale factor. Graph (a) of figure 3.1 shows this change in the growth behavior qualitatively. We also note that these values, $H = 10^{16}$ GeV and $N = 60$, yield an estimate for the duration of inflation without the need to specify t_i or t_f:

$$\Delta t = \frac{N}{H} \approx 4 \times 10^{-39}\,\mathrm{s}. \tag{3.10}$$

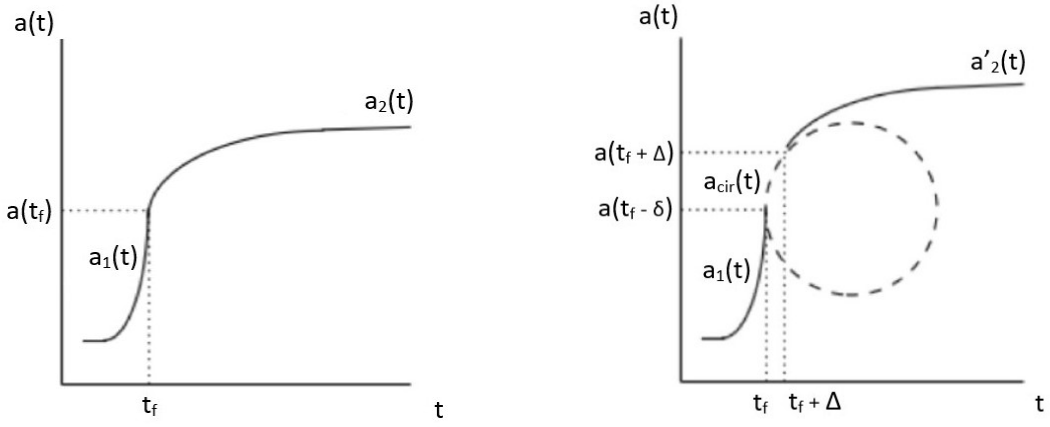

(a) (b)

Figure 3.1 (a) The graph depicts the discontinuity between inflationary and radiation era scale factors at the end of inflation. (b) The circular arc defined by the transitional scale factor $a_{\rm cir}(t)$ intersects tangentially with the inflationary scale factor $a_1(t)$ and the now-displaced radiation era scale factor noted with a prime, $a_2'(t)$.

Chapter 4

The Transition

What kind of transitional function could provide continuity between the two period scale factors? At the end of inflation, the slope begins to decline. For simplicity, we require a steadily declining slope with no regions in which the universe undergoes contraction. To preserve the accepted forms of the period scale factors, we seek a continuous piecewise function. A properly chosen intermediate power law would conform to our requirement, which we explore below. We know of no other solution, complete or otherwise, offered in the literature. Initially, as shown in graph (b) of figure 3.1, we shall use a circular arc $a_{\text{cir}}(t)$ to illustrate the geometry. The arc lies tangent to $a_1(t)$ at the end of inflation and tangent to the now-displaced radiation-era scale factor noted with a prime, $a_2'(t)$. The a functions are not to scale. The parameter Δ to be determined is the time period from the end of inflation until the time of continuity between $a_{\text{cir}}(t)$ and $a_2'(t)$.

In the more detailed view of figure 4.1, we see five unknown variables:

- R — the radius of the circular arc
- Δ — the time between t_f and the tangent point at which the circular arc $a_{\text{cir}}(t)$ meets the displaced radiation era $a_2'(t)$
- $a(t_f - \delta)$ — the a-axis value at $t_f - \delta$, aligned with the center of the arc
- δ — the measure of the t-axis displacement corresponding to the difference between $a(t_f)$ and $a(t_f - \delta)$
- $a(t_f + \Delta)$ — the scale factor at $t_f + \Delta$, the t-axis point of tangency for $a_{cir}(t)$ and $a_2'(t)$.

The transitional function is just the equation of the circle

$$a_{\text{cir}}(t) = a(t_f - \delta) + \sqrt{R^2 - [t - (R + t_f - \delta)]^2}. \tag{4.1}$$

If $a(t_f)$ and $a(t_f - \delta)$ were to coincide, we would be introducing another discontinuity into the model, the change from the inflationary slope to the infinite slope of the circular arc. With the displacement δ, the edge of the circular arc lies earlier on the timeline than t_f, and δ sets that duration. We note that $a(t_f - \delta)$ is therefore never the physical value of the scale factor and so has no direct effect on the expansion of space.

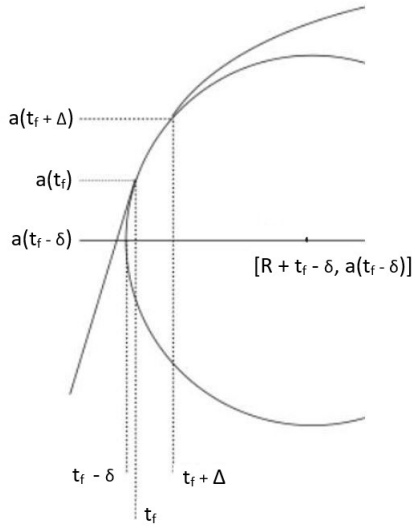

Figure 4.1 Five unknown parameters characterize the two points of tangency of $a_{\text{cir}}(t)$ with the period scale factors (not to scale).

We establish smoothness by equating the scale factors and their derivatives at the tangent points. Thus, we have five unknown parameters in the four matching conditions. In section 5.3, we invoke a fifth equation to specify the model completely.

Imposing a circular arc is an unreasonably strict condition to use to define an interpolating function. We shall continue now by exploring more general power-law solutions for $a(t)$ in the transition between the period scale factors. A properly chosen power-law section would provide continuity but would also potentially lengthen one or the other period, depending on its orientation. A power law with $n < 1$ has essentially no impact on

the length of the radiation era. For a power law with $n > 1$, a very small increase in the inflationary period could have a substantial impact on the scale factor, as discussed further in section 4.2.

4.1 Interpolating Power Laws with $n < 1$

The power law takes the form

$$a_p(t) = a_p(t_f - \delta) + D\,[t - (t_f - \delta)]^n. \tag{4.2}$$

We use the notation $a_p(t)$ for power laws with $n < 1$. The subscript p denotes the representative parabola for $n = \frac{1}{2}$, which opens to the right and has a horizontal axis. The unknown coefficient D is the analog of the unknown radius of the circular arc. Additional unknown parameters, $a_p(t_f - \delta)$, δ, Δ, and $a(t_f + \Delta)$, correspond to the parameters displayed in figure 4.1 for the circular arc. We analyze the continuity of the forms of the scale factor at the two points of tangency.

4.1.1 Smoothness at t_f

For the first matching condition—continuity of $a(t)$—at t_f, $a_p(t)\big|_{t_f} = a(t_f)$ implies

$$D = \frac{a(t_f) - a_p(t_f - \delta)}{\delta^n} \tag{4.3}$$

$$a_p(t) = a_p(t_f - \delta) + \frac{a(t_f) - a_p(t_f - \delta)}{\delta^n}\,[t - (t_f - \delta)]^n. \tag{4.4}$$

The second matching condition at t_f equates the time derivatives, generating an expression for the a-axis vertex coordinate:

$$\dot{a}_p(t)\big|_{t_f} = \dot{a}_1(t)\big|_{t_f} = T(t_0) \tag{4.5}$$

$$\dot{a}_p(t)\big|_{t_f} = n\left[\frac{a(t_f) - a(t_f) - \delta}{\delta^n}\right]\delta^{n-1} \tag{4.6}$$

$$a_p(t_f - \delta) = a(t_f) - \frac{T(t_0)\delta}{n}, \tag{4.7}$$

where we have used the relations in eqs. (3.3) and (3.7) to express these in terms of the current temperature $T(t_0)$, since $t = t_0$ also provides the calibration scale for a. With the vertex coordinate from eq. (4.7), the scale factor is

$$a_p(t) = a(t_f) - \frac{T(t_0)\delta}{n} + \frac{T(t_0)}{n\delta^{n-1}}\left[t - (t_f - \delta)\right]^n. \tag{4.8}$$

4.1.2 Smoothness at $t_f + \Delta$

The interpolating transition we have imposed between the end of inflation and the beginning of the radiation era shifts the eq. (3.2) scale factor according to

$$a_2'(t) = a(t_f + \Delta)\sqrt{\frac{t}{t_f + \Delta}}, \tag{4.9}$$

where we use the prime to distinguish this shifted expression. The vertex of the radiation-era $t^{1/2}$ scale factor remains at $(t = 0, a = 0)$. The third matching condition, in which the interpolating power-law equals $a_2'(t)$ at the point of tangency, yields the noninformative solution

$$a_2'(t)\Big|_{t_f+\Delta} = a_p(t_f + \Delta). \tag{4.10}$$

However, the final smoothness condition equates the derivatives of the scale factors $a_2'(t)$ and $a_p(t)$ at $t_f + \Delta$, so we have

$$\dot{a}_p(t)\Big|_{t_f+\Delta} = \dot{a}_2'(t)\Big|_{t_f+\Delta} \tag{4.11}$$

$$\dot{a}_2'(t)\Big|_{t_f+\Delta} = \frac{a_p(t_f + \Delta)}{2(t_f + \Delta)} \tag{4.12}$$

$$\dot{a}_p(t)\Big|_{t_f+\Delta} = \frac{T(t_0)}{\delta^{n-1}}\left[t - (t_f - \delta)\right]^{n-1}\Big|_{t_f+\Delta} \tag{4.13}$$

$$= \frac{T(t_0)}{\delta^{n-1}}(\Delta + \delta)^{n-1}. \tag{4.14}$$

Thus we ultimately arrive at the condition,

$$\frac{T(t_0)}{\delta^{n-1}}(\Delta + \delta)^{n-1} = \frac{a_p(t_f + \Delta)}{2(t_f + \Delta)} \tag{4.15}$$

$$\frac{T(t_0)}{\delta^{n-1}}(\Delta + \delta)^{n-1} = \frac{1}{2(t_f + \Delta)}\left[a(t_f) - \frac{T(t_0)\delta}{n} + \frac{T(t_0)}{n\delta^{n-1}}(\Delta + \delta)^n\right]. \tag{4.16}$$

The formalism leaves us with the need to fix Δ to evaluate the model; Δ and $a(t_f + \Delta)$ are physical but as yet unknown parameters. The others are mathematical constructs with no direct physical meanings. After substituting the early universe parameter values assumed in section 3.1, we find, for example, the solution for $n = \frac{1}{2}$ at $\Delta = 10^{-35}$ s

$$\delta \approx 2.65 \times 10^{-6} \Delta \tag{4.17}$$

(evaluated using Maple). Table 4.1 lists additional values of δ for a sample set of transition durations Δ. The purpose of having three significant figures listed in the table is to illustrate the relationship between the displacement and any changes to the transition scale.

We have accomplished the objective of parameterizing the transition from the inflationary scale factor with a family of power-law scale factors that ensure sufficient smoothness to have continuity of a and its first time derivative—although we have not imposed the condition of continuity on any higher-order derivatives. The slope of the inflation-era scale factor grows at a rate on the order of the Hubble parameter, and a requirement of continuity on the second derivative would effectively extend inflation into the subsequent period, rather than marking the physical end of inflation as the point at which the second derivative becomes negative.

4.2 Power Laws with $n > 1$

To continue the study of alternative transitions, we now examine power laws with $n > 1$, containing unknown parameters analogous to those analyzed in the previous section. The scale factor formula is

$$a_v(t) = a_v(t_f + \delta) + E\,[t - (t_f + \delta)]^n. \tag{4.18}$$

The subscript v denotes the representative inverted parabola for $n = 2$ with the vertical axis parallel to the a-axis. The displacement of the vertex from $a(t_f)$ now places δ at a time later than the tangent point at $t_f + \Delta$, as shown in figure 4.2.

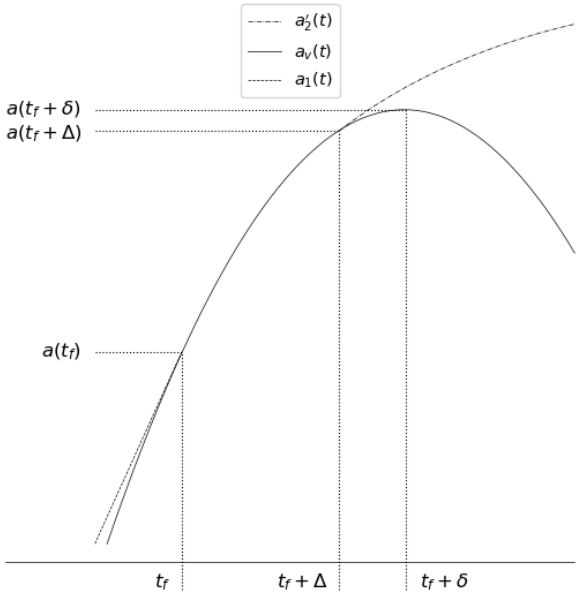

Figure 4.2 The displacement δ necessarily places the vertex of the representative inverted parabola with power law index $n = 2$ later than the end of inflation at t_f and the tangency point at $t_f + \Delta$ (not to scale). Increasing the duration over which the the interpolating scale factor applies also shifts the vertex similarly.

Repeating the analysis of the matching conditions at t_f and $t_f + \Delta$ yields the scale factor

$$a_v(t) = a(t_f) + \frac{T(t_0)\delta}{n} + \frac{T(t_0)}{n(-\delta)^{n-1}}[t - (t_f + \delta)]^n \tag{4.19}$$

and a fourth matching condition

$$\frac{T(t_0)}{(-\delta)^{n-1}}(\Delta - \delta)^{n-1} = \frac{1}{2(t_f + \Delta)}\left[a(t_f) + \frac{T(t_0)\delta}{n} + \frac{T(t_0)}{n(-\delta)^{n-1}}(\Delta - \delta)^n\right]. \tag{4.20}$$

Table 4.1 details the vertex displacements δ for power laws $a(t) \propto t^{1/2}$ and t^2 for a sample set of transition durations Δ between the end of inflation and the beginning of the radiation era. Increasing the duration Δ for the power law $n = \frac{1}{2}$ tends to set the displacement of the vertex. However, because of the difficulty of establishing continuity with the inflationary slope at t_f, the displacement δ for the $n = 2$ interpolator is many orders of magnitude greater. With its vertex located later on the timeline than t_f, the table shows that increasing

the transition has the effect of shifting the vertex of $a_v(t)$ farther away from the end of inflation. The vertex displacement δ for a power law with $n = 2$ and $\Delta = 10^{-35}$ s is almost six orders of magnitude farther from the point of tangency than that of the power law with $n = \frac{1}{2}$. The power law $a_p(t) \propto t^{1/2}$ can establish continuity with the slope of the inflationary scale factor with such a minute displacement, because the power law has an infinite slope at the vertex. However, the power law $a_v(t) \propto t^2$ has no such infinite slope, and the difficulty of establishing continuity with the large slope at the end of inflation, $\sim 10^{11}\ \mathrm{s}^{-1}$, manifests itself in the displacement being many orders of magnitude greater than that of $a_p(t) \propto t^{1/2}$.

Table 4.1 The vertex displacements δ for power laws $a(t) \propto t^{1/2}$ and t^2 for a sample set of transition durations.

Transition	n	Δ (s)	δ (s)
$a_p(t)$	$\frac{1}{2}$	10^{-35}	2.65×10^{-41}
		10^{-33}	3.22×10^{-41}
		10^{-30}	3.29×10^{-41}
		10^{-22}	3.29×10^{-41}
$a_v(t)$	2	10^{-35}	1.50×10^{-35}
		10^{-22}	1.50×10^{-22}

Figure 4.3 displays the transitional scale factors of eqs. (4.8) and (4.19), rescaled by a translation of the t-axis $t \to t' = t_f + t$. The timeline starts at the arbitrarily small initial value $t = 10^{-43}$ s. The graphs represent power laws for $n < 1$ and $n > 1$ with a representative sample of powers. The three $a_v(t)$ scale factors with power laws $t^{3/2}$, t^2, and $t^{5/2}$ essentially overlay each other, and the $a_p(t)$ scale factor proportional to $t^{1/4}$ approaches those of the power laws with $n > 1$. The graph also shows the unsmoothed scale factor defined by eq. (3.2), which exceeds that of $a_p(t)$ at $t^{3/4}$. The t-axis timeline begins at $t = 10^{-43}$ s after inflation terminates, while the vertical dotted line at $t = 10^{-35}$ s marks the nominal start of the radiation era. However, the graphs of the scale factors themselves offer somewhat limited insight into the evaluation of the quality of the interpolating functions. For that, we

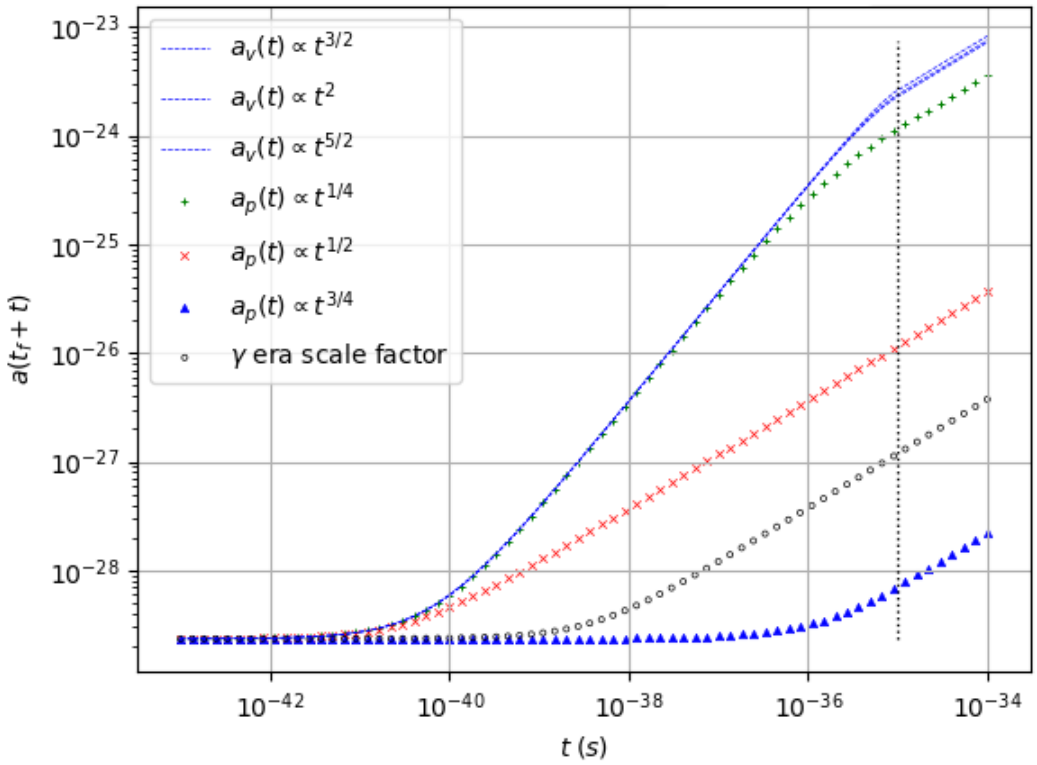

Figure 4.3 Scale factors $a(t_f + t)$ after inflation

now look instead to graphs of the Hubble parameter,

$$H(t_f + t) = \frac{\dot{a}(t_f + t)}{a(t_f + t)}. \tag{4.21}$$

In the transitional Hubble parameters below, H_{in} is the constant inflationary Hubble parameter, taken to be 10^{16} GeV. For the two classes of power laws, we find

$$H_p(t_f + t) = \frac{\left(1 + \frac{t}{\delta}\right)^{n-1}}{\frac{1}{H_{\text{in}}} - \frac{\delta}{n} + \frac{\delta}{n}\left(1 + \frac{t}{\delta}\right)^n} \tag{4.22}$$

$$H_v(t_f + t) = \frac{\left(1 - \frac{t}{\delta}\right)^{n-1}}{\frac{1}{H_{\text{in}}} + \frac{\delta}{n} - \frac{\delta}{n}\left(1 - \frac{t}{\delta}\right)^n}\,. \tag{4.23}$$

Figure 4.4 shows graphs of the Hubble parameters of eqs. (4.22) and (4.23) corresponding to the scale factors shown in figure 4.3. Once again, the graphs based on the scale factors $a_v(t)$ for $t^{3/2}$, t^2, and $t^{5/2}$ essentially overlay each other. The discontinuity of

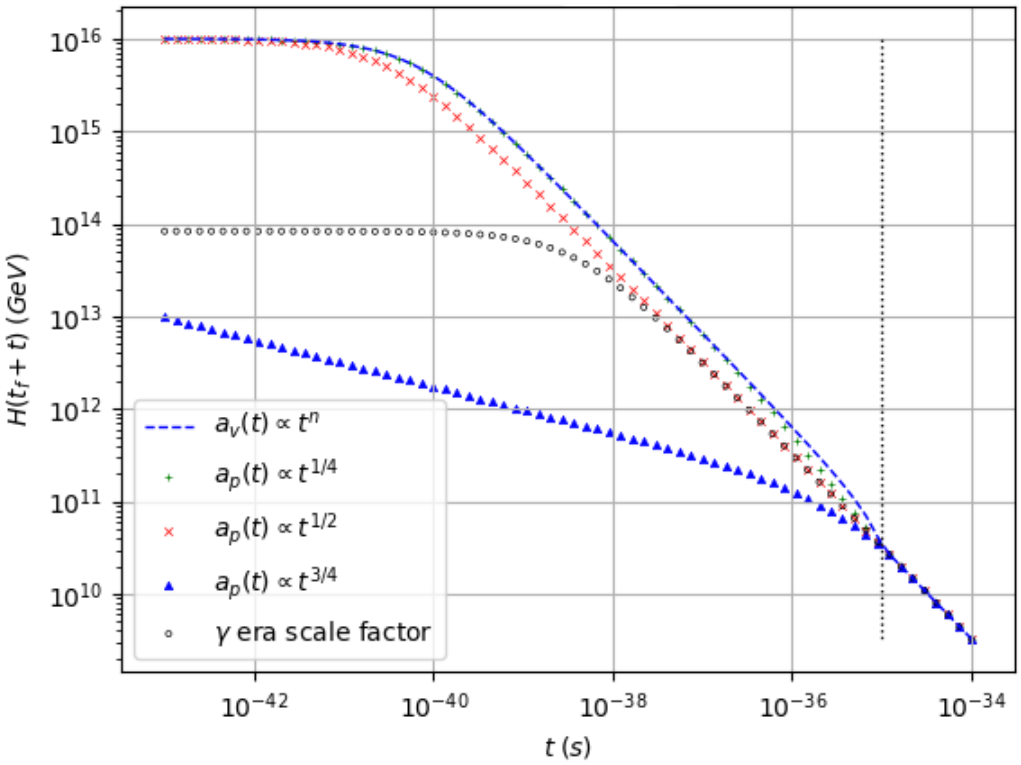

Figure 4.4 Hubble parameters $H(t_f + t)$ after inflation

the radiation-era Hubble parameter with H_{in} exceeds two orders of magnitude. The graph based on scale factor $a_p(t)$ for $t^{3/4}$ fails to display asymptotic behavior with H_{in} at small times, because the timeline has the same t-axis translation and does not start at t_f. Again the vertical dotted line marks the start of the radiation era at $t = 10^{-35}$ s. We note the requirement of smoothness at the beginning of the radiation era causes abrupt shifts downward and upward as $t \to \Delta$ for interpolating scale factors not proportional to $t^{1/2}$. The power laws with $n > 1$ that overlay each other in both figures 4.3 and 4.4 must exhibit the shift downward to establish continuity with the radiation era Hubble parameter. Unable to justify a physical basis for this behavior, we shall move forward in our analysis by eliminating these power laws as valid interpolating functions and focus on more specifically determining workable interpolating functions with $n < 1$. We also note that as $n \to \frac{1}{2}$ from above or below, the scale factor $a_p(t)$ transforms more seamlessly into the radiation era. So

at this stage, we expect that the most suitable interpolating functions will correspond to the index value $n = \frac{1}{2}$, or something close to that. The power laws for the interpolating region and the subsequent radiation-dominated era are both horizontally-opening parabolas (or nearly so), which differ principally in their vertex placements and radii of curvature.

Chapter 5

Additional Constraints

5.1 The Equation of State

We continue with the evaluation of the usefulness of the possible interpolations by considering a parameter ϵ_H, which is an alternative to the equation-of-state parameter w that satisfies $p = w\rho$, according to

$$\epsilon_H = \frac{d\log(H^{-1})}{d\log a} = \frac{3}{2}(1 + w). \tag{5.1}$$

Following a graphical technique described by Kaloian Lozanov [54], we shall interpret the formula as the slope in a plot of the evolution of the scale factor from inflation to the radiation-dominated era. Appendix D provides more information about this expression. Figure 5.1 shows our version of the Lozanov graphical approach for the power law $a_p(t) \propto t^n$, with n ranging from 0.05 to 0.95. Table 5.1 lists statistics for some of the graphed power laws, as well as smaller and larger values of n.

Aside from the footnoted observations in Table 5.1, we note a further curious feature of figure 5.1. The graphs at the upper and lower extremes of n display almost cusp-like changes of slope between the transition and the radiation-dominated era at $t = t_f + \Delta$. Between inflation and the start of the radiation-dominated era, ϵ_H changes from a value much greater than 2 to less than 2 for $n > \frac{1}{2}$. Conversely, for $n < \frac{1}{2}$, the parameter starts less than 2 and then becomes greater than 2. With our expectation that $\epsilon_H = 2$, only the power law $n = \frac{1}{2}$ (the same power law index as in the radiation era itself) appears able to transition seamlessly to the radiation era, which suggests that all powers except $n = \frac{1}{2}$ result in a cusp in the evolution of ϵ_H. This motivates a closer inspection.

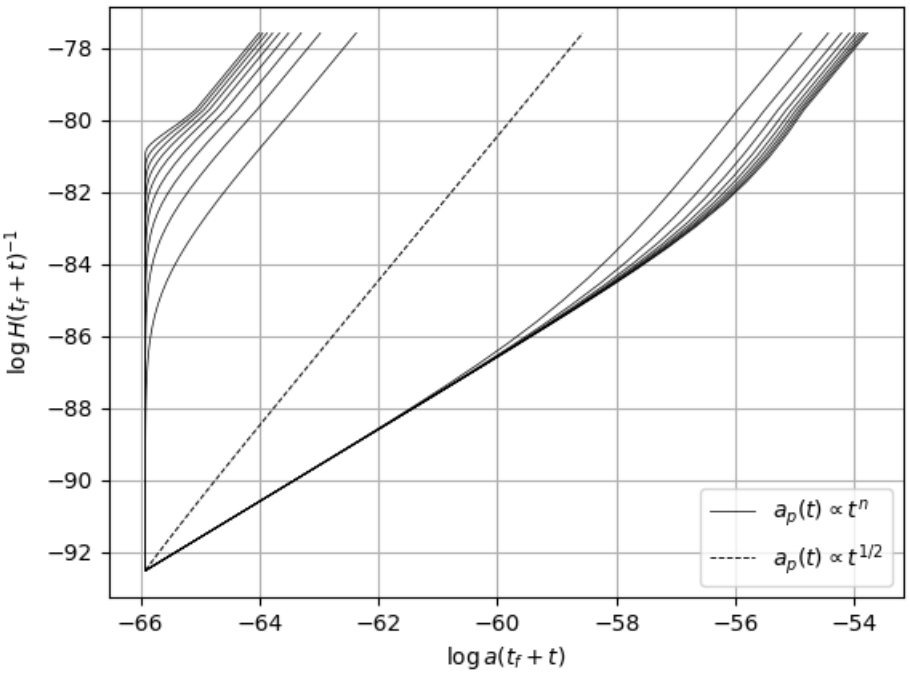

Figure 5.1 Graphs of $\log H^{-1}$ by $\log a$ with 0.05 increments in n from 0.05 to 0.95. The slopes of the graphs equal the parameter $\epsilon_H = \frac{d \log(H^{-1})}{d \log a}$.

Table 5.1 The displacement δ, parameter ϵ_H, and equation-of-state parameter $w = \frac{2}{3}\epsilon_H - 1$ for power laws $a_p(t) \propto t^n$, with values of n ranging between 0 and 1.

n	δ (s)	ϵ_H	w
0.002	2.53×10^{-36}	2.59	0.73 [b]
0.25	9.55×10^{-37}	2.37	0.58
0.50	2.65×10^{-41}	2.00 [a]	0.33
0.75	9.46×10^{-56}	1.50	0.00 [c]
0.98	2.31×10^{-294}	1.04	−0.31 [d]

(a) Computation sets this value more precisely at ≈ 2.00039. After interpolation using the linear relation associated with eq. (5.2), the expected $\epsilon_H = 2$ for a radiation-dominated scale factor occurs at $n \approx 0.5002$.
(b) Values of $\epsilon_H \to 2.6^-$ and $w \approx 0.73$ signify unphysical, exotic tachyon-like particles with velocities greater than the speed of light, which section 5.2 discusses in detail.
(c) For $\epsilon_H \approx 1.50$ and $w \approx 0.00$, we have a transition from inflation to an equation of state that would be consistent with a matter-dominated universe. We take up consideration of the single-component matter-dominated universe in section 5.3.
(d) As $\epsilon_H \to 1.0^+$ and $w \to -\frac{1}{3}$, the scale factor remains inflationary, effectively eliminating the transition.

Figure 5.2 plots ϵ_H versus the power law index n at time $(t_f + \Delta)$:

$$\epsilon_H = 1 + (1-n)\frac{a(t_f) - \frac{T(t_0)\delta}{n} + \frac{T(t_0)\delta}{n}\left(1+\frac{\Delta}{\delta}\right)^n}{T(t_0)\delta\left(1+\frac{\Delta}{\delta}\right)^n}. \tag{5.2}$$

For $n > \frac{1}{2}$, the negative term in the numerator of eq. (5.2) is small relative to the other terms appearing in the fraction, which are on the order of $a(t_f)$ and essentially cancel with the factor of the same characteristic size in the denominator. The linear relation $\epsilon_H - 1 \propto (1-n)$ remains, as the graph and Table 5.1 show. In contrast, for $n < \frac{1}{2}$, the scale factor $a(t_f)$ is small relative to the other terms in the fraction. As $n \to 0$, the fraction and $(1-n)$ are both increasing, and ϵ_H increases to approximately 2.6.

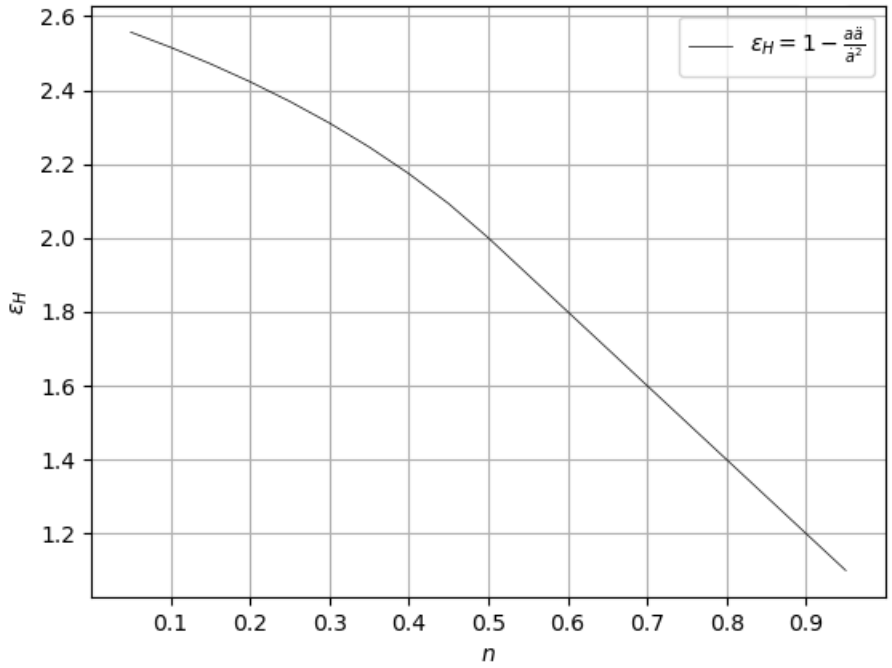

Figure 5.2 The parameter $\epsilon_H = -\frac{\dot{H}}{H^2}$ with power law $a_p(t) \propto t^n$ for $n < 1$ in 0.05 increments at the start of the radiation era, with the transition period $\Delta = 10^{-35}$ s.

Figure 5.2 aligns with the possibility raised by figure 4.3 that only $n = \frac{1}{2}$ results in a transition to the radiation era without an awkward, cusp-like feature—whose very presence would seem to be contrary to the dictum we have adopted of modeling the transitions in a smooth fashion. However, precise calculations consistently indicate that a slightly different

$n \approx 0.5002$ actually produces the seamless transition. In the same way as the abrupt shift that we cannot explain in the graph of the Hubble parameters tends to disqualify all power laws except $n = \frac{1}{2}$, the cusp-like features again appear likely to signify unphysical, unexplained behavior. However, before we attempt to resolve these conflicts, we shall review additional constraints on the equation of state, starting with constraints related to the speed of sound.

5.2 Speed of Sound Constraints

Another tool for evaluating the interpolators is the application of constraints on the speed of sound to the equation of state. A speed of sound less than zero or greater than the speed of light would violate stability or causality, respectively [56, 57]. Stability requires that the speed must be real; imaginary phase speeds would correspond to imaginary frequencies, or modes that grow exponentially with time. At the other end, special relativity imposes the standard limitation that information carried by arbitrary quanta cannot propagate faster than the speed of light $c = 1$ in vacuum. Thus, we expect the sound speed of the transition waves to obey inequalities

$$0 \leq v_s^2 \leq 1. \tag{5.3}$$

We assume, as is standard, that the inflaton wave oscillations are fast and thus adiabatic, so that a passing wave brings about temperature changes without conductive heat transfer. The thermodynamic behavior is reversible, and so the entropy per unit mass is constant [58] as an inflaton wave passes through. Pressure $p = p(s, \rho)$ becomes a function of the density ρ only, $p = p(\rho)$. We also make the assumption that the inflaton condensate at the end of inflation is a perfect fluid, allowing us to apply a linear, single-component equation of state, $p = w\rho$, expressing the dependence of pressure on density in terms of a ρ-independent equation-of-state parameter w. This environment yields a sound speed

$$v_s^2 = \frac{1}{d\rho/dp} = \frac{dp}{d\rho} = w, \tag{5.4}$$

and using $w = \frac{2}{3}\epsilon_H - 1$, the condition $0 \leq w \leq 1$ implies $\frac{3}{2} \leq \epsilon_H \leq 3$. At the precise end of inflation, $\Delta = 0$ in eq. (5.2), leaving

$$\epsilon_H = 1 + (1-n)\frac{a(t_f)}{T(t_0)\delta} = 1 + \frac{(1-n)}{H\delta}. \tag{5.5}$$

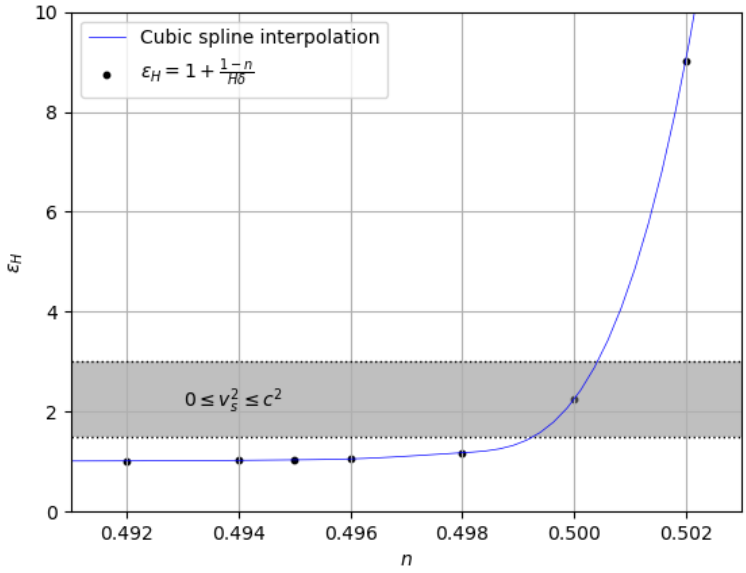

Figure 5.3 Values of the parameter $\epsilon_H = 1 + \frac{(1-n)}{H\delta}$ at the end of inflation, $t_f \approx 4 \times 10^{-39}$ s, for $a_p(t) \propto t^n$ with $n \approx \frac{1}{2}$ in increments of 0.001. The gray band depicts the permissible values of ϵ_H, $\frac{3}{2} \leq \epsilon_H \leq 3$, subject to the assumption that the inflaton condensate at the end of inflation is a single-component perfect fluid with equation of state $p = w\rho$.

Figure 5.3 displays the effect of enforcing the sound speed restrictions from eq. (5.3) on ϵ_H; these conditions severely restrict the permissible range of power laws indices. The line plot is a Python cubic spline interpolation of Maple-generated solutions for the parameter ϵ_H from eq. (5.2) in 0.001 increments around $n = \frac{1}{2}$. The section of the spline interpolation within the gray horizontal band contains valid values of ϵ_H, corresponding to interpolating theories with stable, causal sound speeds. Reading off the graph, we see the permissible physical power law band for the continuous function transitioning from the end of inflation to the radiation era lies approximately between $0.4990 < n < 0.5005$. This narrow band is consistent with the large separation in figure 5.1 between the power law $n = \frac{1}{2}$ and the closely adjacent powers, $n = 0.45$ and $n = 0.55$.

Although we have found restrictions on the allowed range of power law values, a tension between the expected and derived equations of state for $n = \frac{1}{2}$ actually remains. We do not find that $\epsilon_H = 2$ corresponds exactly to $n = \frac{1}{2}$. We instead recall the expected $\epsilon_H = 2$ was associated with $n \approx 0.5002$ reported in Table 5.1, and we now seek to understand the reason for the slight discrepancies between these values and the derived $\epsilon_H \approx 2.00039$ that corresponds to the exact $n = \frac{1}{2}$.

Comparison of the scale factor in eqs. (4.7) and (4.8) of section 4.1 with the first two terms in the numerator of the fraction in the expression below,

$$\epsilon_{H\,\text{derived}} = 1 + (1 - n)\frac{a(t_f) - \frac{T(t_0)\delta}{n} + \frac{T(t_0)\delta}{n}\left(1 + \frac{\Delta}{\delta}\right)^n}{T(t_0)\delta\left(1 + \frac{\Delta}{\delta}\right)^n}, \tag{5.6}$$

indicates that those two terms arise from the a-axis scale factor displacement $a_p(t_f - \delta)$ of the interpolating function's vertex. The third term in the numerator represents the functional dependence of the scale factor on time.

Table 5.2 details parameters corresponding to power laws $a_p(t)$ with indices $n = \frac{1}{2}$ and $n = \frac{2}{3}$ transitioning to radiation-dominated and matter-dominated eras with scale factors likewise proportional to $t^{1/2}$ and $t^{2/3}$. The column $\epsilon_{H\,\text{derived}}$ reconstructs the parameter as the sum of 1 and the contribution from the displacement and the time components. The difference between the expected and derived ϵ_H is separated into the relative contributions from the components of the numerator, $\epsilon_{H\,\text{displacement}}$ and $\epsilon_{H\,\text{time}}$. For comparison, we repeat the analysis for a single-component, matter-dominated transition function establishing continuity between the end of inflation and a matter-dominated era (that is, with $n = \frac{2}{3}$ power laws). We see the results are qualitatively the same. The displacement of the vertex of the scale factor along the a-axis is responsible for the discrepancies from $\epsilon_{H\,\text{expected}}$.

Table 5.2 Parameters corresponding to power laws $a_p(t)$ with indices $n = \frac{1}{2}$ and $n = \frac{2}{3}$ transitioning to radiation-dominated and matter-dominated eras.

n	δ (s)	ϵ_H expected	ϵ_H derived	ϵ_H displacement	ϵ_H time
$\frac{1}{2}$	2.65×10^{-41}	2	2.00039	0.00039	1.00000
$\frac{2}{3}$	7.71×10^{-42}	1.5	1.50020	0.00020	0.50000

If not for the contribution of the vertex displacement, we would have seamless transitions of the equation of state between the interpolating power laws and the radiation or matter eras. A first-order phase transition at $(t_f + \Delta)$ might be responsible for the cusp, but we reason against that possibility. The dynamics of the expansion of space at the tangent point undergoes no change. Prior to and after $(t_f + \Delta)$, the power law index n governing expansion remains approximately the same for each single-component era. Also, the transition precedes the period of preheating described in chapter 7 and subsequent thermalization, so that we expect temperature to evolve smoothly at $t_f + \Delta$.

Instead, invoking continuity of the equation of state at $(t_f + \Delta)$ and noting $\epsilon_{H\,\text{expected}} = \frac{1}{n}$ for a single-component universe, as appendix E shows, we solve eq. (5.6) for the displacement δ and find

$$\epsilon_{Hexpected} = \frac{1}{n} = 1 + (1 - n)\frac{a(t_f) - \frac{T(t_0)\delta}{n} + \frac{T(t_0)\delta}{n}\left(1 + \frac{\Delta}{\delta}\right)^n}{T(t_0)\delta\left(1 + \frac{\Delta}{\delta}\right)^n} \tag{5.7}$$

$$\frac{1}{n} = \frac{a(t_f) - \frac{T(t_0)\delta}{n} + \frac{T(t_0)\delta}{n}\left(1 + \frac{\Delta}{\delta}\right)^n}{T(t_0)\delta\left(1 + \frac{\Delta}{\delta}\right)^n}. \tag{5.8}$$

Substituting $a(t_f) = T(t_0)/H$ from eq. (3.7) with $H = H_{\text{in}}$ yields

$$\delta = \frac{n}{H}. \tag{5.9}$$

Analysis of eq. (5.6) demonstrated that the displacement

$$\epsilon_{H\,\text{displacement}} = a(t_f) - \frac{T(t_0)\delta}{n} \tag{5.10}$$

caused the cusp-like feature. With the eq. (5.9) result, and recalling $a(t_f) = \frac{T(t_0)}{H}$, we instead have $\epsilon_{H\,\text{displacement}} = 0$, and the bump on the curve is gone.

However, making the assumption of continuity of the equation of state at $t_f + \Delta$ destroys the smoothness of the scale factor that we imposed at both $t_f + \Delta$ and t_f. So we must reexamine the matching condition at $t_f + \Delta$; returning to the fourth matching condition and trying to solve for Δ, we see that

$$\frac{T(t_0)}{\delta^{n-1}}(\Delta+\delta)^{n-1} = \frac{1}{2(t_f+\Delta)}\left[a(t_f) - \frac{T(t_0)\delta}{n} + \frac{T(t_0)}{n\delta^{n-1}}(\Delta+\delta)^n\right] \tag{5.11}$$

$$T(t_0)\left(1+\frac{\Delta}{\delta}\right)^{n-1} = \frac{1}{2(t_f+\Delta)}\left[\frac{T(t_0)}{H} - \frac{T(t_0)\delta}{n} + \frac{T(t_0)\delta}{n}\left(1+\frac{\Delta}{\delta}\right)^n\right] \tag{5.12}$$

$$0 = \frac{1}{H} - \frac{\delta}{n} + \frac{\delta}{n}\left(1+\frac{\Delta}{\delta}\right)^n - 2(t_f+\Delta)\left(1+\frac{\Delta}{\delta}\right)^{n-1}. \tag{5.13}$$

With $\delta = \frac{n}{H}$, this simplifies to

$$2(t_f+\Delta) = \frac{1}{H}\left(1+\frac{H\Delta}{n}\right) \tag{5.14}$$

$$\Delta = \frac{\frac{1}{H} - 2t_f}{2 - \frac{1}{n}}. \tag{5.15}$$

So the transition period Δ is undefined for $n = \frac{1}{2}$, which invalidates the claim of first-derivative smoothness imposed by the eq. (4.17) parameters, $\delta \approx 2.65 \times 10^{-6}\Delta$. For $n \approx 0.5002$, associated with $\epsilon_H = 2$, the new formula's value of Δ is in fact less than zero. Since Δ is supposed to represent the length of time over which the interpolating function applies, this value is manifestly unphysical.

Furthermore, substituting $\delta = n/H$ in the interpolating scale factor,

$$a_p(t) = a(t_f) - \frac{T(t_0)\delta}{n} + \frac{T(t_0)\delta}{n}\left(1+\frac{t-t_f}{\delta}\right)^n \tag{5.16}$$

$$= \frac{T(t_0)\delta}{n}\left(1+\frac{t-t_f}{\delta}\right)^n, \tag{5.17}$$

eliminates the a-axis displacement of $a_p(t)$. We introduced the displacement of the power-law vertex in section 4.1.1 in order to enforce the smoothness condition at t_f, but this would be undone by the assumption of exact continuity of the equation of state.

The Lozanov graphical approach to analyzing the equation of state suggests a range of power law indices, $0.5000 \lesssim n \lesssim 0.5002$, are reasonable, and this is supported by the values

that are permitted by the speed-of-sound constraints, $0.4990 \lesssim n \lesssim 0.5005$. Having tried unsuccessfully to establish continuity with the equation of state at $t_f + \Delta$, we now seek an explanation of the discontinuity. If the transition represents a continuation and ultimately a termination of inflation, a local discontinuity might result from a weak phase transition of unknown character. A second explanation may be that a power law index not equal to 0.5 in the transition signals that the composition of the universe is not strictly radiation-dominated as the transition ends, and so a single-component model is not sufficient to describe the dynamics.

Chapter 6

Summary of Numerical Results

We have found that a transition function with power-law index n can provide seamless first-derivative smoothness over the period between the end of inflation and the development of a single-component n-era universe, while obeying fundamental stability and causality constraints. During the transition, the scale factor increases by approximately an order of magnitude more, compared with what it would have been in a model with a sharp cusp dividing the inflationary from post-inflationary functional forms; and that additional accumulated expansion factor remains as time progresses. Figure 6.1 shows the key comparisons.

Figure 6.2 depicts the increases toward asymptotic limits more clearly. Both figures 6.1 and 6.2 also reveal that these increases occur primarily in the vicinity of $t = 10^{-37}$ s and do not particularly depend on the duration of the transition Δ. Table 6.1 contains further data, including how much larger, relatively speaking, the universes with the smooth interpolations are than the models without smoothing. The underlying numbers show that after 10^{-34} s, the asymptotic values 9.8 and 11.2 have completely stabilized (to over 12-decimal-place precision). The percentages represent the degree to which the ratios have approached the asymptotic values reached at 10^{-34} s. Even by 10^{-37} s, the increased expansion factors have already grown to be within 2% of their asymptotic values.

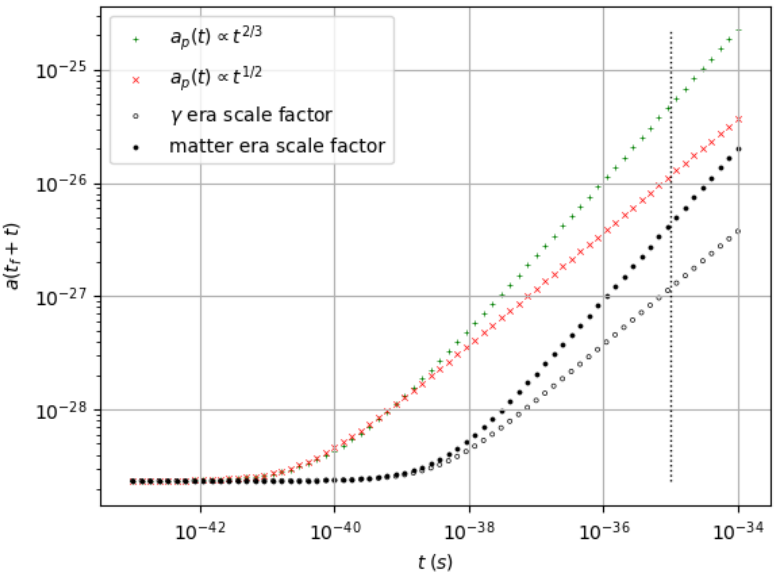

(a)

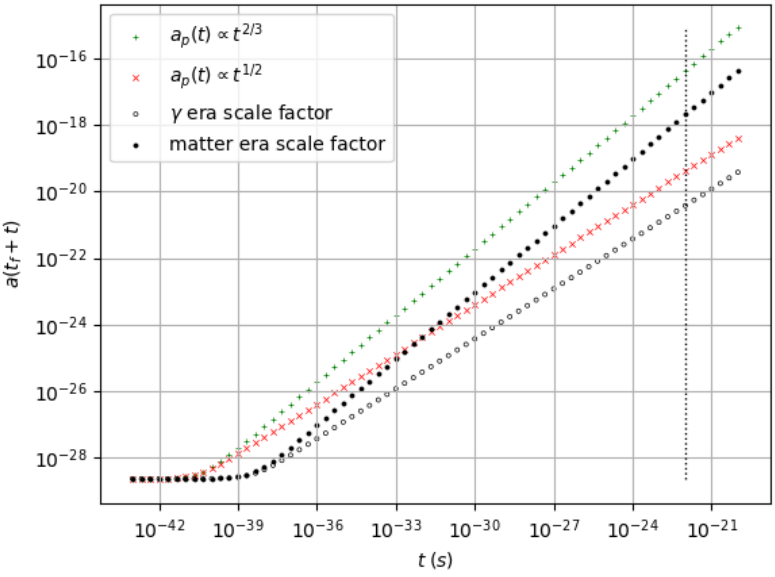

(b)

Figure 6.1 The growth in scale factors $a(t_f + t)$ for single-component universes with smoothness enforced at $t_f + \Delta$ with $\Delta = 10^{-35}$ s and 10^{-22} s in (a) and (b), respectively. We note that the approximate order-of-magnitude increases in the power law scale factors occur at around 10^{-37} s in all cases.

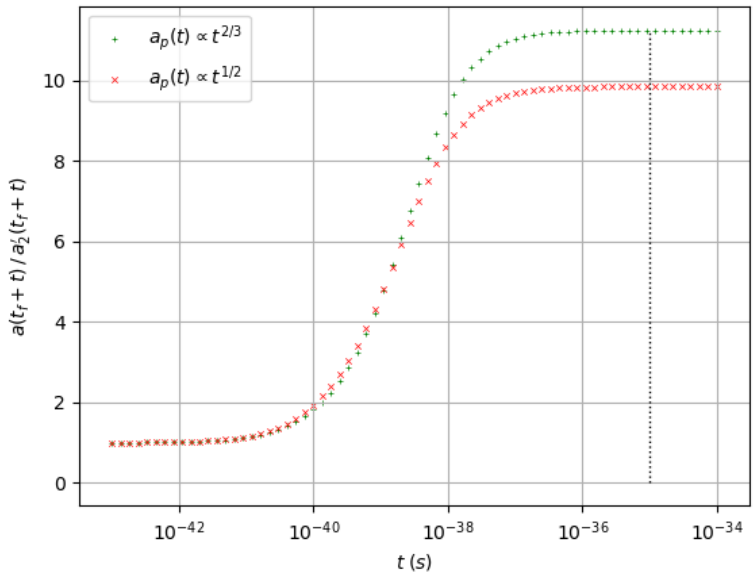

Figure 6.2 The scale factor ratios $\frac{a_p(t)}{a_2'(t)}$. At approximately $t = 10^{-37}$ s, the ratios reach greater than 98% of the asymptotic values of 9.8 and 11.2 for $a_p(t) \propto t^{1/2}$ and $a_p(t) \propto t^{2/3}$, respectively.

Table 6.1 The ratios of $a_p(t)$ to $a_2'(t)$ at different times during the interpolation period.

	$a_p(t) \propto t^{1/2}$		$a_p(t) \propto t^{2/3}$	
Time (s)	Ratio	%	Ratio	%
10^{-34}	9.837	100	11.227	100
10^{-36}	9.828	99.9	11.217	99.9
10^{-37}	9.69	98.5	11.03	98.3
10^{-38}	8.4	85.8	9.4	83.3

We are left with the interesting result about what happens when we insert an interpolating function after the end of inflation to smooth out the dynamics. Compared with the models with discontinuous derivatives—signifying abrupt transitions between the inflationary period and a period with a different equation of state—the total expansion of the scale factor is greater by about an order of magnitude (or between 2 and 3 e-folds). In a way, this is unsurprising, since the interpolating function allows the inflationary expansion

to tail off a bit more gradually, and so the net result is always a larger universe at later times. This kind of increase in the scale factor will form the basis for our analysis of the effect of continuity in the numerical analysis going forward.

Chapter 7

The Smooth Scale Factor in the Preheating Model

Having concluded that enforcing a smooth transition results in an order-of-magnitude increase in the ultimate scale factor of the subsequent single-component universe, we shall now examine the effects of this change on reheating, based on the preheating model of KLS [50], in which the inflaton couples to a second scalar field χ in the era following after inflation, which is taken to be a matter-dominated universe. We shall evaluate preheating effects using a smooth interpolating power law with $n = \frac{2}{3}$, as described previously in section 4.1 as an example of a power law with $n < 1$. We compare our results to those of the KLS model, which employs the scale factor $a(t) \approx a_f(t/t_f)^{2/3}$ with a discontinuous slope. Our numerical analysis shows that the larger scale factor in the smooth model decreases the χ occupation numbers n_k and dilutes the total number density n_χ. The dilution arises naturally out of the volume increase due to the greater expansion of space—although the broad parametric resonance during preheating partially offsets the effect. Broad parametric resonance involves all modes of the scalar field χ less than a specific maximum being involved in quasi-resonant interactions with the inflaton, and it causes an exponential increase in the number of χ particles created. Appendix F summarizes the parameters used in the numerical analysis, a description of each, and their units.

7.1 Occupation Numbers

In this section and section 7.2, we briefly summarize the foundations of the detailed, extensive case that KLS present in support of their theory. The Lagrange density for the scalar

field χ coupled to the inflaton,

$$\mathcal{L} = \frac{1}{2}\chi_{,\mu}\chi^{,\mu} - \frac{1}{2}m_\chi^2\chi^2 - \frac{1}{2}g^2\phi^2\chi^2, \tag{7.1}$$

in expanding space with vanishing mass parameter $m_\chi = 0$, generates the equation of motion

$$\ddot{\chi}_k + \frac{3\dot{a}}{a}\dot{\chi}_k + \left(\frac{k^2}{a^2} + g^2\phi^2\right)\chi_k = 0, \tag{7.2}$$

where $k = \sqrt{\mathbf{k}^2}$, for the Fourier mode χ_k in momentum space. The inflaton at the end of inflation is a coherently oscillating field of form $\phi(t) = \Phi(t)\sin(mt)$, with amplitude envelope $\Phi(t) = \frac{M_P}{\sqrt{3\pi}mt}$ [52], so that

$$\ddot{\chi}_k + \frac{3\dot{a}}{a}\dot{\chi}_k + \left[\frac{k^2}{a^2} + g^2\Phi^2(t)\sin^2(mt)\right]\chi_k = 0. \tag{7.3}$$

In slow roll inflation, chaotic inflation, and other inflationary models in which the friction term $3H\dot{\phi}$ in the equation of motion (2.36) becomes negligible, the inflaton exhibits sinusoidal oscillating behavior around $\phi = 0$. (Here the argument of the sine function has time t in units of m^{-1}, the mass of the inflaton, which the KLS model uses throughout.) The appearance of the Planck mass M_P in $\Phi(t)$ derives from the Hubble parameter expressed in terms of the gravitational constant. The units of k are m, and the scale factor, normalized in the Robertson–Walker metric with $a(t_0) = 1$ today, remains dimensionless.

Broad parametric resonance consists of non-adiabatic oscillation of the χ field in Fourier-space regions where the equation of motion is unstable. The character of the instability is revealed by converting eq. (7.3) into the standard Mathieu equation. Rescaling the scalar field,

$$X_k = a^{3/2}\chi_k, \tag{7.4}$$

eliminates the friction-like term and so yields

$$\ddot{X}_k + \left[\frac{k^2}{a^2} + g^2\Phi^2(t)\sin^2(mt)\right]X_k = 0. \tag{7.5}$$

Now, recasting the argument of the oscillating term by setting $z = mt$ completes the conversion into the Mathieu equation:

$$X_k'' + [A_k + 2q\cos(2z)]\, X_k = 0. \tag{7.6}$$

The prime represents the derivative with respect to the argument z, and the two parameters in the equation are

$$A_k = \frac{k^2}{a^2 m^2} + 2q, \quad q = \frac{g^2 \Phi^2(t)}{4m^2}. \tag{7.7}$$

The resonance behavior of solutions to the Mathieu equation depends on the values of these A_k and q, which determine the stable and unstable regions. Appendix G reproduces the standard plot depicting the stability and instability regions in the q-A_k plane with a graph of the Mathieu equation parameters.

The oscillations of the scalar field exhibit adiabatic instability when

$$\frac{\dot{\omega}}{\omega^2} \gtrsim 1, \tag{7.8}$$

and energy transfer occurs between the inflaton and the scalar field χ. Trial solutions of the Mathieu equation,

$$X_k \propto e^{\mu_k z}, \tag{7.9}$$

are unstable for real values of the Floquet characteristic exponent μ_k [59, 60]. Section 7.2 discusses μ_k in more detail.

The mode occupation number n_k is the energy of the mode in question, divided by the single-particle energy ω_k:

$$n_k = \frac{\omega_k}{2}\left(\frac{|\dot{X}_k|^2}{\omega_k^2} + |X_k|^2\right) - n_{k\,0}. \tag{7.10}$$

(The adjustment $-n_{k\,0}$ to account for the zero-point energy density is effectively negligible.) Figure 7.1 reproduces the results of the discontinuous scale factor of the KLS model, for the scalar field mode amplitude X_k and the exponential increase in the corresponding

occupation number $\log n_k$. The t-axis timeline of both graphs becomes a count of the number of oscillations of the inflaton after t is expressed in units of $\frac{2\pi}{m}$, with which the revised equation of motion (7.5) is

$$\ddot{X}_k + (2\pi)^2 \left[\frac{k^2}{a^2} + g^2 \Phi^2(t) \sin^2(2\pi t) \right] X_k = 0. \tag{7.11}$$

We have selected the specific mode of the KLS model with the wave number $k = 4m$, where $m = 10^{-6}\ M_P$, to maximize the growth of the occupation number. To reproduce the broad-resonance exponential growth, we have used parameters $g = 6.25 \times 10^{-4}$, $\dot{X}(t_f) = 0.045$, and $\ddot{X}(t_f) \approx 0$; these were identified empirically, and varying the parameter values away from these will decrease the observable resonance effect. The scalar field derivative $\dot{X}(t_f)$ approximates what KLS advise—namely, that the positive-frequency solution $X_k(t) \approx \exp\left(-i\omega_k t / \sqrt{2\omega_k}\right)$ be applied as an initial condition.

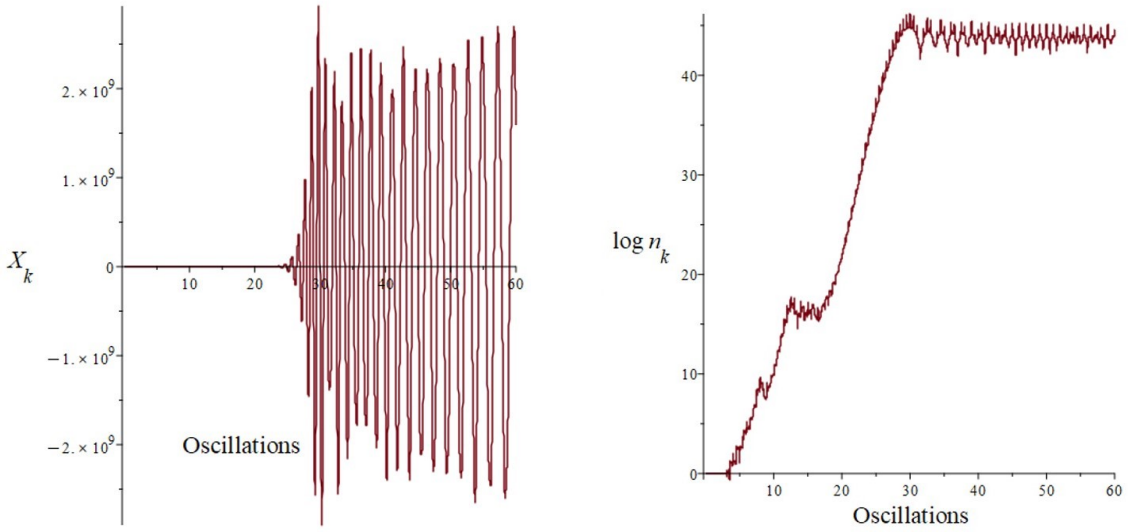

(a) (b)

Figure 7.1 The scalar field and occupation number for the first 60 oscillations in the model with a discontinuous scale factor

Broad parametric resonance preheating requires certain preconditions on $\Phi(t)$ and the Mathieu equation parameter q, and it begins shortly after the end of inflation, after approximately one quarter of an oscillation of the inflaton. (KLS use this approximation to advance their analysis.) With time defined in terms of the number of oscillation cycles,

$t_f = \frac{\pi}{2m} \approx 10^{-37}$ s, which makes the timeline consistent with that which we have found for the continuous scale factor; our order-of-magnitude increase in the size of the cosmos also appears at around 10^{-37} s.

In graph (b) of figure 7.1, the scalar field spans many instability bands in the first ~ 10 oscillations, as q decreases substantially, and the resonances cause exponential growth in the occupation number. From about 12 to 17 oscillations, the growth flattens as q lessens while crossing the stability region corresponding to q values decreasing from about 2 to 1. Broad resonance and growth resume in the next 10 oscillations in the instability band for $q \lesssim 1$ and $A_k \approx 1$, before ultimately terminating after ~ 34 oscillations. Appendix H also shows graph (b) of figure 7.1 superimposed on the final three instability regions of figure G.1 (corresponding to decreasing q as time progresses).

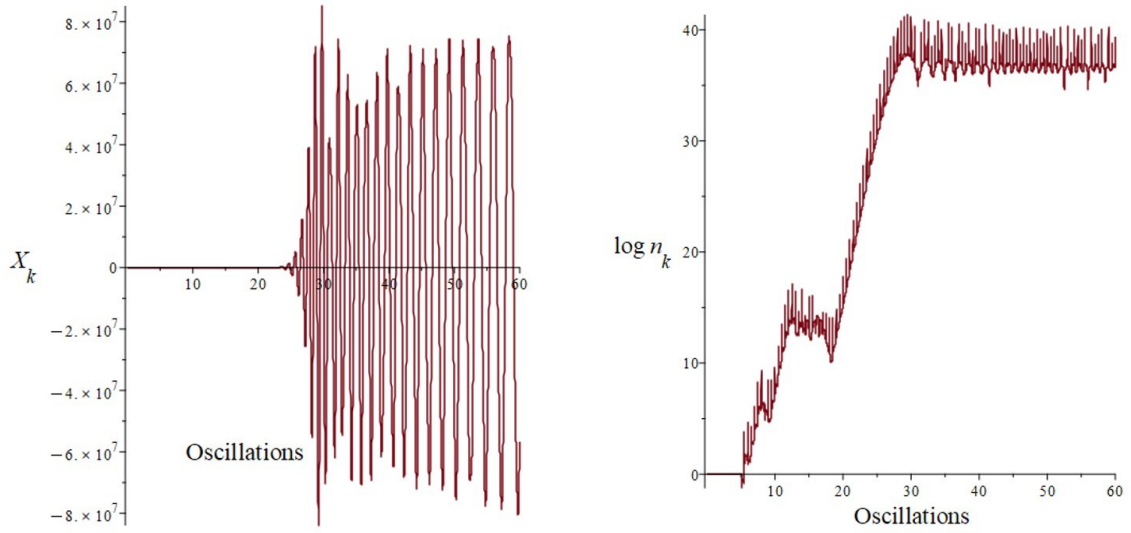

(a) (b)

Figure 7.2 The scalar field and occupation number for the first 60 oscillations in a model with the continuous scale factor

In figure 7.2, we repeat the presentation from figure 7.1 using the smooth transitional scale factor in place of the kinked scale factor of the KLS model. The scalar field and occupation number show sharp decreases from figure 7.1 to figure 7.2 because of the effect of the order-of-magnitude increase in $a(t)$. We can examine the effect of the continuous

scale factor more precisely by analyzing the root mean squares of X_k and n_k averaged over the 10 oscillations following the end of preheating, which occurs after approximately 34 oscillations. With time t in units of m^{-1} according to the KLS formalism, we can convert the scale factor units of time in seconds to oscillations,

$$a(t) \approx \left[\frac{t\,(\mathrm{s})}{t_f}\right]^{2/3} = \left[\frac{t\,(\mathrm{s})\left(\frac{2\pi/m}{\mathrm{s}}\right)}{\frac{\pi}{2m}}\right]^{2/3} = (4t)^{2/3}. \tag{7.12}$$

We have also used the assumption for t_f that broad parametric preheating begins after inflation ends, at one fourth of an oscillation. Then we apply a factor of 10 for the approximate order-of-magnitude increase in the continuous $a(t)$,

$$a(t) \to 10a(t) \approx 10(4t)^{2/3}. \tag{7.13}$$

For X_k (in the $k = 4m$ mode), we find a modest decline of ~ 0.03 in the root mean square, due to the order-of-magnitude increase in the scale factor. Figure 7.3 shows $\log n_k$ for both forms of the scale factor for 10 oscillations following the end of broad resonance. The decrease in $\log n_k$ because of the effect of the larger scale factor causes a reduction of just ~ 0.002 in the root mean square of the occupation number n_k at 10 oscillations after broad resonance terminates.

Local maxima in $\log n_k$ for the smooth scale factor in figure 7.3 occur at every half oscillation of ϕ at $t = \frac{1}{2}, 1, \frac{3}{2}, \ldots$. At these points, where $\sin(2\pi t) = 0$ in eq. (7.11), the frequency reduces to

$$\omega_k = 2\pi\frac{k}{a}, \tag{7.14}$$

with values less than one, $0.080 \lesssim \omega_k \lesssim 0.095$. For the 10 oscillation periods under consideration with the smooth scale factor model, this range of fractional frequencies has the effect of increasing the contribution of the term containing the kinetic energy $\dot{X}_k$ in the occupation number,

$$n_k = \frac{\omega_k}{2}\left(\frac{|\dot{X}_k|^2}{\omega_k^2} + |X_k|^2\right) - n_{k\,0}, \tag{7.15}$$

even as it tends to suppress the contribution of the potential-like X_k term. Thus, the small fractional frequency generates the local maxima. The range of larger frequencies with the

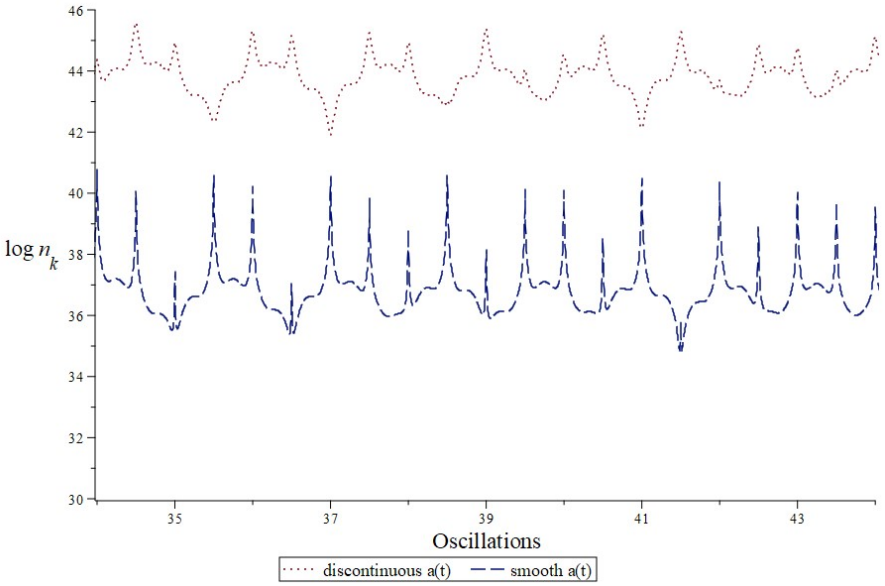

Figure 7.3 These plots compare 10 oscillations of $\log n_k$ after the end of broad resonance at ~ 34 oscillations for the two functional forms of the scale factor.

cusped scale factor following the end of resonance, $0.80 \lesssim \omega_k \lesssim 0.95$, has less of an effect and intersperses some local minima, depending on the relative values of $\dot{X}_k$ and X_k at the half-oscillation times.

We are able to provide some understanding of the differences in appearance of $\log n_k$—that is, the greater degree of dispersion of the amplitudes above the average occupation number in graph (b) of figure 7.2 in comparison with figure 7.1—by examining in detail the effect of the fractional frequency. At oscillation 36, for example, the occupation numbers $\log n_k(36)$ are approximately 45.3 and 40.2 for the cusped and smooth scale factor models, respectively. The kinetic term in the energy, amplified by the frequency, for the most part determines the occupation number in both models. The average occupation numbers over 4 oscillations from oscillation 34 to 38 are approximately 43.9 and 36.8, respectively—yielding an increase during this period of ~ 0.03 with the cusped scale factor and ~ 0.09 with the smooth model. The lower level of the scalar field in the smooth model and (more importantly) its time derivative moderate what would otherwise be an approximately 10-fold difference in the increases based on the values of ω_k alone. Thus, we see the greater dispersion of amplitudes above the average $\log n_k$ in figure 7.2. Appendix I

contains a table that lists some of the supporting data associated with the behavior around oscillation 36, as well as related graphs.

7.2 Number Density

The number density of the scalar field quanta has its basis in the process of broad parametric resonance KLS characterize in their paper as *stochastic*—that is, random. They show that the variation in the phase θ_k of the scalar field χ in the course of semiclassical interactions between the χ-particles and the oscillating inflaton field is very much greater than π, which makes successive phases effectively random. However, this does not mean that the there is no net energy flow from one sector to the other. In fact, a growth in the number of particles between classical scattering events can be as much as 3 times as probable as a decrease, based on the numerical effect of possible values for the phase angle in the recurrence relation governing resonance. KLS also separate preheating into two time periods. The first period precedes all backreaction and rescattering, and the second period involves the effect of those interactions on number density, which can be significant. Backreaction and rescattering are quantum effects in which the created χ-particles interact with the background inflaton field. In backreaction, interactions can alter the effective masses of the particles and the frequency of the inflaton oscillations. Rescattering involves a created particle scattering again, either off an inflaton or another χ-particle. However, KLS conclude that the duration of the second period is so brief that during it they can safely neglect the expansion of the universe, and their analysis of that part does not depend on the scale factor. Therefore, here we shall determine the effect of the continuous scale factor on number density conversely without including backreaction and rescattering.

Semiclassical scattering leading to quantum-mechanical χ-particle production involves the interaction of the scalar field χ and the background inflaton field oscillating around zero. KLS derive the number density of the χ field from the adiabatic approximation solution to

eq. (7.5),

$$X_k(t) = \frac{\alpha_k(t)}{\sqrt{\omega_k}} e^{-i\int^{t_j} dt\, \omega_k} + \frac{\beta_k(t)}{\sqrt{\omega_k}} e^{+i\int^{t_j} dt\, \omega_k}, \tag{7.16}$$

with the scalar field phase $\theta_k^j = \int^{t_j} dt\, \omega_k$ and t_j representing the time at end of the j^{th} oscillation—such that as time $t \to t_j$, the inflaton field is oscillating around its minimum, $\phi \to 0$. The functions $\alpha_k(t)$ and $\beta_k(t)$ are time-dependent Bogoliubov transformation coefficients [61].

Around $\phi \approx 0$, eq. (7.5) becomes

$$\ddot{X}_k + \left[\frac{k^2}{a^2} + g^2\Phi^2(t)m^2(t - t_j)^2\right] X_k = 0. \tag{7.17}$$

The scalar field χ with an effectively random phase θ_k^j completes a half-oscillation at time $t \to t_j$ for $j = 1, 2, 3, \ldots$. As $t \to t_j$ for each half-oscillation of χ, the inflaton field concurrently oscillates near zero, creating a period of non-adiabatic energy transfer, which leads to exponential growth in the number of χ-quanta according to eq. (7.8). At other times, the number density n_χ remains stable. Introduction of parameters

$$\tau = k_*(t - t_j) \text{ and } \kappa = \frac{k}{ak_*} \tag{7.18}$$

recasts eq. (7.17) as a differential equation with a parabolic cylinder function solution,

$$\frac{d^2X_k}{d\tau^2} + (\kappa^2 + \tau^2)X_k = 0, \tag{7.19}$$

which is also the Schrödinger equation with an unstable quadratic potential, $V(\phi) \propto -\tau^2$. Appendix J derives the largest mode to participate in the broad parametric resonance, $k_* = \sqrt{gm\Phi}$. The scattering of solutions X_k of eq. (7.5) leads to a recurrence relation for the Bogoliubov coefficients, which may be represented by transfer matrix,

$$\begin{pmatrix} \alpha_k^{j+1} e^{-i\theta_k^j} \\ \beta_k^{j+1} e^{+i\theta_k^j} \end{pmatrix} = \begin{pmatrix} \frac{1}{D_k} & \frac{R_k^*}{D_k^*} \\ \frac{R_k}{D_k} & \frac{1}{D_k^*} \end{pmatrix} \begin{pmatrix} \alpha_k^j e^{-i\theta_k^j} \\ \beta_k^j e^{+i\theta_k^j} \end{pmatrix}. \tag{7.20}$$

KLS provide the reflection R_k and transmission D_k amplitudes from the solutions of the parabolic cylinder equation and also the phase angle φ_k, which is a complicated function

of the parameter κ,

$$\varphi_k = \arg\Gamma\left(\frac{1+i\kappa^2}{2}\right) + \frac{\kappa^2}{2}\left(1+\log\frac{2}{\kappa^2}\right). \tag{7.21}$$

With these, the recurrence relation becomes

$$\begin{pmatrix}\alpha_k^{j+1}\\ \beta_k^{j+1}\end{pmatrix} = \begin{pmatrix}\sqrt{1+e^{-\pi\kappa^2}}\,e^{i\pi\varphi_k} & ie^{-i\frac{\pi}{2}\kappa^2+2i\theta_k^j}\\ -ie^{-i\frac{\pi}{2}\kappa^2-2i\theta_k^j} & \sqrt{1+e^{-\pi\kappa^2}}\,e^{-i\pi\varphi_k}\end{pmatrix}\begin{pmatrix}\alpha_k^j\\ \beta_k^j\end{pmatrix}. \tag{7.22}$$

Noting that the occupation number n_k in eq. (7.10) just depends on the Bogoliubov coefficient β_k [62],

$$n_k = |\beta_k|^2, \tag{7.23}$$

and that for for a coherent process $n_k \gg 1$, leads to the recurrence relation

$$n_k^{j+1} \approx \left[1 + 2e^{-\pi\kappa^2} - 2\sin(\theta_{\rm tot}^j)\,e^{-\frac{\pi}{2}\kappa^2}\sqrt{1+e^{-\pi\kappa^2}}\right]n_k^j, \tag{7.24}$$

with the accumulated phase

$$\theta_{\rm tot}^j = 2\theta_k^j - \varphi_k + \arg\beta_k^j - \arg\alpha_k^j. \tag{7.25}$$

Because the variation in the phases θ_k^j is very much greater than π, the randomness of θ_k^j—and by extension the randomness of α_k^j and β_k^j as functions of θ_k^j—make $\theta_{\rm tot}^j$ stochastic. Noting that resonance begins to be suppressed unless $\pi\kappa^2 \lesssim 1$, KLS find that for $\pi\kappa^2 \ll 1$, a growth in the number of particles is three times as likely as a decrease. Within the range $0 < \theta_{\rm tot}^j \leq 2\pi$, values of $0 < \theta_{\rm tot}^j < \frac{\pi}{4}$ and $\frac{3\pi}{4} < \theta_{\rm tot}^j \leq 2\pi$ cause an increase in the number of particles according to eq. (7.24); only over one quarter of the possible range of phases, $\frac{\pi}{4} < \theta_{\rm tot}^j \leq \frac{3\pi}{4}$, does the number of χ-particles decrease, as energy flows (incoherently) back to the inflaton field. A second recurrence relation also obtainable [59] from the Mathieu equation (7.6),

$$n_k^{j+1} = n_k^j e^{2\pi\mu_k^j}, \tag{7.26}$$

in combination with eq. (7.24), yields the Floquet characteristic exponent,

$$\mu_k^j = \frac{1}{2\pi}\log\left[1 + 2e^{-\pi\kappa^2} - 2\sin(\theta_{\rm tot}^j)\,e^{-\frac{\pi}{2}\kappa^2}\sqrt{1+e^{-\pi\kappa^2}}\right]. \tag{7.27}$$

Integration of n_k for all modes that participate in broad parametric resonance gives rise to the total number density of χ-quanta,

$$n_\chi = \frac{1}{(2\pi a)^3} \int d^3k\, n_k(t) = \frac{1}{4\pi^2 a^3} \int dk\, k^2 e^{2\mu_k mt}. \tag{7.28}$$

The units of number density n_χ are the expected m^{-3}, since occupation number $n_k(t)$ is dimensionless. KLS evaluate the integral on the far-right-hand side of eq. (7.28) by the steepest descent method and estimate the number density to be

$$n_\chi \approx \frac{k_*^3}{64\pi^2 a^3 \sqrt{\pi\mu mt}} e^{2\mu mt}. \tag{7.29}$$

They also determine the maximum Floquet characteristic exponent μ associated with an unknown maximum $k_{\max}$, estimated as $k_{\max} \approx \frac{k_*}{2}$.

We use the proportionality

$$n_\chi \propto \frac{1}{a^3 \sqrt{\mu mt}} e^{2\mu mt} \tag{7.30}$$

to perform a numerical analysis of the effect of the continuous scale factor by examining the ratio

$$R_\chi = \frac{n_{\chi\, a(t)_{\mathrm{smooth}}}}{n_{\chi\, a(t)_{\mathrm{cusp}}}}. \tag{7.31}$$

The ratio R_χ between terms $n_{\chi\, a(t)_{\mathrm{smooth}}}$ and $n_{\chi\, a(t)_{\mathrm{cusp}}}$ represents the number density of the smooth scale factor model to that with a discontinuous derivative at the end of inflation, as used by KLS. We anticipate a decrease in the number density due to the increase in volume, moderated to a certain amount by the dependence of the proportionality in eq. (7.30) on μ. The use of the proportionality eliminates the dependence on the unknown mode k_*, which KLS estimate as $k_*(t) \approx \sqrt{gm\Phi(t)}$, as detailed in Appendix J.

In the absence of $\frac{e^{2\mu mt}}{\sqrt{\mu mt}}$, the greater time allowed for the expansion of space as inflation tails off in the smooth model would on its own cause dilution—that is, a decrease in the number density. The order-of-magnitude increase in the smooth scale factor alone would reduce the number density by the cube of the scale factor increase, $\sim 10^{-3}$. However, the effect of the broad parametric resonance in preheating—in particular, the term $\frac{e^{2\mu mt}}{\sqrt{\mu mt}} > 1$—partially offsets the dilution of the $\sim 10^{-3}$ increase in the volume of space. The extent of the

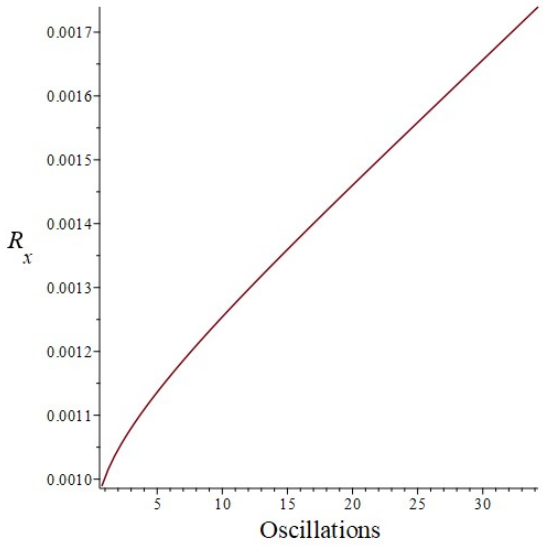

Figure 7.4 The ratios R_χ represent the minimal dilution of the smooth scale factor. Maximizing the offset with total phase $\sin(\theta^j_{\rm tot}) = -1$ in eq. (7.27) minimizes the dilution.

offset is dependent on the stochastic $\sin(\theta^j_{\rm tot})$ in eq. (7.27). Figure 7.4 displays the ratio R_χ of number density of the smooth scale factor to the discontinuous scale factor as a function of time (again expressed as the number of oscillations). The value of the ratio at the start of preheating, $\sim 10^{-3}$, reflects the effect only of the expansion of space. As preheating progresses, however, R_χ rises to a level slightly greater than 1.7×10^{-3} at the end of broad parametric resonance, at around 34 oscillations, in the limiting case in which $\sin(\theta^j_{\rm tot})$ is consistently equal to -1. In contrast, as $\sin(\theta^j_{\rm tot})$ increases toward 1, R_χ decreases. For example, at $\sin(\theta^j_{\rm tot}) = 0$, $R_\chi \sim 1.6 \times 10^{-3}$, and R_χ is about 1.3×10^{-3} at $\sin(\theta^j_{\rm tot}) = 0.65$. With a slightly larger stochastic value, $n_{\chi\, a(t)_{\rm cusp}}$ is not directly calculable via this method at lower oscillations, and with a stochastic phase of 0.8, the calculations of both $n_{\chi\, a(t)_{\rm cusp}}$ and $n_{\chi\, a(t)_{\rm smooth}}$, even at the end of 34 oscillations, because that would require the Floquet index μ in eq. (7.27) to be negative. The negative Floquet index signals an essentially unphysical solution, which the model formalism does not support; physically this scenario would describe a net energy flowing back into the inflaton field, while mathematically the formalism breaks down because the saddle point integration method is no longer usable. Thus, examination of the ratio R_χ places a bound on the effect of the continuous scale factor.

The reduction of the number density due to the expansion of space alone, $\sim 10^{-3}$, increases only slightly, by at most about 1.7×10^{-3} after preheating, depending on the values of the stochastic $\sin(\theta^{j}_{\rm tot})$ angles.

Chapter 8

Conclusion

This work has explored the consequences of applying the reasonable expectation of smoothness to the physical expansion of space, as expressed by the characteristic scale factors defining the early universe evolving through its generally-accepted, broadly-defined epochs. We focused on the nearly instantaneous slice of time separating the inflationary era and the subsequent era in which the stress-energy tensor was assumed to be dominated by a single component, either radiation or matter. We focused on the transition out of inflation specifically because it is where we inevitably expect to find the sharpest change in the behavior of the scale factor; assuming some realistic values for primordial parameters reveals that the time derivative of the scale factor can decrease by a factor of $\frac{1}{120}$ between inflation and the radiation era. Rather than being guided by a specific equation of state model, we imposed a first-derivative smoothness requirement upon the scale factor and looked at phenomenalistic interpolating functions that could connect the inflation and subsequent eras. The assumption of a continuously, steadily declining (but not contracting) slope after the end of inflation led to an in-depth examination of families of interpolating candidates with shifted power-law dependencies on time. We imposed the same requirements of smoothness at the beginning and at the end of the brief interpolating transition period.

From these matching conditions, we uncovered that it was necessary to place the vertices of power law interpolating functions with indices $n < 1$ prior to the end of inflation at t_f and the vertices of functions with $n > 1$ subsequent to t_f, with the displacement in either case parameterized by δ. Also initially unknown was the transition period Δ—the duration of the period between the end of inflation and the single-component universe

(whether modeled as composed of radiation or matter). However, implicit in our transition model was a remaining uncertainty in the parameters of the model. We cannot find specific expressions for all of them without imposing additional conditions, and we can do no better than finally expressing the displacement δ in terms of the transition period Δ. Graphical analysis of the Hubble parameter and the equation-of-state and speed-of-sound stability and causality constraints allowed us to identify physically reasonable interpolating power-law functions as those having indices that approached the power-law indices $\frac{1}{2}$ and $\frac{2}{3}$ for radiation and matter single-component universes, respectively. Numerical analyses demonstrate the remarkable result that the actual transition lasts approximately 10^{-37} s, essentially regardless of the composition of the single-component universe that follows the transition and the duration Δ. In addition, the universe enters the single-component era about an order of magnitude (or approximately 2–3 e-folds) larger than it would have been if subject to a scale factor with a discontinuous slope, which switched instantaneously to $t^{1/2}$ or $t^{2/3}$ behavior at the end of the inflationary epoch. Although the form of the interpolating function is not exponential, the increase in the lifespan of the universe, 10^{-37} s, is not inconsequential compared to the assumption for the inflationary expansion of the universe, $N \approx 60$ e-folds. We understand the outcome to be a universe given an additional short sliver of time in which to grow larger simply because we have imposed a condition of smoothness on the physical expansion of space. The numerical analysis adds precision to this result. For a radiation-dominated era following the transition, at 10^{-37} s the increase in the size of the universe has attained 98.5% of its asymptotic value, and the corresponding figure for a subsequent matter-dominated era is 98.3%. Generalizing the approach we have used to a multiple-component universe would also be interesting, as would considering the high-scale physics of inflation that might provide the friction needed to end inflation in a smoother way.

We proceeded to examine the effect of the theoretical changes we had described to the dynamic expansion of space (characterized by a smooth scale factor and the resulting pre-

dicted increase in the size of the universe) on a subsequent preheating era. The evolution of the universe after inflation remains highly speculative because of the challenges implicit in experimental confirmation. A period of reheating appears to be required in order to be consistent with the later stages of cosmological development, but the details of the reheating dynamics can depend sensitively on the nature of the particle species available to be excited—including as-yet unobserved high-mass species that may not be accessible at standard model scales but could nonetheless have been active participants in the dynamics of the hot, dense early universe. However, we have also discussed the intricate, highly-technical theory of preheating developed by Kofman, Linde, and Starobinsky to address some generic problems with reheating. We applied the KLS formalism to our model with a smooth interpolating scale factor leading into a matter-dominated universe, in order to gauge the effects of the smoothing on the most sensitive χ-particle occupation number n_k and the corresponding number density n_χ. We were able to estimate the numerical changes compared with the results obtained using the standard cusped scale factor, and we concluded that the differences are not necessarily numerically significant, apart from a dilution in the total particle density that should be common to all models that predict somewhat larger universes after the end of inflation. Specifically, for the occupation number of the most aggressively growing χ mode, we find a modest decline in $\log n_{k=4m}$ of $\sim 2 \times 10^{-3}$ in the root mean square for 10 oscillations following the end of broad parametric resonance, which is a consequence of a decrease of just $\sim 3 \times 10^{-2}$ in the root mean square of the scalar field χ_k over the same period. In addition, by constructing a relation consisting of the ratio of the number density in the cosmology with the smooth scale factor to that with the cusped scale factor, we determine a partial offset to the expected dilution of the quantity of bosons produced by broad parametric resonance due to the approximate 10^3 increase in the unit volume of space caused by the larger smooth scale factor. The stochastic nature of broad parametric resonance precludes a specific prediction, but we find an additional modest increase in the proportion, with an upper bound of $\lesssim 1.7 \times 10^{-3}$.

It may be somewhat surprising that the effect of a proposed smoothing of the scale factor is so minor—mostly limited to the natural rarefaction of the χ particles that comes with a spatially larger universe. Regarding the possibility (in a case of optimal phase alignment) of, at most, an additional near doubling per unit volume of number density, we note that a doubling of a small number of something in a unit volume may easily be thought of as not negligible. However, in terms of the many, many orders of magnitude of primal particles in a unit volume of early space, we consider the outcome of having, at most, close to twice as many as not of substance. Thus, we view the result of the numerical analysis of the effect of a not insignificant increase in the size of the universe to represent confirmation of the comparative invariance of the KLS preheating model to these kinds of modifications. We are satisfied that result should represent a modestly useful contribution to the body of work in support of this iconic theory.

Bibliography

[1] A. Friedmann, "About the curvature of space," Journal of Physics **10**, 377–386 (1922).

[2] H. P. Robertson, H. P., "Relativistic Cosmology," Rev. Mod. Phys. **5**, 62–90 (1933).

[3] A. G. Walker, "Completely Symmetric Spaces," J. London Math. Soc. **19**, 219–226 (1944).

[4] J. V. Narlikar, *An Introduction to Cosmology*, Cambridge University Press (2002).

[5] S. Weinberg, *Gravitation and Cosmology: Principles and Applications of the General Theory of Relativity*, John Wiley & Sons, Inc. (1972).

[6] D. Baumann, "Cosmology," Lecture Notes, http://cosmology.amsterdam/education/cosmology.

[7] O. F. Piattella, "Lecture Notes in Cosmology," arXiv:1803.00070 [astro-ph.CO].

[8] S. M. Carroll, "Lecture Notes on General Relativity," arXiv:9712019 [gr-gc].

[9] B. Schutz, *A First Course in General Relativity*, Cambridge University Press, New York (2009).

[10] A. H. Jaffe, "Cosmology 2012: Lecture Notes," Imperial College, London.

[11] B. Ryden, *Introduction to Cosmology* (Addison Wesley, San Francisco, 2003).

[12] A. R. Liddle and D. H. Lyth, *Cosmological Inflation and Large-Scale Structure* (Cambridge University Press, New York, 2006).

[13] A. D. Linde, "The Inflationary Universe," Rep. Prog. Phys. **47**, 925 (1984).

[14] D. Baumann, "TASI Lectures on Inflation," `arXiv:0907.5424`.

[15] J. Lesgourgues, “Inflationary Cosmology,” Lecture Notes, https://lesgourg.github.io/courses.html.

[16] A. R. Liddle, *An Introduction to Modern Cosmology* (Wiley & Sons, West Sussex, 2015).

[17] B. A. Bassett, S. Tsujikawa, and D. Wands, “Inflation Dynamics and Reheating,” Rev. Mod. Phys. **78**, 537 (2006); arXiv:astro-ph/0507632.

[18] W. H. Kinney, “Cosmology, Inflation, and the Physics of Nothing,” arXiv:astro-ph/0301448.

[19] S. Weinberg, *Cosmology* (Oxford University Press, Oxford, 2008).

[20] Planck Collaboration VI. 2020, "Cosmological Parameters," A&A, **641**, A6.

[21] D. J. Fixsen, "The Temperature of the Cosmic Microwave Background," Astrophys. J. **707**, 916–920 (2009).

[22] G. F. Smoot, et al., "Structure in the COBE Differential Microwave Radiometer First Year Maps," Astrophys. J. **396**, L1 (1992).

[23] P. Halpern and N. Tomasello, "Size of the Observable Universe," Advances in Astrophysics **1** (2016).

[24] G. ’t Hooft, “The Inflationary Universe,” Nucl. Phys. B **79**, 276 (1974).

[25] A. M. Polyakov, “Particle Spectrum in Quantum Field Theory,” JETP Lett. **20**, 194 (1974).

[26] A. H. Guth, "The Inflationary universe: A Possible Solution to the Horizon and Flatness Problems," Phys. Rev. D **23**, 347 (1981).

[27] E. W. Kolb and M. S. Turner, *The Early Universe*, CRC Press, Taylor & Francis Group (2018).

[28] A. D. Linde, “A New Inflationary Universe Scenario: A Possible Solution of the Horizon, Flatness, Homogeneity, Isotropy and Primordial Monopole Problems,” Phys. Lett. B **108**, 389 (1982).

[29] A. D. Linde, “Inflationary Cosmology,” Lect. Notes Phys. **738**, 1–54 (2008); arXiv:hep-th/0705.0164.

[30] D. H. Lyth, “Particle physics models of inflation,” Lect. Notes Phys. **738**, 81 (2008); arXiv:hep-th/0702128.

[31] A. Riotto, “Inflation and the Theory of Cosmological Perturbations,” arXiv:hep-ph/0210162.

[32] A. D. Linde, “Chaotic Inflation,” Phys. Lett. B **129**, 177 (1983). arXiv:0705.0164.

[33] I. Zehavi, et al., “Galaxy Clustering in the Completed SDSS Redshift Survey: The Dependence on Color and Luminosity,” Astrophys. J. **736**, 59–88 (2011); arXiv:astro-ph.CO/1005.2413.

[34] A. D. Linde, “Particle Physics and Inflationary Cosmology,” Contemp. Concepts Phys. **5**, 1–362 (2005); arXiv:hep-th/0503203.

[35] C. L. Bennett, et al., "4-Year COBE DMR Cosmic Microwave Background Observations: Maps and Basic Results," Astrophys. J. **464**, L1–/l4 (1996); arXiv:astro-ph/9601067.

[36] Planck Collaboration VI. 2020, "Diffuse Component Separation," A&A, **641**, A4.

[37] M. White and W. Hu, “The Sachs-Wolfe Effect,” Astron. Astrophys. **321**, 8–9 (1997); arXiv:astro-ph.CO/9609105.

[38] Planck Collaboration X. 2020, "Constraints on inflation," A&A, **641**, A10.

[39] P. Schneider, *Extragalactic Astronomy and Cosmology*, Springer (2015).

[40] E. Komatsu, et al., “First Year Wilkinson Microwave Anisotropy Probe (WMAP) Observations: Tests of Gaussianity,” Astrophys. J. Suppl. **148**, 119–134 (2003); arXiv:astro-ph/0302223.

[41] C. L. Bennett, et al., “Nine-Year Wilkinson Microwave Anisotropy Probe (WMAP) Observations: Final Maps and Results,” arXiv:astro-ph.CO/1212.5225.

[42] D. H. Lyth, “Models of Inflation and the Spectral Index of the Adiabatic Density Perturbation,” (1996); arXiv:hep-ph/9609431

[43] Planck Collaboration XXII. 2014, "Constraints on inflation," A&A, **571**, A22.

[44] N. Bartolo, et al., "Non-Gaussianity from Inflation: Theory and Observations," Phys. Rept. **402**, 103–266 (2004); arXiv:astro-ph/0406398.

[45] D. Baumann, et al., "CMBPol Mission Concept Study: Probing Inflation with CMB Polarization," AIP Conf. Proc. **1141**, 10–120 (2009); arXiv:astro-ph/0811.3919.

[46] W. Hu and M. White, "A CMB Polarization Primer," New Astron. **2**, 323 (1997); arXiv:astro-ph/9706147.

[47] M. Kamionkowski, A. Kosowsky, and A., "Statistics of Cosmic Microwave Background Polarization," Phys.Rev. D **55**, 7368–7388 (1977); arXiv:astro-ph/9611125.

[48] BICEP2 Collaboration, Ade, P. A. R., et al., "BICEP2 I: Detection Of B-mode Polarization at Degree Angular Scales," Phys. Rev. Lett. **112**, 1241101 (2014); arXiv:astro-ph.CO/1403.3985

[49] Planck Collaboration XX. 2016, "Constraints on inflation," A&A, **594**, A20.

[50] L. Kofman, A. D. Linde, and A. A. Starobinsky, "Towards the Theory of Reheating after Inflation," Phys. Rev. D **56**, 3258 (1997); arXiv:hep-ph/9704452.

[51] E. W. Kolb, "Dynamics of the Inflationary Era," arXiv:hep-ph/9910311.

[52] R. Allahverdi, R. Brandenberger, F. Y. Cyr-Racine, and A. Mazumdar, "Reheating in Inflationary Cosmology: Theory and Applications," Ann. Rev. Nucl. Part. Sci. **60**, 27–51 (2010); arXiv:1001.2600.

[53] A. D. Linde, "Inflationary Cosmology and Creation of Matter in the Universe," in S. Bonometto, V. Gorini, and U. Moschella (eds.), *Modern Cosmology* (Institute of Physics Publishing, Bristol, UK, 2002), p. 159–185.

[54] K. Lozanov, "Lectures on Reheating after Inflation," arXiv:1907.04402.

[55] S. Weinberg, "Effective Field Theory, Past and Future," Proc. Sci. **CD09**, 001 (2009); arXiv:0908.1964.

[56] L. Lindblom, "Causal Representations of Neutron-Star Equations of State," Phys. Rev. D **97**, 123019 (2018); arXiv:1804.04072.

[57] G. F. R. Ellis, R. Maartens, and M. A. H. MacCallum,"Causality and the Speed of Sound," Gen. Rel. Grav. **39**, 1651 (2007); gr-qc/0703121.

[58] K. S. Thorne and R. D. Blandford, *Modern Classical Physics* (Princeton University Press, Princeton, 2017).

[59] N. W. McLachlan, *Theory and Applications of Mathieu Functions* (Oxford University Press, London, 1947).

[60] M. Abramowitz and I. Stegun, *Handbook of Mathematical Functions* (Dover, New York, 1972).

[61] N. D. Birrell and P. C. W. Davies, *Quantum Fields in Curved Space* (Cambridge University Press, Cambridge, 1982).

[62] L. Parker, "The Creation of Particles by the Expanding Universe," Ph.D. thesis, Harvard University (1966).

Appendix A

Non-zero Christoffel Symbols

The Appendix contains the remaining non-zero Christoffel symbols.

For $l = m = 1$:

$$\Gamma^{r}_{ji} = \frac{1}{2} g^{rr} \left(\frac{\partial g_{ri}}{\partial x^{j}} + \frac{\partial g_{rj}}{\partial x^{i}} - \frac{\partial g_{ij}}{\partial x^{r}} \right). \tag{A.1}$$

$$\Gamma^{r}_{tr} = \frac{1}{2} g^{rr} \left(\frac{\partial g_{rr}}{\partial x^{t}} + \frac{\partial g_{rt}}{\partial x^{r}} - \frac{\partial g_{tr}}{\partial x^{r}} \right) = \frac{\dot{a}}{a}. \tag{A.2}$$

$$\Gamma^{r}_{rr} = \frac{kr}{1 - kr^{2}};\ \Gamma^{r}_{\theta\theta} = -r(1 - kr^{2});\ \Gamma^{r}_{\phi\phi} = -(1 - kr^{2})[r \sin^{2}(\theta)]. \tag{A.3}$$

For $2 = m = 2$:

$$\Gamma^{\theta}_{ji} = \frac{1}{2} g^{\theta\theta} \left(\frac{\partial g_{\theta i}}{\partial x^{j}} + \frac{\partial g_{\theta j}}{\partial x^{i}} - \frac{\partial g_{ij}}{\partial x^{\theta}} \right). \tag{A.4}$$

$$\Gamma^{\theta}_{t\theta} = \frac{1}{2} g^{\theta\theta} \left(\frac{\partial g_{\theta\theta}}{\partial x^{t}} + \frac{\partial g_{\theta t}}{\partial x^{\theta}} - \frac{\partial g_{t\theta}}{\partial x^{\theta}} \right) = \frac{\dot{a}}{a}. \tag{A.5}$$

$$\Gamma^{\theta}_{r\theta} == \frac{1}{r};\ \Gamma^{\theta}_{\phi\phi} = -\sin(\theta)\cos(\theta). \tag{A.6}$$

For $l = m = 3$:

$$\Gamma^{\phi}_{ji} = \frac{1}{2} g^{\phi\phi} \left(\frac{\partial g_{\phi i}}{\partial x^{j}} + \frac{\partial g_{\phi j}}{\partial x^{i}} - \frac{\partial g_{ij}}{\partial x^{\phi}} \right). \tag{A.7}$$

$$\Gamma^{\phi}_{t\phi} = \frac{1}{2} g^{\phi\phi} \left(\frac{\partial g_{\phi\phi}}{\partial x^{t}} + \frac{\partial g_{\phi t}}{\partial x^{\phi}} - \frac{\partial g_{t\phi}}{\partial x^{\phi}} \right) = \frac{\dot{a}}{a}. \tag{A.8}$$

$$\Gamma^{\phi}_{r\phi} = \frac{1}{r};\ \Gamma^{\phi}_{\theta\phi} = \frac{\cos(\theta)}{\sin(\theta)}. \tag{A.9}$$

Appendix B

Comoving Density Equations

This appendix derives the comoving density equations. A cosmological continuity equation is the basis, which we obtain from the Friedmann and acceleration equations. Differentiating the first Friedmann equation

$$\left(\frac{\dot{a}}{a}\right)^2 = \frac{8\pi G}{3}\rho_t - \frac{k}{a^2}, \tag{B.1}$$

gives

$$-2\left(\frac{\dot{a}}{a}\right)^3 + 2\frac{\dot{a}\ddot{a}}{a^3} = \frac{8\pi G}{3}\dot{\rho} + 2k\frac{\dot{a}}{a^3}. \tag{B.2}$$

After substituting in the above formula k from the first Friedman equation and $\ddot{a}$ from the acceleration equation,

$$\frac{\ddot{a}}{a} = -\frac{4\pi G}{3}(\rho + 3p), \tag{B.3}$$

simplification yields

$$\dot{\rho} = -3\frac{\dot{a}}{a}(\rho + p). \tag{B.4}$$

Equation B.4 is the continuity equation we seek.

Rearranging equation B.4 leaves

$$\frac{\dot{\rho}}{\rho} = -3\frac{\dot{a}}{a}(1 + w). \tag{B.5}$$

with equation of state $w = p/\rho$. After integration, we arrive at

$$\rho = \rho_0 a^{-3(1+w)}. \tag{B.6}$$

The equations of state for matter, radiation, and the vacuum are 0, $\frac{1}{3}$, and -1, respectively, which represent a universe composed completely of dust, relativistic gas, or negative

pressure. Thus, the comoving densities are

$$\rho_m = \frac{\rho_{m,0}}{a^3} \; ; \; \rho_r = \frac{\rho_{r,0}}{a^4} \; ; \; \rho_\Lambda = \rho_{\Lambda,0}. \tag{B.7}$$

Although we derive these ratios from idealized, single-component universes, the trend in flatness shown in Table 1.1 indicates the reasonableness of the assumption.

Direct inspection of the densities themselves brings about the same conclusions about the ratios. A mass density has a comoving dependence of volume on a^3 in the denominator. A radiation density has the same inverse comoving volume dependence and added to it is one more power of the scale factor due to the inverse length dependence of radiative energy, $E = \frac{hc}{\lambda}$. Finally, the vacuum has no dependence on length, so that $\rho_\Lambda = \rho_{\Lambda,0}$ without adjustment.

Appendix C

Temperature and the Scale Factor

In this appendix, we review the derivation of the inverse relation between the radiation temperature of the universe and the scale factor, following the approach outlined by Ryden [11]. In an isothermal environment, the first law of thermodynamics

$$dQ = dE + p\,dV \tag{C.1}$$

reduces to

$$\frac{dE}{dt} = -p\frac{dV}{dt}. \tag{C.2}$$

After substituting the pressure of a relativistic gas, $p_\gamma = \frac{\rho_\gamma}{3}$, and the CMB black body energy density, $\rho_\gamma = 4\sigma T^4$, we get

$$\frac{d(\rho_\gamma V)}{dt} = -\frac{\rho_\gamma}{3}\frac{dV}{dt}, \tag{C.3}$$

$$\frac{d\rho_\gamma}{dt}V + \rho_\gamma\frac{dV}{dt} = -\frac{\rho_\gamma}{3}\frac{dV}{dt}, \tag{C.4}$$

$$\frac{1}{T}\frac{dT}{dt} = -\frac{1}{3V}\frac{dV}{dt}. \tag{C.5}$$

In an expanding universe with volume element $V = a^3(t)L^3$, the relation becomes

$$\frac{1}{T}\frac{dT}{dt} = -\frac{1}{3a^3(t)L^3}\frac{d[a^3(t)L^3]}{dt} = -\frac{1}{a}\frac{da}{dt}, \tag{C.6}$$

which is an elementary separable differential equation, satisfied for

$$T \propto a^{-1}. \tag{C.7}$$

Appendix D

The Equation of State

This appendix details the derivation of the working forms of the equation of state in flat space, defined as

$$\epsilon_H = -\frac{\dot{H}}{H^2} = -\frac{\ddot{a}/a - (\dot{a}/a)^2}{(\dot{a}/a)^2} = 1 - \frac{\ddot{a}/a}{(\dot{a}/a)^2}. \tag{D.1}$$

Substituting the first Friedmann equation in flat space,

$$H^2(t) = \left(\frac{\dot{a}}{a}\right)^2 = \frac{8\pi G}{3}\rho, \tag{D.2}$$

and the acceleration equation,

$$\frac{\ddot{a}}{a} = -\frac{4\pi G}{3}(\rho + 3p), \tag{D.3}$$

gives

$$\epsilon_H = 1 - \frac{\frac{-4\pi G}{3}(\rho + 3p)}{\frac{8\pi G}{3}\rho} = \frac{3}{2}(1 + w), \tag{D.4}$$

where w would be the coefficient of proportionality between pressure p and density ρ in a single-component universe. For an exponential scale factor $a = e^{Ht}$, we clearly have $d\log a = Hdt$, but in fact this relationship holds more generally, as integrating it just gives the definition of H. So we can alternatively express ϵ_H as

$$\epsilon_H = -\frac{\dot{H}}{H^2} = \frac{1}{H}\left(-\frac{\dot{H}}{H}\right) = \frac{1}{H}\frac{d}{dt}\log(H^{-1}) = \frac{d\log(H^{-1})}{d\log a}, \tag{D.5}$$

that is, as the slope along a plot of $\log(H^{-1}) = -\log H$ versus $\log a$.

Appendix E

Derivation of ϵ_H expected

The derivation of $\epsilon_{H\,\text{expected}} = \frac{1}{n}$ for a single-component universe is:

$$a_n(t) = a_n(t_0)\left(\frac{t}{t_0}\right)^n \tag{E.1}$$

$$\dot{a}_n(t) = n\frac{a_n(t_0)}{t_0^n}t^{(n-1)} = \frac{n}{t}a_n(t) \tag{E.2}$$

$$\ddot{a}_n(t) = n\frac{a_n(t_0)}{t_0^n}(n-1)t^{(n-2)} = \frac{n-1}{t}\dot{a}_n(t). \tag{E.3}$$

Therefore,

$$\epsilon_H = -\frac{\dot{H}}{H^2} = 1 - \frac{\ddot{a}/a}{(\dot{a}/a)^2} = 1 - \frac{a_n(t)\ddot{a}_n(t)}{\dot{a}_n(t)^2} \tag{E.4}$$

$$= 1 - \frac{a_n(t)\frac{n-1}{t}\dot{a}_n(t)}{\dot{a}_n(t)^2} = 1 - \frac{a_n(t)\frac{n-1}{t}}{\frac{n}{t}a_n(t)} = \frac{1}{n}. \tag{E.5}$$

Appendix F

Parameters and Units

Below is a summary of parameters used in the numerical analysis and a description for reference. Units are in mass unless otherwise noted.

- $a(t)$ — [⦸] scale factor
- k — momentum of the mode
- m — mass of the inflaton; the fundamental unit of the analysis; $m = 10^{-6} M_p$
- M_p — Planck mass
- $n_k(t)$ — [⦸] occupation number
- n_k — [mass^3] occupation number (density)
- n_χ — [mass^3] number density
- t — [mass^{-1}] time
- μ — [⦸] Floquet characteristic exponent
- ϕ — inflaton
- Φ — inflaton amplitude
- χ, X — scalar field

Appendix G

Mathieu Equation Stability-Instability chart

We reproduce here the well-known stability-instability chart [59, 60] showing the regions of the parameter space in which the initial value problem solutions for the Mathieu equation (7.6) are either stable or unstable. Note that q and A_k decrease as time progresses.

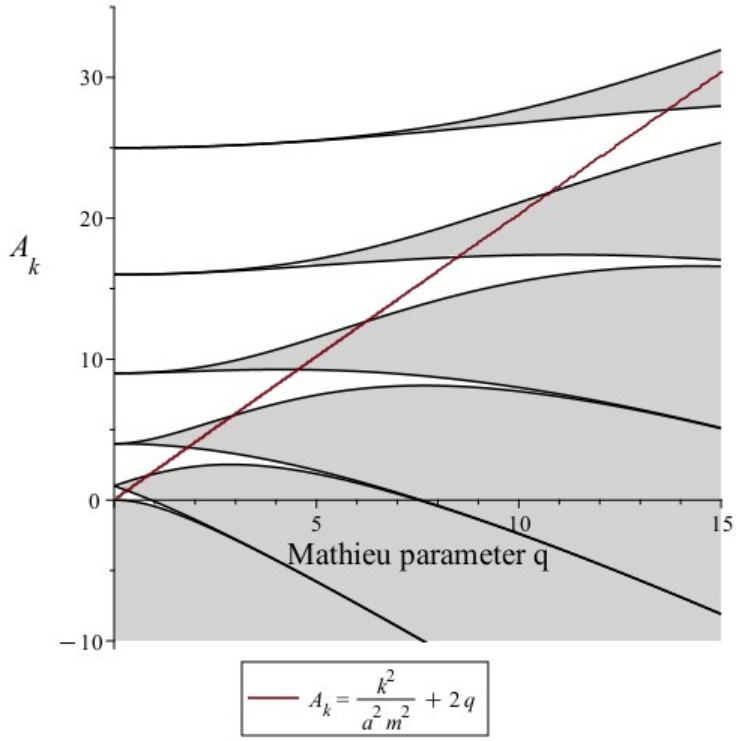

Figure G.1 The areas highlighted in gray are the regions of instability in the q-A_k parameter space. The plot also depicts the Mathieu equation parameters associated with the equation of motion solutions.

Appendix H

Regions of Instability

The regions of instability in Figure G.1 correspond to the periods of sustained exponential growth in n_k during preheating. Figure H.1 superimposes the Mathieu equation instability regions associated with the equation of motion in the KLS model on the time evolution of $\log n_k$, to highlight this correspondence.

There are some interesting and noteworthy differences between the behavior in the three broad-resonance growth regions for n_k (at least for the particular, rapidly-growing value $k = 4m$ we have selected). There are small oscillations visible, in addition to the secular growth in $\log n_k$. During periods when the parameters make the Mathieu equation stable (the white bands in figure H.1), the oscillations are comparatively chaotic; this is also what was seen in figure 7.3 after the last resonant growth period has ending. There is a certain amount of approximately periodic behavior, due to the driving by the amplitude squared of the inflaton field, so there are fairly stark features every half an inflaton oscillation period. (See figures H.2 and H.3.) However, underneath these is a chaotically varying baseline. During the periods of resonance (the gray bands), the baseline behavior is different, with approximately exponential growth in the occupation number, as is typical in an unstable driven system. On top of this are additional oscillations, qualitatively similar in some ways to those in the stability regions. However, there are also clear manifestations of the nonlinearity of the Mathieu equation, in the form of period doubling or tripling. When the exponential growth is subtracted, the residual still has, on average, one peak per half oscillation of the inflaton field. However, these peaks are not evenly placed or of equal amplitude. During the second shown resonance region, the oscillating residuals have periods

equal to the full inflaton oscillation period—a period doubling phenomenon. Within each full oscillation are two dissimilar up-and-down cycles. (See figures H.4 and H.5.) Moreover, in the vicinity of and during the first, shortest resonant period there is period tripling, with the periodic residuals taking one and half inflaton oscillation cycles to return fully to their original phase space positions. (See figures H.6 and H.7.)

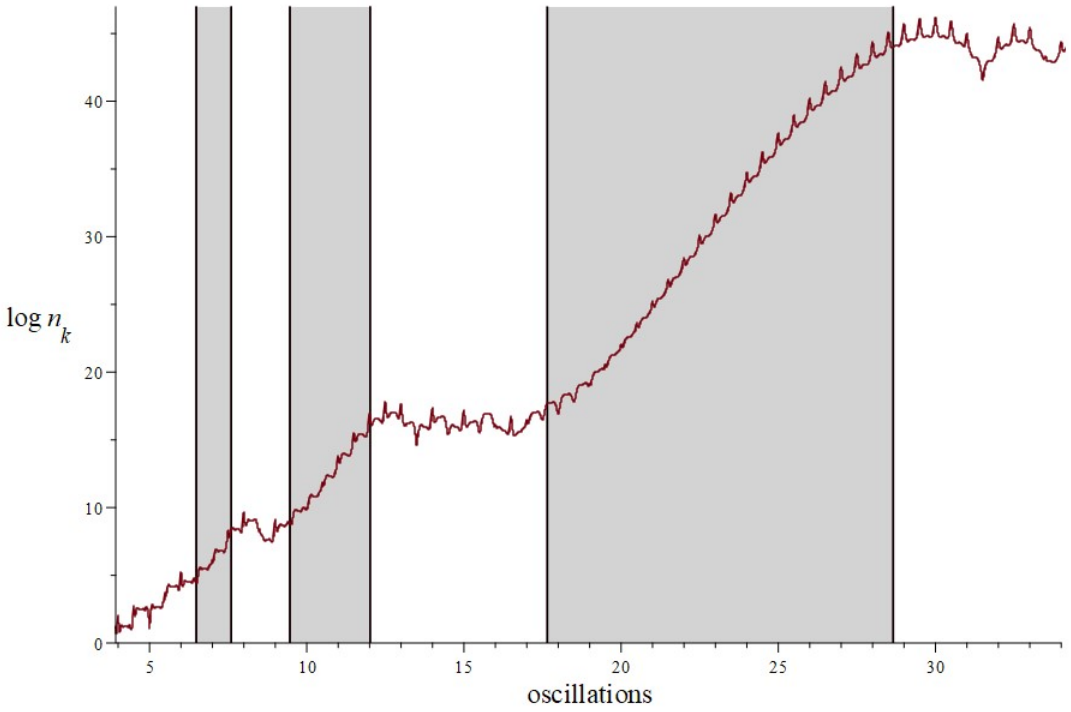

Figure H.1 The final three instability regions superimposed on the $\log n_k$ resonance growth. As the number of oscillations increases, we see exponential growth in occupation number as the q and A_k of figure G.1 decline toward zero and the equation of motion crosses the last three instability regions.

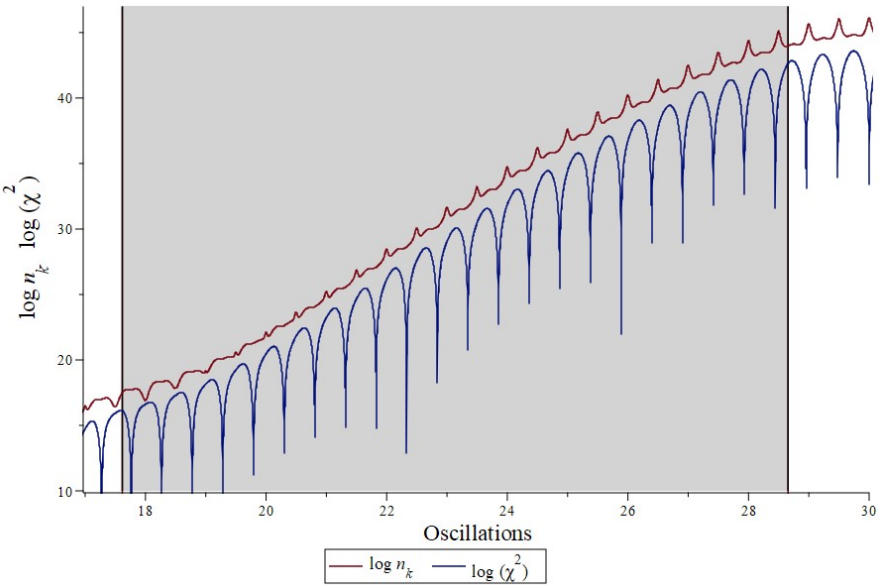

Figure H.2 Instability band for resonance with $N \approx 17.5$ to 28.5.

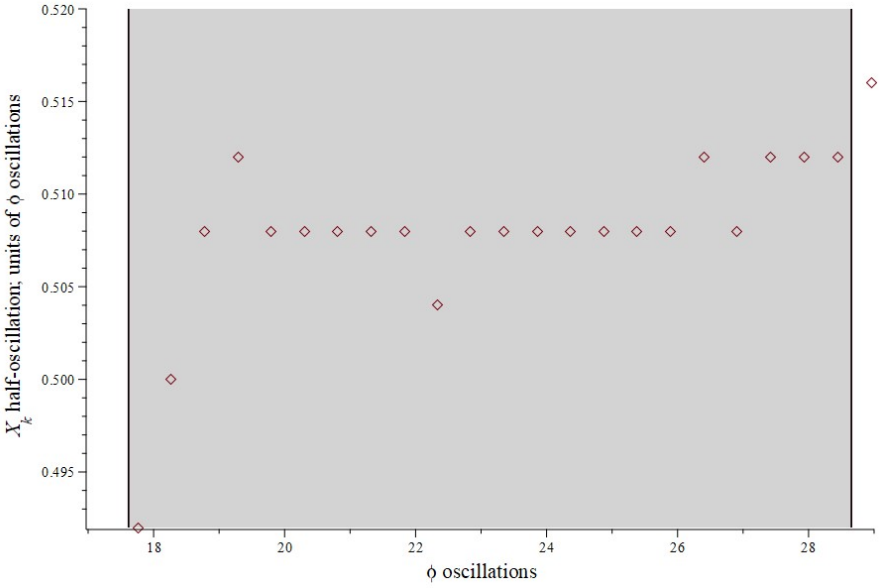

Figure H.3 Resonance at half-periods of χ_k.

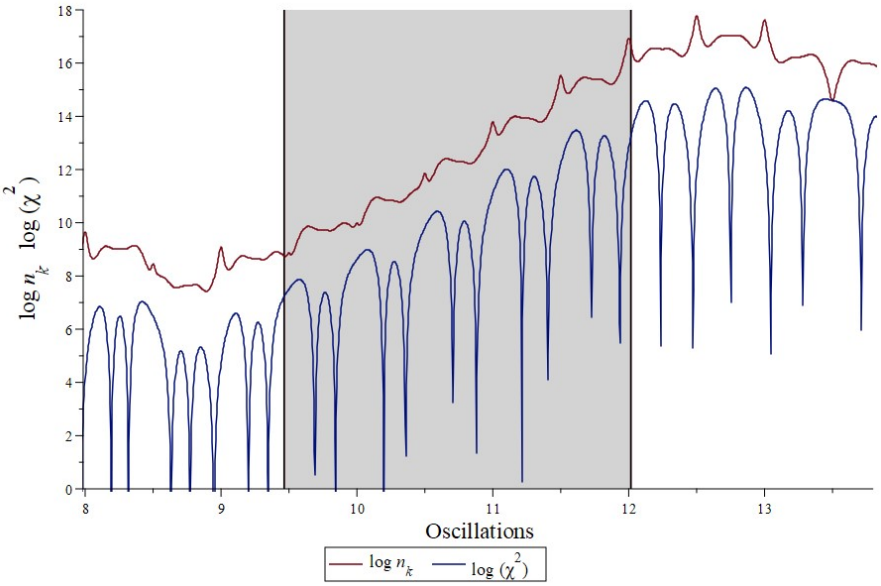

Figure H.4 Instability band for resonance with $N \approx 9.5$ to 12.

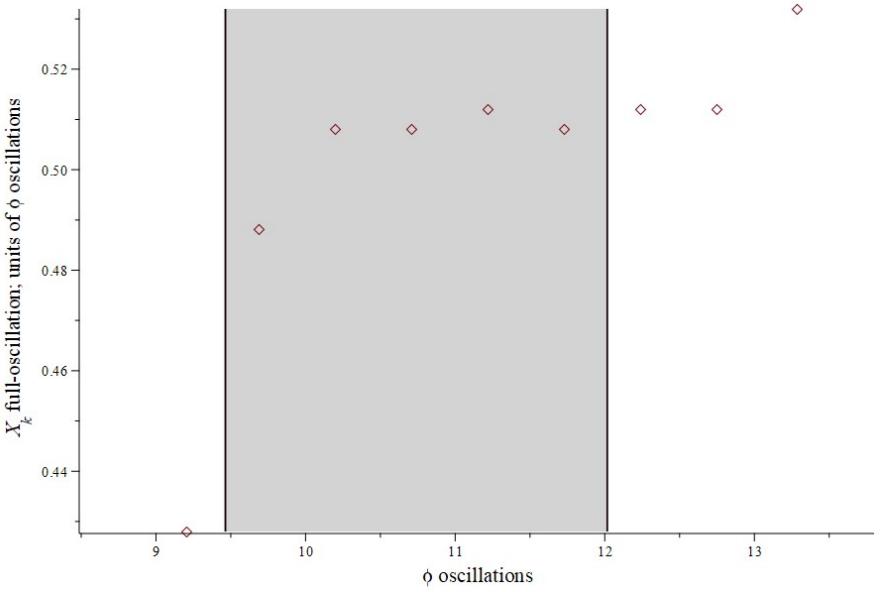

Figure H.5 Resonance at period-doubling of χ_k.

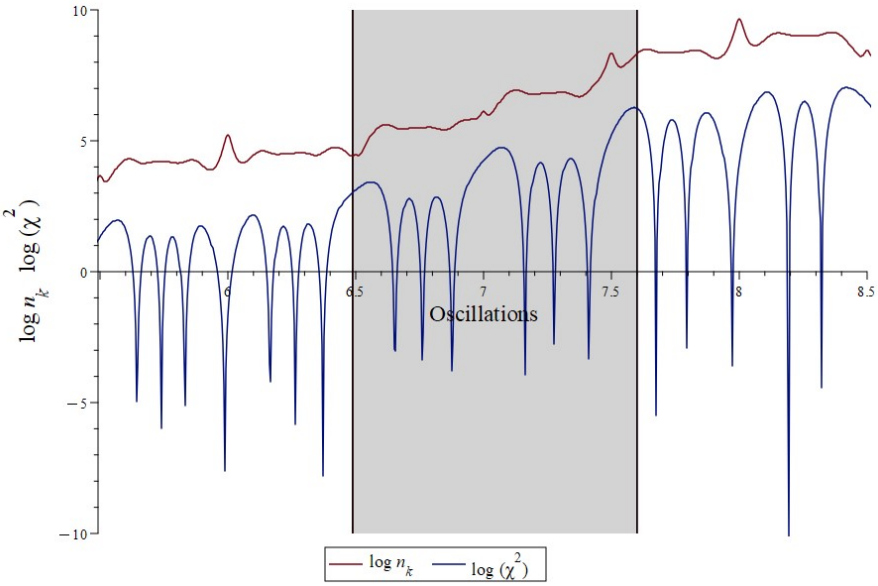

Figure H.6 Instability band for resonance with $N \approx 6.5$ to 7.5.

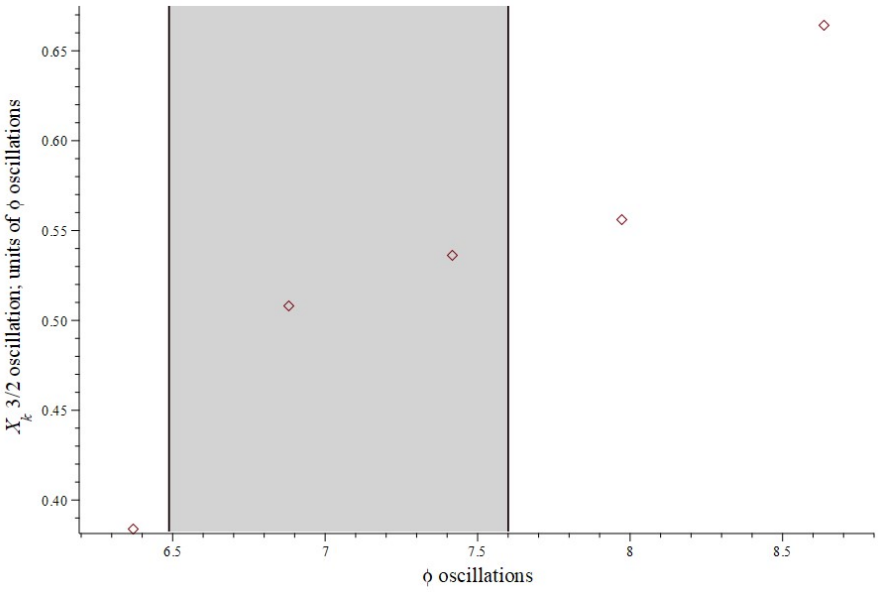

Figure H.7 Resonance at $\frac{3}{2}$-periods of χ_k.

Appendix I

Occupation Number Supporting Data

Table I.1 Data in support of the differences in appearance between graphs (b) of figures 7.1 and 7.2, in which the last column represents the increase in occupation number $\log n_k(36)$ compared to the average value over 4 oscillations from oscillation 34 to 38, and 43.9 and 36.8 are for the KLS and smooth scale factor models, respectively.

$a(t)$ model	ω_k	$\omega_k \lvert X\rvert^2$	$\frac{\lvert\dot{X}\rvert^2}{\omega_k}$	$\log n_k(36)$	Increase
cusped	0.91	4.62×10^{17}	9.56×10^{19}	45.3	0.03
smooth	0.091	8.71×10^{13}	5.79×10^{17}	40.2	0.09

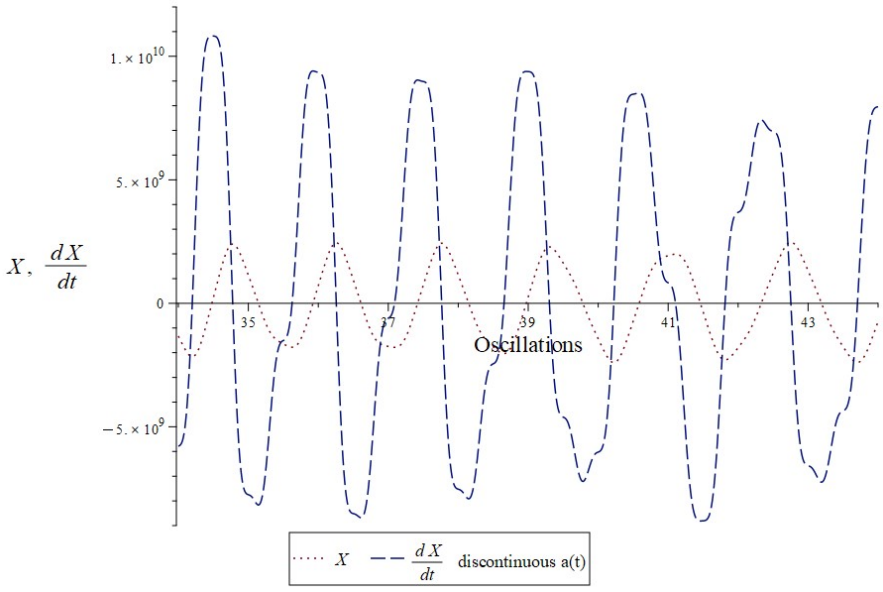

Figure I.1 Plots of scalar field X and its time derivative $\dot{X}$ with the cusped scale factor for 10 oscillations following the end of broad parametric resonance.

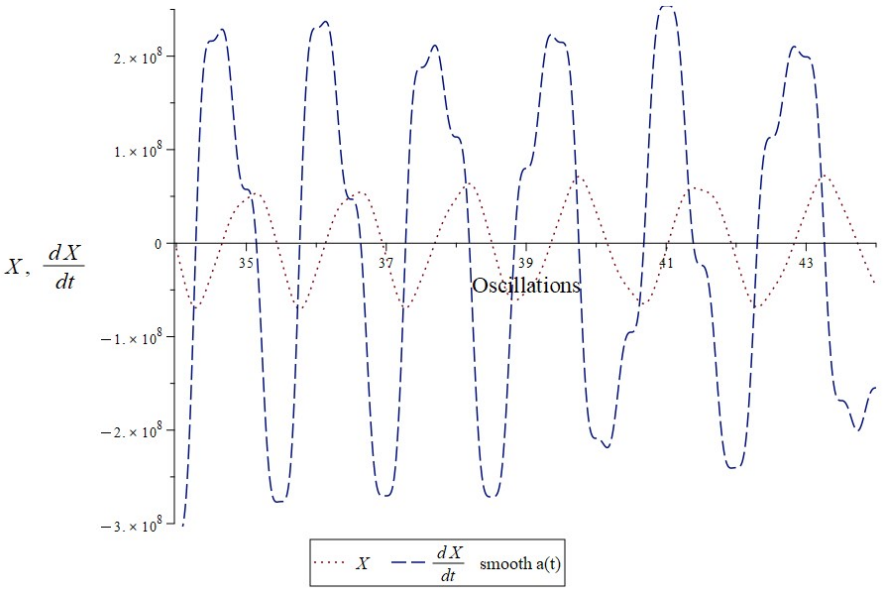

Figure I.2 Plots of scalar field X and its time derivative $\dot{X}$ with the smooth scale factor for 10 oscillations following the end of broad parametric resonance.

Appendix J

Derivation of the Range of Modes

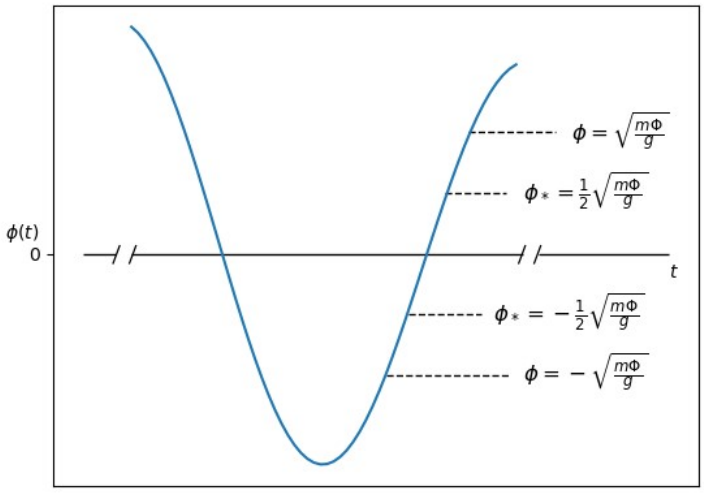

Figure J.1 The outer and inner pairs of dotted lines represent the ranges of $\phi(t)$ that participate in parametric resonance. The wider outer band corresponds to the values of $\phi(t)$ that participate in the resonance as $k \to 0$, and the inner band is the preheating band of broad parametric resonance as $\phi(t) \to 0$.

Appendix J details the derivation of the range of modes k_* that participate in the broad parametric resonance process. KLS provide the typical frequency for the scalar field χ oscillations, $\omega(t) = \sqrt{k^2 + g^2\phi^2(t)}$, subject to the adiabatic instability condition, eq. (7.8),

$$\frac{\dot{\omega}}{\omega^2} \gtrsim 1 \tag{J.1}$$

$$\frac{\dot{\omega}}{\omega^2} = \frac{g^2\phi\dot{\phi}}{\left(k^2 + g^2\phi^2\right)^{3/2}} \gtrsim 1. \tag{J.2}$$

The instability condition yields the inequality defining the unstable modes. The inflaton at the end of inflation is an oscillating field of the form $\phi(t) = \Phi(t)\sin(mt)$. For broad

resonance, when $\phi(t)$ is small and the decaying envelope Ψ is approximately constant over the period of a single oscillation, $\dot{\phi} \approx m\Phi$. This makes the resonance condition

$$1 \lesssim \frac{g^2 \phi m \Phi}{\left(k^2 + g^2\phi^2\right)^{3/2}} \tag{J.3}$$

$$k^2 \lesssim \left(g^2 \phi m \Phi\right)^{2/3} - g^2\phi^2. \tag{J.4}$$

We find the maximum range of k by taking the derivative of the inequality (J.4) to maximize the inflaton value ϕ_*,

$$\frac{2g^{4/3}m^{2/3}\Phi^{2/3}}{3\phi_*^{1/3}} - 2g^2\phi_* = 0, \tag{J.5}$$

for which the solution is

$$\phi_* = (3)^{-3/4}\sqrt{\frac{m\Phi}{g}} \approx \frac{1}{2}\sqrt{\frac{m\Phi}{g}}. \tag{J.6}$$

Substituting $\phi_* \approx \frac{1}{2}\sqrt{\frac{m\Phi}{g}}$ into $k_{\rm max}^2 \lesssim \left(g^2\phi_* m\Phi\right)^{2/3} - g^2\phi_*^2$, we find

$$k_{\rm max} \lesssim \sqrt{\frac{gm\Phi}{2}}. \tag{J.7}$$

Taking $k \to 0$ in eq. (J.3) generates an expression for the inflaton associated with the minimum-range of mode k:

$$\frac{g^2\phi m\Phi}{\left(g^2\phi^2\right)^{3/2}} \gtrsim 1 \tag{J.8}$$

$$\phi \lesssim \sqrt{\frac{m\Phi}{g}}. \tag{J.9}$$

Figure J.1 shows a standard graphical representation of the bands of $\phi(t)$ associated with the minimum and maximum ranges of k. The wider outer band corresponds to the values of $\phi(t)$ that participate in the resonance for the minimal Fourier component—that is, as $k \to 0$. The inner band, $-\frac{1}{2}\sqrt{m\Phi/g} \leq \phi_* \leq \frac{1}{2}\sqrt{m\Phi/g}$, corresponds to the participating $\phi(t)$ associated for the modes with $k_* = \sqrt{gm\Phi}$. This is the preheating band of broad parametric resonance. Explosive growth in the number of particles occurs as $\phi(t) \to 0$. We note that $k_{\rm max}^2$ applies to a band of $\phi(t)$ for which $|\phi| \leq 2\phi_*$. Thus, we find

$$k_* = \sqrt{gm\Phi}. \tag{J.10}$$